TECTONIC HISTORY OF THE OSBOURN SPREADING CENTER

AND

DYNAMIC SUBSIDENCE OF THE CONGO BASIN

Thesis by

Nathan John Downey

In Partial Fulfillment of the Requirements for the

degree of

Doctor of Philosophy

CALIFORNIA INSTITUTE OF TECHNOLOGY

Pasadena, California

2009

(Defended August 21, 2008)

ACKNOWLEDGEMENTS

By indirections, find directions out
                                                -Hamlet, Act 2, Scene I

Although Polonius is talking about lying, I find this quote an appropriate description of my experience with scientific research. It seems that most of the ideas I have are wrong and eventually after pursuing these indirections, I reach some barrier, beyond which I cannot further continue. Luckily, I have had lots of people who have been there to redirect me on another course along which I travel until I meet another barrier, at which someone else has helped me along and so on. In this iterative way it seems that I bounce around from idea to idea until eventually I find myself arriving at some destination, whether or not it was my intended, at which there is some truthful nugget. Well, at least *plausibly* true. Anyway, I would never have reached this place without the help of all the guides along the way. It is those people who I would like to thank here.

First, I would like to give my thanks to my thesis and orals advisors Joann Stock, Mike Gurnis, Rob Clayton and Mark Simons who have been very helpful and devoted many hours to critically analyzing my work. I would also like to thank Jean-Philippe Avouac, Don Helmberger, Tom Heaton and Jeroen Tromp, the various members of my thesis and orals committees. During the last two years I have spent much of my time as a visitor at Harvard University. I learned much at Harvard from John Shaw, who also provided me with office space and computational resources, Rick O'Connell who gave simple but sagacious advice and Brendan Meade for ideas about topography and erosion.

My research also benefited from discussions with the various graduate students in the department. My classmates Chris Dicaprio, Min Chen and Lydia Dicaprio (honorary) were especially helpful and provided many ideas about the problem sets we all struggled to complete in our first years as graduate students. My officemates, Brian Savage, Rowena Lohman, Zhimei Yan, Daoyuan Sun, Javier Favela, Ying Tan and Sonja Spasojevic were

all excellent, and I hope they enjoyed my company as much as I enjoyed theirs. I would also like to thank Ozgun, Vala, Matt, Charlie, David, Julie, Ryan, Laura, Cody and my officemates at Harvard, Amanda and Judith.

Most especially I would like to thank my wife, Nicole, and son, Logan, for making sure that I took care of myself (and them too). Nicole has been such an important part of my life at Caltech that I can't imagine having gone through it without her. Logan has made the latter years of my graduate studies very special, and the enjoyment of the time I spent with him while preparing my thesis provided a much-needed distraction and prevented me from sharing *Don Quixote's* fate in which he:

> *…became so caught up in reading that he spent his nights reading from dusk till dawn and his days reading from sunrise to sunset and so with too little sleep and too much reading his brains dried up, causing him to lose his mind.*

Lastly, I would like to thank my parents who encouraged me to pursue my goals and provided me with the support and assistance needed to do so. Thank you very much.

ABSTRACT

This is a thesis in two parts. First is the presentation of a new technique by which it is possible to constrain tectonic models of oceanic regions which are devoid of magnetic reversal anomalies. I applied this technique to the Osbourn region of the Southwest Pacific and determined the tectonic history of the Cretaceous Osbourn spreading center. The results of this analysis showed that the Osbourn Trough, although an extinct spreading center, was not part of the Cretaceous Pacific-Phoenix spreading center. The second part of this thesis involves study of the cratonic Congo sedimentary basin. I created instantaneous dynamic models of the Congo basin that are strongly constrained by observation and which demonstrate that the most recent subsidence event of the basin has a mantle dynamic origin. These models constrain the density structure of the upper mantle beneath the Congo. In addition, I examined geologic data that constrain the time-dependent history of the Congo basin in an attempt to determine the subsidence mechanism of cratonic sedimentary basins.

TABLE OF CONTENTS

C h a p t e r   1

INTRODUCTION

Chapters one and two of this thesis—which outline the history of the Osbourn Trough—appear, at first glance, to be completely unrelated to Chapters three and four on the Congo basin. The Osbourn Trough is an extinct feature. Conversely, the Congo basin's surface is currently being dynamically depressed. The Congo basin lies on ancient continental crust more than a billion years old, while the oceanic lithosphere near the Osbourn Trough is an order of magnitude younger, having been created during the mid to late Cretaceous. The tectonic history of the Osbourn Trough is the story of an evolving plate boundary. In contrast, the Formation of the Congo basin is of interest because it is a deformational process that occurs *away* from plate boundaries. Finally, and perhaps most obvious, the Osbourn Trough is 5 km beneath the sea surface, whereas the Congo basin appears to have been almost exclusively subaerial for the past one hundred and fifty million years! Despite these dissimilarities, both of these topics stem from the same motivation: the importance of understanding the mechanical properties and behaviors of the lithosphere.

Understanding the tectonic history of the Osbourn Trough is important for several reasons. It was active during the Cretaceous, a period in which enhanced mid-ocean volcanism may have resulted in a rise of global sea level. Quantifying the spreading rates, and therefore the volume of water displaced, of Cretaceous spreading centers is therefore very important. Additionally, the tectonic configuration of the Pacific and surrounding oceanic plates during the Cretaceous is poorly constrained. This poor constraint makes it impossible to accurately create plate reconstructions that extend back to mid-Cretaceous times. However, perhaps the most important reason for understanding the history of the Cretaceous Osbourn spreading center is that this history is part of a larger story in which the largest known oceanic plateau erupted onto the seafloor and fractured into several

pieces, which subsequently spread apart. Three of these pieces eventually became the Manihiki, Hikurangi and Ontong-Java plateaus all of which are contained within the modern Pacific Plate. The relation of this massive eruption to the Pacific-Phoenix-Farallon triple junction is particularly interesting in terms of the mechanical properties of oceanic lithosphere and the interaction between the lithosphere and mantle convection. It is not known if the eruption of this massive plateau occurred at the location of this ridge-ridge-ridge triple junction or if the triple junction shifted to the location of the eruption. The first possibility implies that the material erupted to form the plateaus may have flowed upward within a pre-existing mantle flow regime beneath intersecting mid-ocean ridges, while the second implies that the force of the eruption caused a large-scale re-organization of the plate system. The history of the Osbourn spreading center is just a single chapter within this story; it is interesting because it is the best-constrained part of the story and is a complete documentation of the evolution of the Osbourn system from the initial fracturing of the large plateau to the eventual extinction and capture of the Hikurangi region by the Pacific Plate.

However, understanding the story of the Osbourn Trough is hampered by the lack of magnetic reversals during the Cretaceous Long Normal Polarity Interval (Chron C34) and the resulting magnetic lineations these reversals leave as a record of past spreading activity. In Chapter Two, I present and validate a technique by which it is possible to accurately determine the azimuth of spreading at oceanic spreading centers and place bounds on their spreading rates using abyssal-hill morphology. In Chapter Three, I use this technique to constrain the history of the Osbourn spreading center from birth to death. The most important result of this work is that it appears that there were two triple junctions in the Manihiki region throughout Chron C34, lending support to the theory that the eruption of the Ontong-Java, Manihiki and Hikurangi plateaus caused the fracturing of the Pacific Plate into several microplates. Studying how and why this fracturing process occurred will reveal many insights into the mechanical properties of the oceanic lithosphere. However before we can study these properties we must first document what happened, which is the main motivation of Chapter Three.

The Congo basin study presented here in Chapters Four and Five is also focused on the interactions of mantle convection and the mechanical properties of cratonic lithosphere. Here we have a mantle downwelling which is causing the depression of the Earth's surface. As outlined in Chapter Four, the dynamics of this depression is very well constrained by long-wavelength (>800 km) gravity, topography and shear-wave velocity anomalies. This combination of anomalous observations at the Congo basin allows us to tightly constrain the density structure of the lithosphere beneath the Congo basin, revealing the presence of a large high-density object at shallow (100 km) mantle depths. In Chapter Five I go on to present evidence that the Congo basin, at least for the present and during the Cenozoic, has been depositionally inactive. This observation is very important in terms of the mechanical properties of the lithosphere because it implies that the high-density region within the Congo lithosphere indicated by instantaneous models is (probably) stable. Mechanisms by which this anomaly could be stabilized may include thermal diffusion, although other mechanisms may also be important.

Another important theme of Chapters Four and Five is the implications this study of the Congo basin on cratonic basins in general. The stratigraphic infill and time-dependent properties of the Congo basin throughout the Meso-Cenozoic are typical of Cratonic basins implying the current dynamic state of the Congo basin may also have occurred at other basins in the past. Stratigraphically and economically important entities, the formation mechanisms of these basins are generally unknown, but may provide critical information about the mechanical properties of cratonic lithosphere. The Congo basin, with its unique characteristics may be the key to understanding the formation mechanisms of these basins.

Despite their obvious differences, the two parts of this thesis are motivated by a need to understand the mechanical properties of the lithosphere. The story of the formation of the Osbourn Trough and the current dynamical state of Congo basin help to reveal these properties.

C h a p t e r   2

A RIDGELET TRANSFORM METHOD FOR CONSTRAINING TECTONIC MODELS VIA ABYSSAL-HILL MORPHOLOGY

Nathan J. Downey and Robert W. Clayton

Abstract

Abyssal-hill shape and orientation is related to the direction and spreading rate of paleo-spreading centers. Therefore, analyzing abyssal hill shape and trend is useful for constraining tectonic models of regions devoid of magnetic reversal anomalies. Detecting systematic changes of abyssal hill shapes or trends, due to changes in spreading rate or direction, is not straightforward, which makes it difficult to determine appropriate regions over which to average abyssal hill parameters. Often, however, detecting these systematic changes, where they occur, and the scale over which they occur, is of primary importance for tectonic reconstructions. We present a new method of abyssal-hill analysis that is based on the ridgelet transform, a relative of the 2D wavelet transform. Our method is capable of locally estimating the width, azimuth and root-mean-square (RMS) amplitude of abyssal hill fabric, and highlights changes in these parameters across a survey area, making it possible to identify regions created with a constant spreading rate and direction. We use three multibeam swaths, one crossing the Osbourn Trough in the southwest Pacific Basin, one crossing the East Pacific Rise and one crossing the Mid-Atlantic Ridge, to demonstrate the utility and performance of our method.

1. Introduction

Measurements of abyssal hill morphology can be used to constrain tectonic histories of regions devoid of magnetic reversal anomalies [*Menard*, 1967]. By examining the shape and orientation of abyssal hills over these regions, it is possible to make spreading rate and direction estimates for use in tectonic reconstructions; however other factors can also affect abyssal hill shape and trend [*Goff et al.*, 1997].

The shape of abyssal hills is controlled by the faulting process that occurs at oceanic spreading centers after the formation of oceanic crust [*Buck and Polikov*, 1998; *Goff, et al.*, 1995; *Macdonald, et al.*, 1996]. The nature of this faulting is determined by the local stress state, which is in turn, related to the spreading rate. Therefore several measures of abyssal hill shape correlate with spreading rate and direction. These measures include abyssal hill width, asymmetry (measured as a difference in slope between the sides facing toward and away from the spreading center) and root-mean-square (RMS) amplitude [*Goff*, 1991; *Goff, et al.*, 1997; *Hayes and Kane*, 1991; *Kriner, et al.*, 2006]. Abyssal hill trend (the azimuth of the hill's long axis) and the distribution in azimuths of the slopes facing toward and away from the spreading axis are useful indicators of paleo-spreading direction [*Goff and Jordan*, 1988; *Kriner, et al.*, 2006].

Abyssal hill shape and azimuth naturally vary. Even amongst abyssal hills simultaneously created at a single spreading center there is a slight variation in these parameters. This natural variation therefore requires that we obtain an average abyssal hill shape that can then be used to infer spreading rates and directions. This variation makes it necessary to use statistical tests to determine if the mean shape or trend of two populations of abyssal hills is different. The techniques of *Goff and Jordan* [1988] and *Kriner et al.* [2006] approach the problem of abyssal hill variation by estimating an average shape and trend parameter for a region of seafloor. During this process, any systematic change in abyssal hill shape across this region is lost, making it necessary to use a cross-validation approach, where several estimates are made over the same area using different estimation regions, to determine the location of systematic changes in abyssal hill shape. Often, however, these changes are interesting tectonic features, that indicate a change in spreading rate or

direction. For example, *Larson et al.* [2002] were able to map the location of the Pacific-Phoenix-Farallon triple junction trace by examining changes in abyssal hill trends.

In this paper we present a new method of estimating the width, trend, and RMS amplitude of abyssal hills based on the ridgelet transform [*Candès*, 1998; *Starck et al.* 2002, 2003]. This method is spatially local, with the capability of determining the shape and azimuth of individual abyssal hills. The advantage of this technique is that averaging after shape estimation makes it easier to identify the location of systematic changes in abyssal hill shape. As a result, determining appropriate regions over which to average shapes and azimuths is simplified. We demonstrate the usefulness of this technique by examining three swaths of multibeam data (Figure 1), one collected near the Osbourn Trough (OT) [*Lonsdale*, 1997], one collected near the East Pacific Rise (EPR) and one collected near the Mid-Atlantic Ridge (MAR). Our results highlight the differences between abyssal hills created at fast and slow spreading centers, as outlined by *Goff* [1991], *Goff et al.* [1995,1997] and *Hayes and Kane* [1991]. We are able to detect two regions of anomalous seafloor morphology near the EPR, which correspond to the location of the Loius Scarp and Yaquina Fracture Zone [*Eakins and Lonsdale*, 2003] and are able to show that the Louis Scarp marks the location of a possible change in spreading direction. We also identify the possible location of either a change in the spreading direction of the Osbourn paleo-spreading center or the location of a triple junction trace, and the location of a possible reduction of spreading rate at the Osbourn paleo-spreading center.

2. The ridgelet transform

2.1 Wavelet analysis of geologic textures

The two-dimensional ridgelet transform [*Candès*, 1998; *Starck, et al.*, 2003] is a relative of the two-dimensional wavelet transform. Wavelet transform methods have varied application in the Earth sciences [*Kumar and Foufoula-Georgiou*, 1997], including quantifying the multiscale alignment of fault outcrops in a continental setting [*Ouillion*, 1996], the study of rock fabric alignment [*Gaillot, et al.*, 1999], and the analysis of sea floor texture [*Little, et al.*, 1993]. *Little et al.* [1993] used 1D wavelets to highlight a region

of reduced short-wavelength power and enhanced long-wavelength power in a center-beam bathymetry profile collected northeast of Hawaii. They conclude that this anomalous region was created at a small abandoned spreading center, which they were able to locate near the region's center. The wavelet transform allowed them to separate the scales of the bathymetry so that a large-scale thermal swell could be analyzed separately from the small-scale features associated with the abandoned spreading center.

Little et al. [1994, 1996] extended this technique to the analysis of 2D Sea Beam data. For this analysis they created a 2D analyzing function capable of enhancing abyssal hills of an *a priori* preferred orientation. These functions were applied to data collected near the Mid-Atlantic Ridge, and by selectively enhancing features oriented parallel to the ridge axis, were able to recreate an interpretation of abyssal-hill fabric made by identifying abyssal hills manually [*Little and Smith*, 1996].

Our ridgelet transform method differs from that of *Little et al.* [1994, 1996] because it automatically determines abyssal-hill azimuths and scales for individual abyssal hills. These individual estimates are then averaged in regional groups such that populations of hills with statistically different properties are identified.

2.2 Definition of the ridgelet transform

The ridgelet transform maps a function in a 2D space-space domain to a 3D space-azimuth-scale domain. It is defined as follows [*Candès and Donoho*, 1999; *Starck, et al.*, 2003]. Choose a function, $\psi : \mathbf{R} \rightarrow \mathbf{R}$ (where $\mathbf{R}$ indicates the set of real numbers), with sufficient decay and which satisfies the wavelet definition [*Mallat*, 1998]:

$$\int \psi(s) \, ds = 0 \, . \tag{1}$$

The corresponding ridgelet is defined for a scale parameter $a > 0$, a location parameter (we use along-track distance) $b \in \mathbf{R}$, and an azimuth parameter $\theta \in [0°, \ 360°)$ measured positive clockwise from the x_2 (northward) direction, as the function $\psi_{a,b,\theta} : \mathbf{R}^2 \rightarrow \mathbf{R}$ [*Candès and Donoho*, 1999]:

$$\psi_{a,b,\theta}(x_1,x_2) = \frac{1}{\sqrt{a}} \; \psi\left(\frac{x_1 \sin(\theta) + x_2 \cos(\theta) - b}{a}\right). \tag{2}$$

A plot of this function for various values of a, b and θ is presented in Figure 2. The ridgelet transform is given by:

$$R_f(a,b,\theta) = \iint \overline{\psi}_{a,b,\theta}(x_1,x_2) f(x_1,x_2) \, dx_1 dx_2 \tag{3}$$

where $f : \mathbf{R}^2 \to \mathbf{R}$ is the function we wish to analyze.

A ridgelet can be thought of as an infinitely anisotropic two-dimensional wavelet: it is constant along the q direction and has a cross-sectional shape given by dilations of y. When used in a ridgelet transform, the ridgelet function locates and characterizes the elongate features of f, similar to the anisotropic wavelets of *Gaillot et al.* [1999] and *Ouillon et al.* [1996] and to the analyzing functions of *Little et al.* [1994].

2.3 Digital implementation of the ridgelet transform

A useful property of the ridgelet transform is its relation to the Radon transform [*Bracewell*, 2000]. The Radon transform of a function $f : \mathbf{R}^2 \to \mathbf{R}$ is given by:

$$Ra_f(\theta,s) = \iint f(x_1,x_2) \, \delta(x_1 \sin(\theta) + x_2 \cos(\theta) - s) \, dx_1 dx_2 \tag{4}$$

where s is a location parameter (usually chosen to be one spatial dimension of the original signal) and θ is defined as before. The Radon transform maps a function from a space-space domain to a space-azimuth domain. If we use the one-dimensional wavelet transform along the space dimension of the Radon transform formula:

$$\int Ra_f(\theta,s) \, \psi_{a,b}(s) \, ds \tag{5}$$

where $\psi_{a,b}(s)$ is the dilated and translated wavelet:

$$\psi_{a,b}(s) = \frac{1}{\sqrt{a}} \ \psi\left(\frac{s-b}{a}\right)$$
(6)

with a and b defined as before, we recover the ridgelet transform (Equation 3).

This property suggests a method by which we can calculate the ridgelet transform of a dataset: first transform to the Radon domain, then apply a 1D wavelet transform along lines of constant θ [*Starck, et al.*, 2002; *Starck, et al.*, 2003].

The 2D ridgelet transform maps linear features in a two-dimensional space-space domain to maxima in a three-dimensional location-scale-azimuth domain. By applying the ridgelet transform, with appropriate y, to multibeam bathymetry and then locating maxima in the ridgelet domain we are able to determine the dominant scale and azimuth of abyssal ridges along a multibeam swath. It is, therefore, relatively simple to detect the location and scale of systematic changes in these parameters using statistical tests. The local RMS amplitude is easily calculated during our implementation of the ridgelet transform (see *§3.1* below).

The ridgelet transform is invertible [*Starck, et al.*, 2002, 2003], however, invertibility is not necessary for our analysis because we interpret our data directly in the ridgelet domain. This ridgelet domain analysis allows us considerable latitude in the design and implementation of the ridgelet transform algorithm. We first Radon transform the bathymetry data by numerically calculating the line integrals given by Equation (4) in the spatial domain. Because multibeam data are collected in swaths, a bias is introduced when calculating the Radon transform, i.e. along-track azimuths will have a longer domain of integration in (4) than will cross-track azimuths. A space-domain implementation allows us to avoid this bias by restricting the length of the along-track Radon integrals. A space-domain calculation also allows us to normalize the Radon integral (4) by the length of the line along which the data are summed, avoiding the problem of irregular edges and gaps in the data. This normalization yields an "average" bathymetry along an azimuth, allowing for a more physical interpretation of the Radon-transformed data. This Radon transform process also results in a regular gridding of the data in the Radon domain allowing us to use

standard Fast Fourier Transform techniques to calculate the wavelet transform during the transformation of the data to the ridgelet domain.

3. Application of the ridgelet transform to abyssal-hill morphology

3.1 Example ridgelet transform of multibeam data

We use a section of multibeam data collected north of the Osbourn Trough [*Lonsdale*, 1997] by the research-vessel icebreaker (R/VIB) *Nathaniel B. Palmer* during cruise NBP0304 in 2003 (Figure 1) to illustrate the ridgelet transform (Figure 3). The Osbourn Trough is located between 26°S and 26°15'S at the bottom of Figure 3a.

Our Radon transform algorithm takes a gridded multibeam dataset as input (we use a 200 m grid spacing) and a series of track points that (approximately) run down the center of the multibeam swath. The track points parameterize the "location" for the location-azimuth output of the Radon transform. For each track point we only use the data within a 10 km radius (the Radon aperture), which is approximately half the width of a multibeam swath. We calculate the average bathymetry of the data in that window and subtract it from the data within the window to yield a bathymetric anomaly. The RMS amplitude of this anomaly is our local measure of the RMS amplitude of the abyssal hills (we also simultaneously calculate the RMS amplitude of the bathymetry within a 20 km-radius window for comparison). The 10 km-radius window restricts our analysis to wavelengths less than ~20 km. A similar wavelength band was used by *Hayes and Kane* [1991] in their analysis of abyssal-hill RMS amplitude.

Next, the Radon integral (4) is calculated along lines intersecting the track point with azimuths varying from 0° to 180°. The result of these integrals for each azimuth is then normalized by the length of the integral through regions of defined bathymetry (i.e. the Radon integral is not calculated over gaps in the data). The final output, after this process has been applied to all track points, is the Radon transform of the bathymetric anomaly in a track point-azimuth domain. The output of our Radon transform algorithm for the example dataset is shown in Figure 3b.

Features localized near a single point of the spatial domain become localized along lines in the Radon domain. In a location-azimuth space these lines follow the shape of the tangent function. This effect can be seen by examining the Radon transform of the two seamounts near 25°37'S (Figure 3a). These seamounts appear in Figure 3b as low-amplitude linear anomalies in the shape of tangent curves centered at 90°. Conversely the Radon transform concentrates linear features in the spatial domain at single points of the Radon domain. The location of these points coincides with the azimuth and location of their parent features in the spatial domain. There is a small NW-SE trending ridge located within the Osbourn Trough at 26°4'S in Figure 3a. This ridge maps to a peak in the Radon domain at 120° azimuth (Figure 3b). The peaks in Figure 3b corresponding to narrow ridges on the seafloor are much more localized than are the peaks corresponding to wide abyssal ridges. For narrow abyssal ridges, a small range of azimuths lay along the top of the abyssal ridges (i.e., the region where the abyssal ridge is significantly higher than the abyssal plain). However, for wider abyssal ridges, the range of azimuths that lay along the region of high bathymetry is much larger. Therefore the width of a peak in the Radon domain is wider in azimuth for large scale abyssal hills than for small scale abyssal hills. This effect is reduced by increasing the width of the multibeam swath by combining data from two adjacent swaths and using a correspondingly larger Radon aperture.

Because the Radon transform resolution depends on abyssal-hill scale, a further separation of the data based on scale is desired. This separation is accomplished during the second step of the ridgelet transform. The wavelet that we choose to use for this step is the Mexican Hat wavelet (Figure 4), which is defined as the second derivative of a Gaussian:

$$\psi(x) = -\frac{d^2}{dx^2} e^{-(x^2/2)} = \left(1 - x^2\right) e^{-(x^2/2)}. \tag{7}$$

The Mexican Hat wavelet satisfies the following equation, when $\Gamma = \mathbf{R}$:

$$\int_{\Gamma} \psi(x)\, x^n dx = 0, \quad n = 0,1. \tag{8}$$

For $n = 0$, this equation reduces to the wavelet definition (1) and the $n = 1$ case demonstrates that the Mexican Hat wavelet has zero linear moment. Because the Mexican

Hat wavelet is localized to a small region of **R** , called its "effective support", (see Figure 4), equation (8) holds approximately when Γ is equal to the effective support. The Mexican Hat wavelet is insensitive to the mean and any linear trend in the data over the wavelet's effective support, so we are able to measure the scales of small ridges superimposed on large ridges independently, as the large ridge is approximately linear at the scale of the smaller ridge. Also, because the Mexican Hat wavelet is symmetric, peaks in the Radon domain correspond to peaks in the ridgelet domain, preserving their sign. Thus local minima in the ridgelet domain correspond to trenches and local maxima correspond to ridges. The locations of the maxima in the ridgelet domain provide us with a local measure of the azimuth and scale of abyssal hills.

The wavelet transform increases the dimensionality of the data by one, taking us from the 2D azimuth-location domain of the Radon transformed data to the 3D azimuth-location-scale domain of the ridgelet transformed data. To compare our results with those of previous studies it is necessary to convert the scale, which is a relative measure of wavelet size, to a width parameter expressed in kilometers. We define this new width parameter to be the distance between the zero crossings of the Mexican Hat wavelet of appropriate scale (Figure 4).

Figures 3c-f show the output of the ridgelet transform of the data in Figure 3a as several constant-width slices through the ridgelet transform output. Because the Radon transform utilizes a "Dirac ridge" (see the square panel below Figure 3b) to transform data, it is sensitive to all linear features in the data regardless of the scale (width) of those features. A ridgelet corresponding to the widths of the slices in Figures 3c-f are plotted, at the scale of the data in Figure 3a, in the square panel beneath each slice. These ridgelets are only sensitive to linear features in the data that have a width close to that of the ridgelet itself. Described in this way, the ridgelet transform of the data for a specified scale can be interpreted as a band-limited Radon transform. Thus Figures 3c-f can be thought of as a scale decomposition of Figure 3b.

As noted above, the peaks corresponding to the small-scale ridges in the space domain are much smaller in azimuth than the peaks corresponding to large scale ridges. The azimuth

resolution is constant across each ridgelet slice, therefore the ridgelet transform also separates the well-resolved small-scale features from the poorly resolved large-scale ones. Increasing the size of the Radon aperture would help to better resolve the large-scale features. In this case, however, the size of the Radon aperture is limited to the width of the multibeam swath. A wider swath width (or 2 swaths next to each other) would improve the resolution in azimuth at our scales of interest. For a constant azimuth, the ridgelet transform has the same resolution characteristics as the wavelet transform—better location resolution at small scales and better scale resolution at large scales [*Mallat*, 1998].

By examining Figures 3c-f we can see that the peak corresponding to the small ridge at 26°4'S has highest amplitude for a width of 4 km. We can therefore estimate this abyssal hill's width as 4 km and its azimuth as 120°. Similarly the ridge bounding the northern side of the Osbourn Trough at 25°56'S has a dominant width of 8 km and an azimuth of ~80°. On Figure 3a, we have marked the azimuth and scale at the appropriate location for each ridgelet maxima by a symbol consisting of a line segment that parallels the ridge axis, and an I-shaped symbol oriented 90° to the line segment, whose length equals the width of each ridge. A sample symbol for an azimuth of 45° and a width of 5 km is shown beneath Figure 3a.

3.2 Results of ridgelet analysis of the Osbourn Trough, East Pacific Rise and Mid-Atlantic Ridge datasets

In addition to the Osbourn Trough multibeam data, we also applied our ridgelet transform method to two other multibeam swaths (Figure 1). The East Pacific Rise (EPR) dataset was acquired by the *R/V Revelle* in 1997 (cruise GENE04), while the Mid-Atlantic Ridge (MAR) dataset was acquired onboard the *R/V Melville* in 2002 (cruise VANC05). A sample of the output of our ridgelet transform analysis of these additional swaths is shown in Figures 5 and 6. The East Pacific Rise is located at longitude 108°48'W in Figure 5a, and the Mid-Atlantic Ridge is located near 10°3'W in Figure 6. The widths and azimuths of the abyssal hills are marked in Figures 5 and 6 using the same scheme as in Figure 3a. The three datasets presented here were chosen because they were collected during transits across a spreading center (or extinct spreading center in the case of the Osbourn Trough)

and therefore are long stretches of a single swath.   Furthermore these swaths survey bathymetry created at much different spreading rates.   The EPR dataset surveys crust created at roughly 14 cm/yr [*Small*, 1998] whereas the MAR dataset surveys crust created at 3.3 cm/yr [*DeMets et al.*, 1991].   The paleo-spreading rate of the Osbourn spreading center is estimated to have been 6-8 cm/yr [*Billen and Stock*, 2000]

The output of the application of our ridgelet transform procedure to the multibeam data acquired during all three cruises is shown in Figures 7-9 and Table 1. Figure 7 displays the results of the ridgelet analysis of the EPR dataset. This dataset includes two regions of anomalous abyssal hill shape. The eastern anomalous region extends from 109°3'W to 108°12'W (Figure 5b) and is characterized by an increased RMS amplitude and NE and NW trending abyssal hills, values much different from the regional abyssal-hill trends (see Figures 7a and 7c). The location of this anomalous region coincides with the trace of the Yaquina Fracture Zone (Figure 5b) as mapped by *Eakins and Lonsdale* [2003].   The western region of anomalous bathymetry extends from 111°54'W to 110°45'W (Figure 5c) and is likewise characterized by increased RMS amplitude, but does not exhibit any unusual abyssal-hill trends. This corresponds to the location of the Louis Scarp [*Eakins and Lonsdale*, 2003]. These two anomalous regions provide natural boundaries between regions of relatively constant abyssal-hill properties. Therefore we divide the EPR abyssal hills into three populations (Figure 6). Group EPR 1 consists of abyssal hills observed west of the Louis Scarp, EPR 2 contains those observed between the Louis Scarp and the Yaquina Fracture Zone and EPR 3 are the abyssal hills observed east of the Yaquina Fracture Zone. All three populations exhibit similar RMS amplitudes, ranging from 50-100 m, a range typical of crust created at fast spreading centers [*Goff et al.*, 1997]. Similarly, all three populations exhibit a similar mean abyssal hill width. However these widths vary widely in all three populations. The Louis Scarp, however, marks the location of a change in abyssal hill strike. Population EPR 1 has a mean azimuth of 5.1° and an angular deviation [*Cain*, 1989] of 8.6°, while EPR 2 has mean azimuth of 12.3° and angular deviation of 7.3° (Table 1). The result of a Watson-Williams test [*Zar*, 1999] shows that these means are significantly different with 95% confidence. Thus the Louis Scarp may mark the location of a change in spreading direction.

The results of the ridgelet analysis of the MAR dataset are shown in Figure 8. Unlike the EPR abyssal hills, the azimuths of the MAR abyssal hills do not vary significantly along the ship track, and we see no reason to separate these abyssal hills into separate populations based on their shapes and locations. The widths also vary widely, with a slightly higher mean value than the EPR abyssal hills, as would be expected for slower spreading centers, however, the large scatter of widths makes it impossible to determine if this difference is significant. The RMS amplitude of the bathymetry near the Mid-Atlantic Ridge is in general much larger than that of the EPR, ranging from 100-400m, a range that is in agreement with that of typical slow-spreading regions [Goff et al., 1997]. However, farther from the Mid-Atlantic Ridge, RMS amplitudes decrease markedly. This decrease in seafloor roughness is most likely due to an increase in sediment cover (gray line in Figure 7c) which artificially smoothes seafloor bathymetry.

There is a change in abyssal hill azimuth for the Osbourn Trough dataset (Figure 8) at approximately 23°S. Abyssal hills between 20°S and 22°S (group OT 1) have mean trend of 98.3° and an angular deviation of 7.1° while abyssal-hills between 24°S and 26°S (group OT 3) have mean trend 90.6° and an angular deviation of 6.8°. The result of a Watson-Williams test shows that these two populations have different means at a 95% confidence level. However, the abyssal hills between 22°S and 24°S (group OT 2) have a mean trend of 93.9° which is not significantly different from the means of either groups OT 1 or OT 3. Unlike the relatively sudden shifts of abyssal-hill azimuths observed at the Louis Scarp, this change in azimuth appears to occur over a larger scale. Two possible geologic scenarios which would result in a change in abyssal-hill trend are a change in paleo-spreading direction along this multibeam swath, or the presence of a triple junction trace between 22°S and 24°S. The widths of the OT abyssal hills are typically about 5 km. The sediment thickness along the OT dataset is in general quite thin, so sediment smoothing should not affect our estimates of seafloor roughness there. The RMS amplitudes of this dataset are also quite low, near 50-100 m, with the exception of the region immediately north of the Osbourn Trough which exhibits roughness of 50-300 m. This pattern of roughness of the Osbourn Trough dataset may result from a significant slowing of spreading rate prior to the extinction of the Osbourn Trough.

4. Discussion and conclusions

Our ridgelet transform method is capable of locally estimating abyssal-hill width, azimuth and RMS amplitude. It should also be possible to modify our method to quantify other aspects of abyssal hill shape. Using asymmetric wavelets in conjunction with the Mexican Hat wavelet utilized here may quantify abyssal-hill asymmetry using the ridgelet transform. The estimation of abyssal-hill shape should be especially useful for studies of regions where other data types are unavailable for constraining tectonic models, such as regions created during periods of constant magnetic polarity.

A particularly important aspect of our method is that it simplifies detecting changes in abyssal hill shape, which is a possible indicator of a change in spreading rate or direction. We are able to use our method to detect a change in spreading direction at the Louis Scarp west of the EPR, a possible change in spreading direction, or the location of a triple junction trace, north of the Osbourn Trough, and a possible decrease in spreading rate prior to the extinction of the Osbourn paleo-spreading center. Determining when any change in spreading direction or rate occurred, however, is not directly possible using multibeam data. Unlike magnetic reversal data there is no timescale associated with changes in abyssal-hill morphology. Other data, such as radiometric dating of dredge or core samples are required to fully constrain the tectonic history of a region via abyssal hill morphology. There are several potential sources of error in our ridgelet analysis. Any process that modifies the shape of abyssal hills after their formation will affect the results of any bathymetry analysis. Two of the most prevalent processes are intraplate volcanism resulting in the formation of seamounts and the modification of seafloor shape by sedimentation. Small point features in the multibeam data are sufficiently averaged out during the Radon transform, but large seamounts can affect the output if their height exceeds the amplitude summed along nearby abyssal ridges. In the regions where abyssal hill analysis may be most useful for tectonic reconstructions (i.e., those created during the Cretaceous Long Normal Polarity Interval; Chron C34, 83-121 Ma [*Cande and Kent*, 1995]) sediment cover can be relatively thick. Sediment cover tends to smooth out bathymetry by reducing the RMS amplitude and damping the expression of small scale features. Therefore, it is important to know the sediment thickness near multibeam surveys.

Seismic data and drilling may provide some control on sediment thickness. Ultimately, however, the errors that may affect the results of our ridgelet transform method must be examined on a region by region basis.

References

Billen, M. and J. Stock (2000), Morphology and Origin of the Osbourn Trough, *Journal of Geophysical Research*, *105*, 13481-13489.

Bracewell, R. (2000), *The Fourier Transform and its Applications*, McGraw-Hill, Singapore.

Buck, W., and A. Polikov (1998), Abyssal hills formed by stretching oceanic lithosphere, *Nature*, *392*, 272-275.

Cain, M. (1989), The analysis of angular data in ecological field studies, *Ecology*, *70*, 1540-1543.

Cande, S., and D. Kent (1995), Revised calibration of the geomagnetic polarity time scale for the late Cretaceous and Cenozoic, *Journal of Geophysical Research*, *100*, 6093-6095.

Candès, E. (1998), Ridgelets: Theory and application, Ph.D. thesis, pp. 116, Stanford University, Stanford.

Candès, E., and D. Donoho (1999), Ridgelets: A key to higher dimensional intermittency, *Philosophical Transactions of the Royal Society of London*, *357*, 2495.

DeMets, C., Gordon, A., Argus, D., and S. Stein (1990), Current plate motions, *Geophysical Journal International*, *101*, 425-478.

Divins, D. L. (2006), NGDC Total sediment thickness of the world's oceans & marginal seas, http://www.ngdc.noaa.gov/mgg/sedthick/sedthick.html, *National Geophysics Data Center, Boulder, CO.*

Eakins, B. and P. Lonsdale (2003), Structural patterns and tectonic history of the Bauer microplate, Eastern Tropical Pacific, *Marine Geophysical Researches*, *24*, 171-205.

Gaillot, P., Darrozes, J. and J. Bouchez (1999), Wavelet transform: a future of rock fabric analysis?, *Journal of Structural Geology*, *21*, 1615-1621.

Goff, J. (1991), A global and regional stochastic analysis of near-ridge abyssal hill morphology, *Journal of Geophysical Research*, *96*, 21713-21737.

Goff, J., and T. H. Jordan (1988), Stochastic modeling of seafloor morphology: Inversion of Sea Beam data for second-order statistics, *Journal of Geophysical Research*, *93*, 13589-13608.

Goff, J., Ma, Y., Shah, A., Cochran, J. and J. Sempere (1997), Stochastic analysis of seafloor morphology on the flank of the Southeast Indian Ridge: The influence of ridge morphology on the formation of abyssal hills, *Journal of Geophysical Research*, *102*, 15521-15534.

Goff, J., Tucholke, B., Lin, J., Jaroslow, G. and M. Kleinrock (1995), Quantitative analysis of abyssal hills in the Atlantic Ocean: A correlation between inferred crustal thickness and extensional faulting, *Journal of Geophysical Research*, *100*, 22509-22522.

Hayes, D., and K. Kane (1991), The dependence of seafloor roughness on spreading rate, *Geophysical Research Letters*, *18*, 1425-1428.

Kriner, K., Pockalny, R. and R. Larson (2006), Bathymetric gradients of lineated abyssal hills: Inferring seafloor spreading vectors and a new model for hills formed at ultra-fast rates, *Earth and Planetary Science Letters*, *242*, 98-110.

Kumar, P., and E. Foufoula-Georgiou (1997), Wavelet analysis for geophysical applications, *Reviews of Geophysics*, *35*, 385-412.

Larson, R., Pockalny, R. Viso, R., Erba, E. Abrams, L., Luyendyk, B., Stock, J. and R. Clayton (2002), Mid-Cretaceous tectonic evolution of the Tongareva triple junction in the southwest Pacific Basin, *Geology*, *30*, 67-70.

Little, S. (1994), Wavelet analysis of seafloor bathymetry: An example, in *Wavelets in Geophysics*, edited by E. Foufoula-Georgiou and P. Kumar, pp. 167-182, Academic Press, San Diego.

Little, S., Carter, P. and D. Smith (1993), Wavelet analysis of a bathymetric profile reveals anomalous crust, *Geophysical Research Letters*, *20*, 1915-1918.

Little, S., and D. Smith (1996), Fault scarp identification in side-scan sonar and bathymetry images from the Mid-Atlantic Ridge using wavelet-based digital filters, *Marine Geophysical Researches*, *18*, 741-755.

Lonsdale, P. (1997), An incomplete geologic history of the south-west Pacific basin, *Geological Society of America Abstract Programs*, *29*, 4574.

Macdonald, K., Fox, R., Alexander, R. Pockalny, R. and P. Gente (1996), Volcanic growth faults and the origin of Pacific abyssal hills, *Nature*, *380*, 125-129.

Mallat, S. (1998), *A Wavelet Tour of Signal Processing*, pp. 637, Academic Press, San Diego.

Menard, H. W. (1967), Sea floor spreading, topography and the second layer, *Science*, *157*, 923-924.

Ouillion, G. (1996), Hierarchical geometry of faulting, *Journal of Geophysical Research*, *101*, 5477-5487.

Small, C. (1998), Global systematics of mid-ocean ridge morphology, in *Faulting and magmatism and mid-ocean ridges, AGU Geophysical Monograph 106*, edited by Buck, R. Delaney, P. Karson, J. and Y. Lagabrielle, pp. 1-25, American Geophysical Union, Washington.

Starck, J., Candès, E. and D. Donoho (2002), The curvelet transform for image denoising, *IEEE Transactions on Image Processing*, *11*, 670-684.

Starck, J., Candès, E. and D. Donoho (2003), Astronomical image representation by the curvelet transforn, *Astronomy & Astrophysics*, *398*, 785-800.

Zar, J. (1999), *Biostatistical Analysis*, 4th ed., Prentice-Hall, Upper Saddle River, New Jersey.

Tables

Table 1: Table of abyssal hill population statistics

Population	Mean Azimuth (°)	Angular Deviation (°)	Mean Width (km)	Width Standard Deviation (km)
EPR 1	5.1	8.6	2.6	1.6
EPR 2	12.3	7.3	2.8	3.2
EPR 3	9.7	8.5	3.2	3.5
MAR	-12.5	12.4	4.1	4.6
OT 1	98.3	7.1	6.0	3.8
OT 2	93.9	11.9	6.2	3.0
OT 3	90.6	6.8	4.3	2.6

Figure 1: **a)** Basemap outlining the locations of the Osbourn Trough (OT), East Pacific Rise (EPR) and Mid-Atlantic Ridge (MAR) multibeam datasets used in this study. **b)** The solid line in this figure marks the location of the Osbourn Trough multibeam swath. The data collected along the yellow section of this line is plotted in Figure 3a. **c)** Same as b) except for the East Pacific Rise dataset. The three yellow sections of the EPR swath are plotted in Figures 5a-c. **d)** The location of the Mid-Atlantic Ridge multibeam swath, the yellow section of which marks the location of the multibeam data plotted in Figure 6. The dashed lines in b)-d) mark the locations of active spreading centers (EPR and MAR) or in the case of the OT dataset, the location of the extinct Osbourn spreading center.
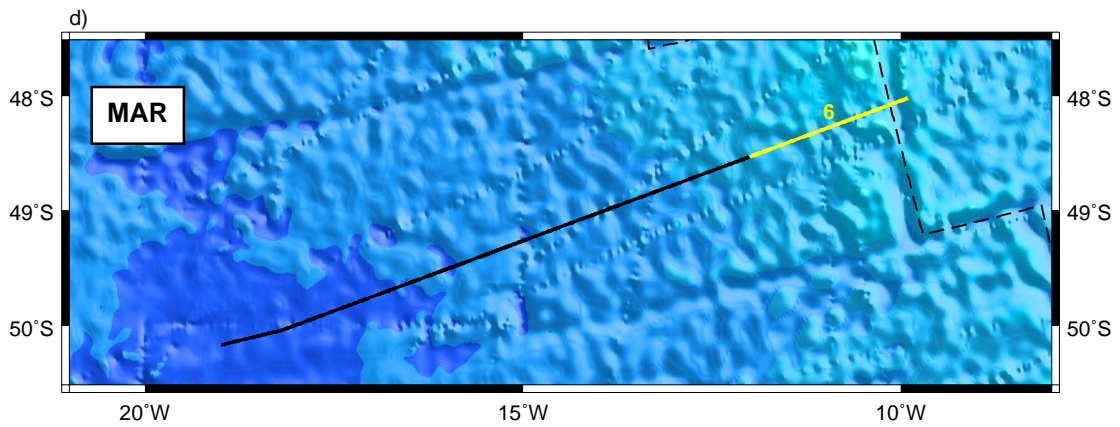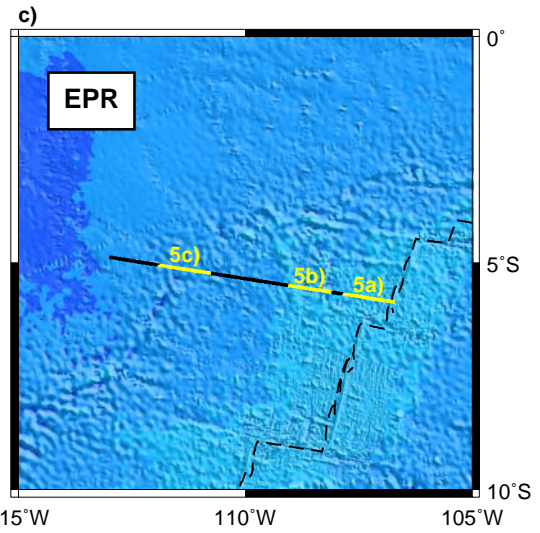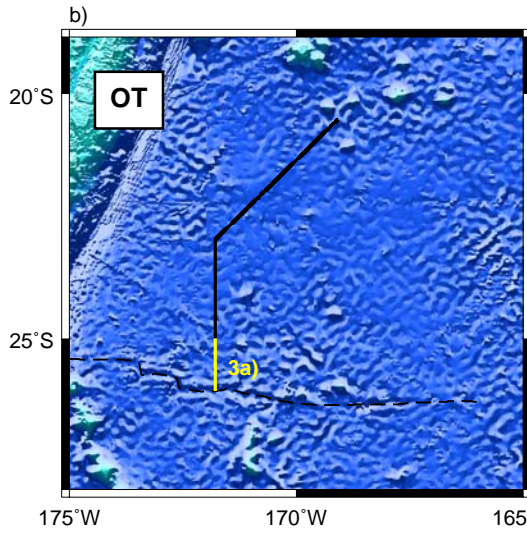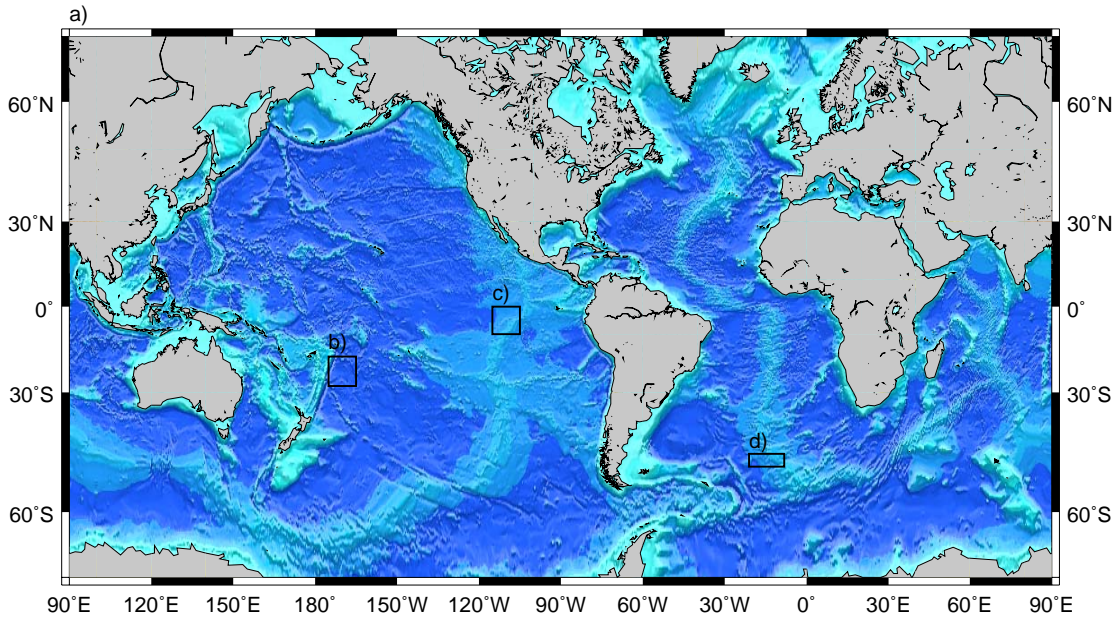
Figure 2: Example ridgelets similar to those used in our analysis. These functions are constant along one dimension and shaped like a Mexican Hat wavelet perpendicular to that dimension. Arrows indicate the directions of the x_1 and x_2 axes. θ is measured positive clockwise from x_2. **a)** Reference ridgelet: $\theta = 0$, $a = a_o$, $b = b_o$. **b)** Rotated and scaled version of a): $\theta = 20°$, $a = 2a_o$, $b = b_o$. **c)** Translated version of b): $\theta = 20°$, $a = 2a_o$, $b > b_o$.
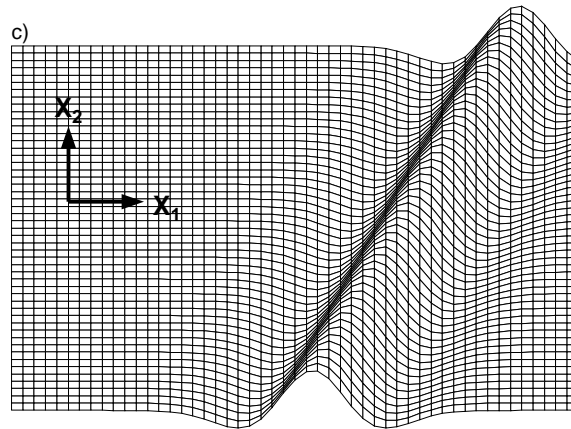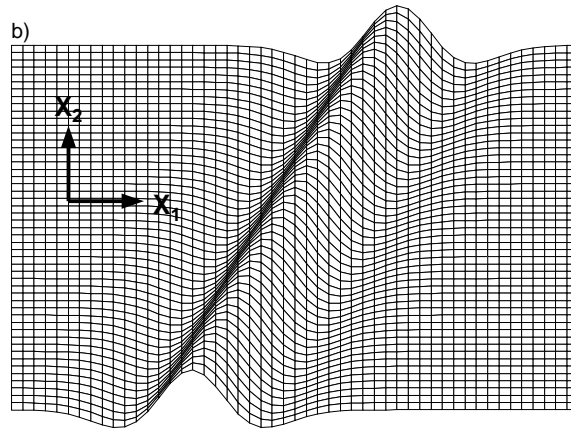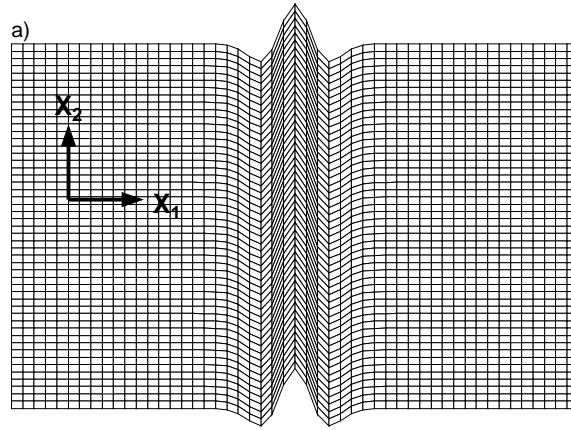
a)

b)

c)

Figure 3: a) Example dataset consisting of a section of the NBP0304 multibeam data north of the Osbourn Trough. This dataset contains two prominent seamounts near 25°37'S, numerous abyssal-hills and a single ridge contained within the axis of the Osbourn Trough at 26°6'S. **b)** Radon transform of the dataset in a). The seamounts appear as tangent function shaped features. Most of the abyssal-hills show up as maxima near 90°. However the ridge in the trough axis strikes at 120° and appears in b) as a maximum at the location appropriate to that azimuth. Note that the smallest ridges in a) form well-localized maxima in b), relative to the maxima of larger ridges. This difference in behavior between scales leads naturally to the multiscale decomposition of this data presented in c)-f). The box beneath b) shows a schematic of the Dirac ridge used in the Radon transform to analyze the data in a). Figures **c)-f)** present a particular slice through the ridgelet transform at the width indicated. A sample ridgelet corresponding to each width is plotted in the box beneath each panel at the scale of the data in a). The resolution in azimuth is best for the smallest scale abyssal hills. The location of the maxima in these slices gives a measure of the location and azimuth of a particular abyssal hill. The width at which each abyssal hill maxima has largest amplitude is the measure of the width of that abyssal hill. The locations, azimuths and widths of each maxima in the ridgelet domain are plotted on a) with a symbol consisting of a line segment parallel to the azimuth, and a superimposed I-shaped symbol at 90 degrees to the azimuth whose length equals the width location of each maxima. A sample symbol for a northeast trending 5 km wide hill is shown beneath a).
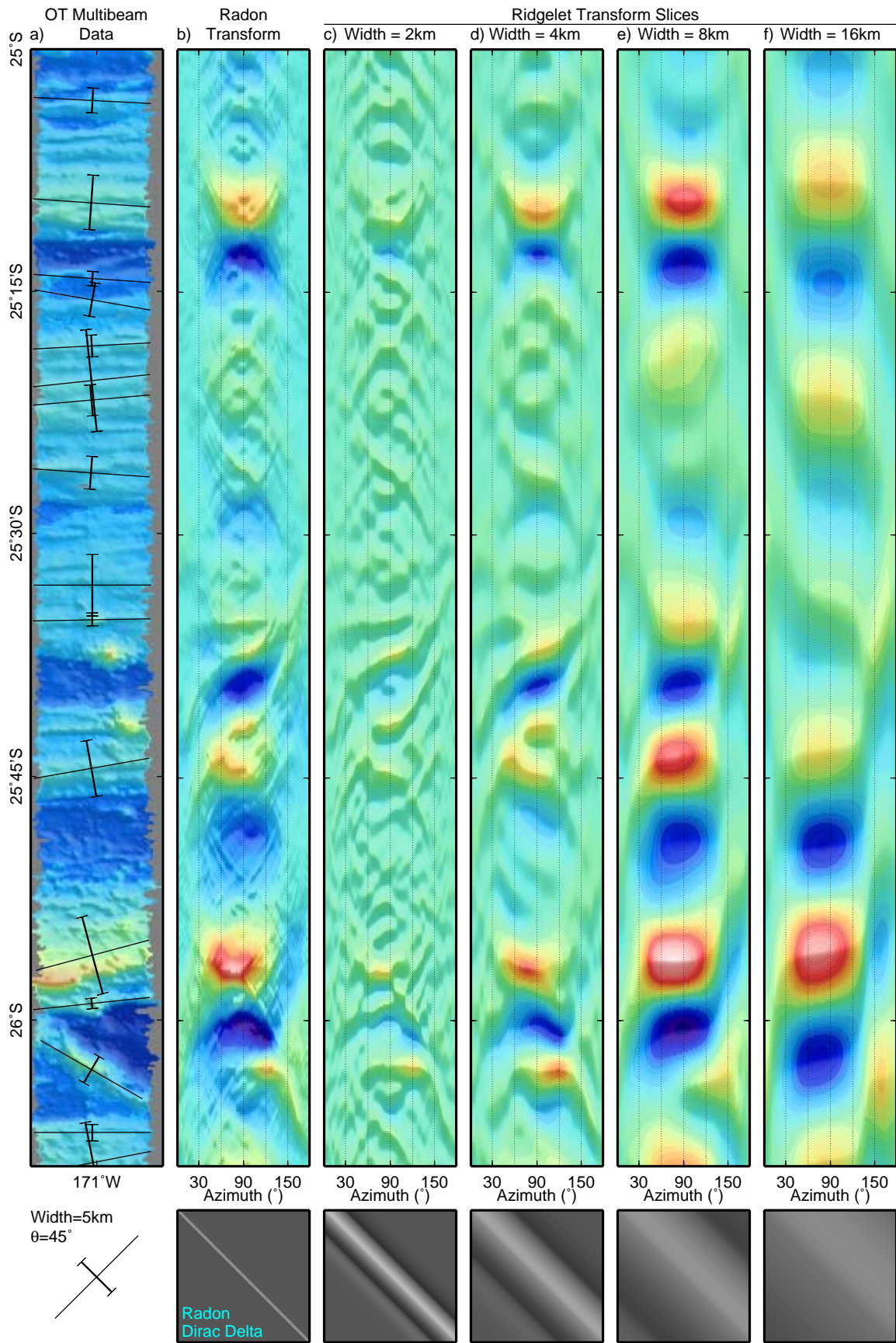
27

OT Multibeam Data b) Radon Transform Ridgelet Transform Slices
c) Width = 2km d) Width = 4km e) Width = 8km f) Width = 16km

Figure 4: Example Mexican Hat wavelet superimposed on the Radon transform of the NBP0304 data at θ=90° and the latitudes shown. The scale and translation of the wavelet match a peak in the ridgelet transform of the data. The width of the wavelet is defined as the distance between zero-crossings of the wavelet. Note also that the wavelet is effectively zero outside the region of its "effective support".
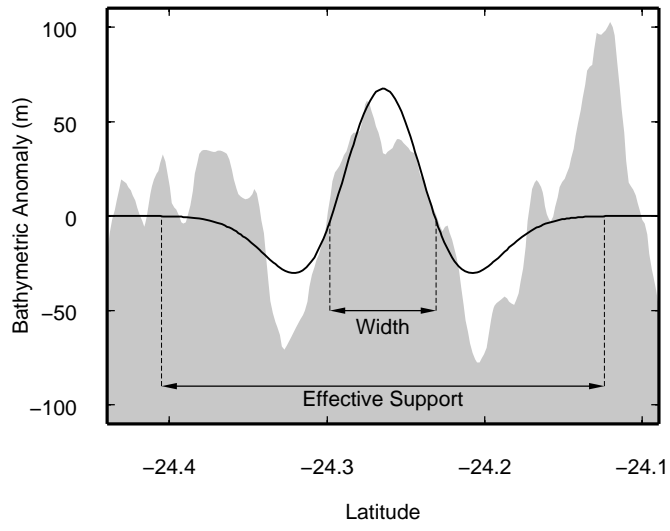
Figure 5: a) A sample of the EPR multibeam swath. The East Pacific Rise is located at 106°42'W in this figure. The location of each ridgelet maxima is plotted using the same symbol used in Figure 3a. **b)** Same as a) but for the anomalous region of seafloor fabric observed near the Yaquina Fracture Zone (FZ). **c)** Detail of the anomalous multibeam data collected near the Louis Scarp.
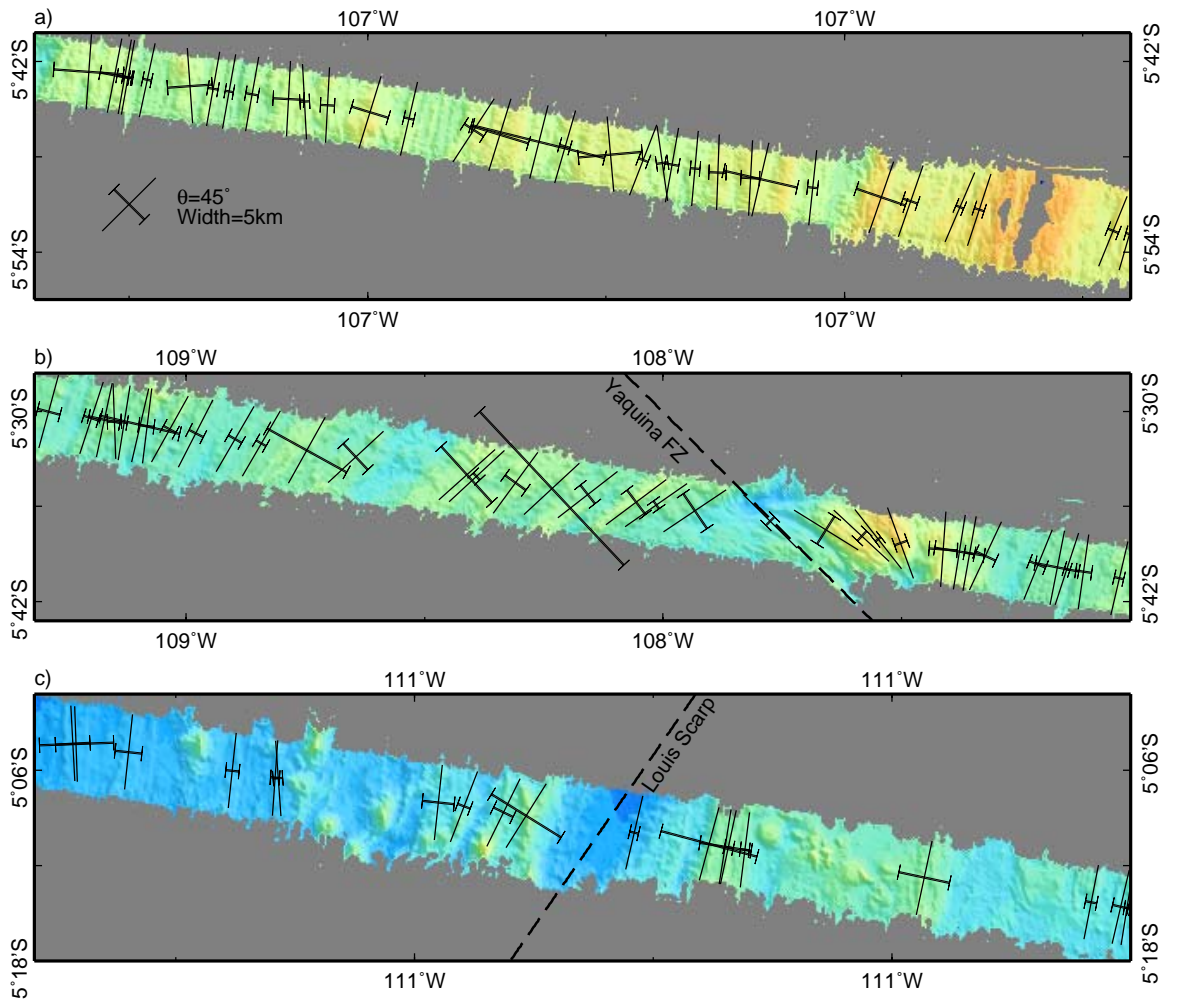
EPR Multibeam Data

a)

θ=45°
Width=5km

b)

Yaquina FZ

c)

Louis Scarp

Figure 6: A sample of the MAR multibeam swath. The Mid-Atlantic Ridge is located at 10°3'W in this figure.
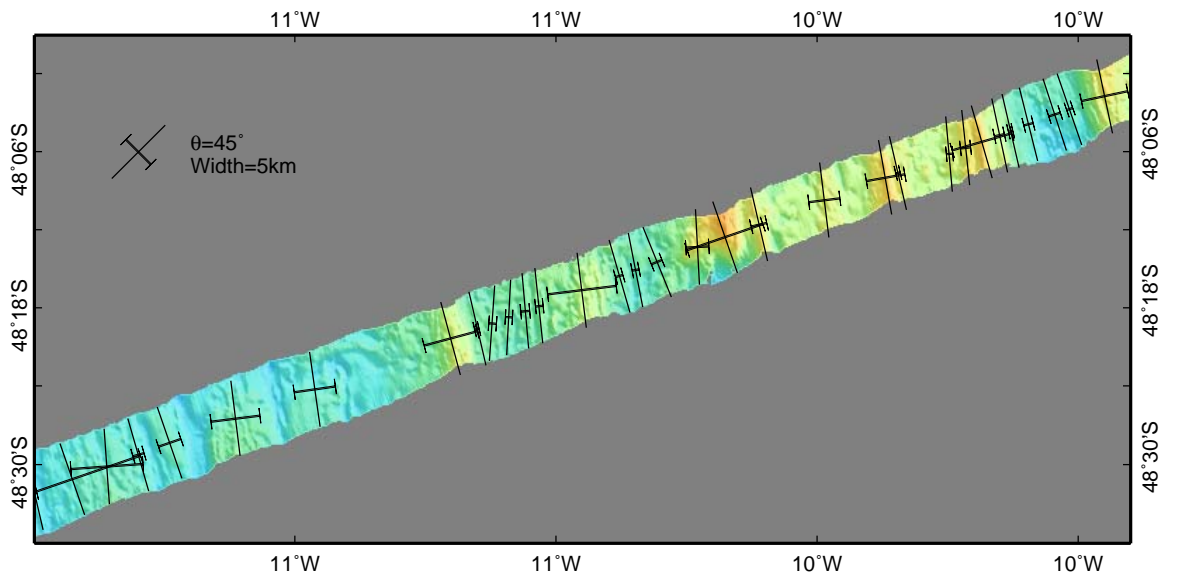
MAR Multibeam Data

Figure 7: Output of the ridgelet transform method for the EPR multibeam data. The Louis Scarp and Yaquina Fracture Zone provide natural boundaries between three populations of abyssal hills, which we denote as EPR 1, 2 and 3. **a)** Azimuths of the observed abyssal hills. The Grey lines denote the locations of the EPR 1,2 and 3 populations. For each population, the mean azimuth is plotted as a solid line and the mean +/- one angular deviation [Cain, 1989] are plotted as two dotted lines. The azimuth of the EPR abyssal hills changes across the Louis Scarp, from 5.1° for EPR 1, west of the scarp to 12.3° for EPR 2 east of the scarp, a difference that is statistically significant. With the exception of a few anomalous abyssal hills near the Yaquina Fracture Zone, the azimuth of abyssal hills does not significantly change east of the Louis Scarp, with a mean of 9.7° for the EPR 3 abyssal hills. **b)** The widths of these abyssal hills vary widely, and no clear trend or change in abyssal hill widths is observed between the three populations. The mean width of each population is plotted as a solid line. **c)** RMS amplitude of the EPR bathymetry, calculated using a 10 km-radius (solid black line) and a 20 km-radius (dashed black line) window. Also plotted is the sediment thickness along the multibeam swath taken from the NGDC global sediment database [*Divins*, 2006]. The RMS amplitude is within the range of 50-100 m for all three groups of abyssal hills, a value typical of fast spreading ridges. The RMS amplitude of bathymetry increases markedly near the locations of the Louis Scarp and Yaquina Fracture Zone.
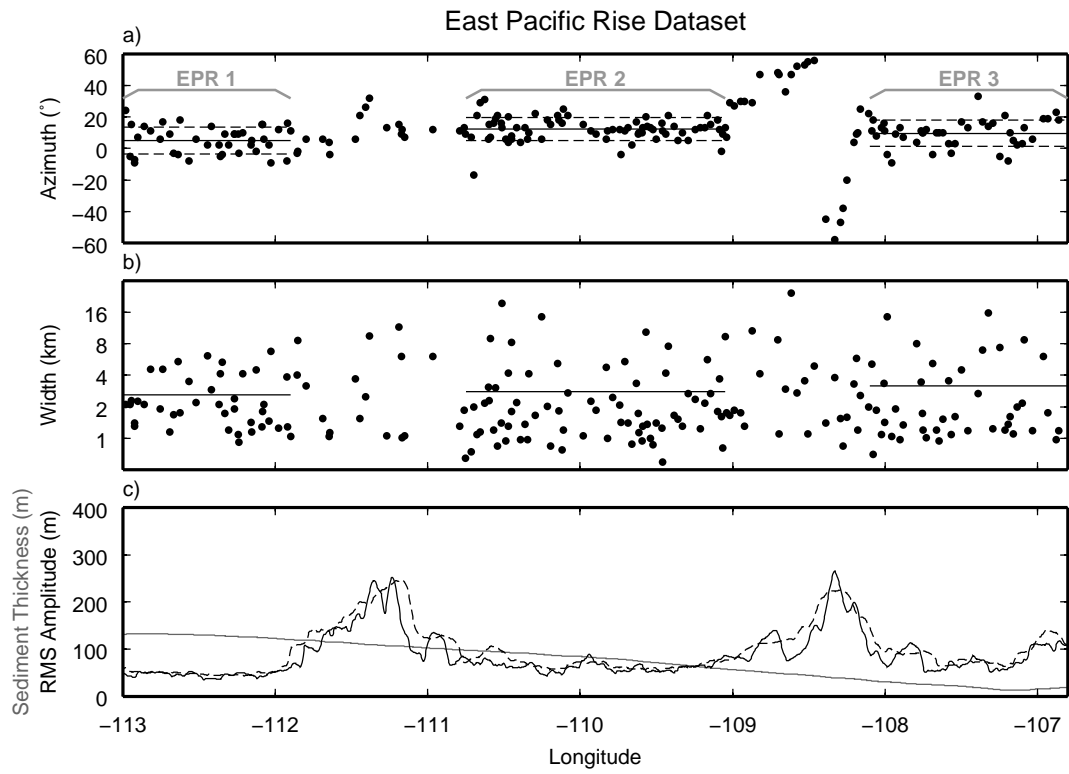
East Pacific Rise Dataset

Figure 8: Output of the ridgelet transform algorithm for the MAR multibeam data. Unlike the EPR abyssal hills there are no clear boundaries observed in the data. **a)** The azimuths of MAR abyssal hills remain relatively constant across the survey area, with a mean value of -12.5° (soild line) and an angular deviation of 12.4° (dotted lines). **b)** The widths are also scattered similar to those of the EPR abyssal hills, with a slightly higher mean width of 4.1 km (solid line). **c)** The RMS amplitude near the MAR axis, which is typical of slow spreading rates. The RMS amplitude decreases steadily with increasing distance to the MAR. This decrease in smoothness is correlated with sediment thickness, which increases with distance from the ridge. The decrease in RMS amplitude therefore is attributed to the smoothing effect of thick sediment cover.
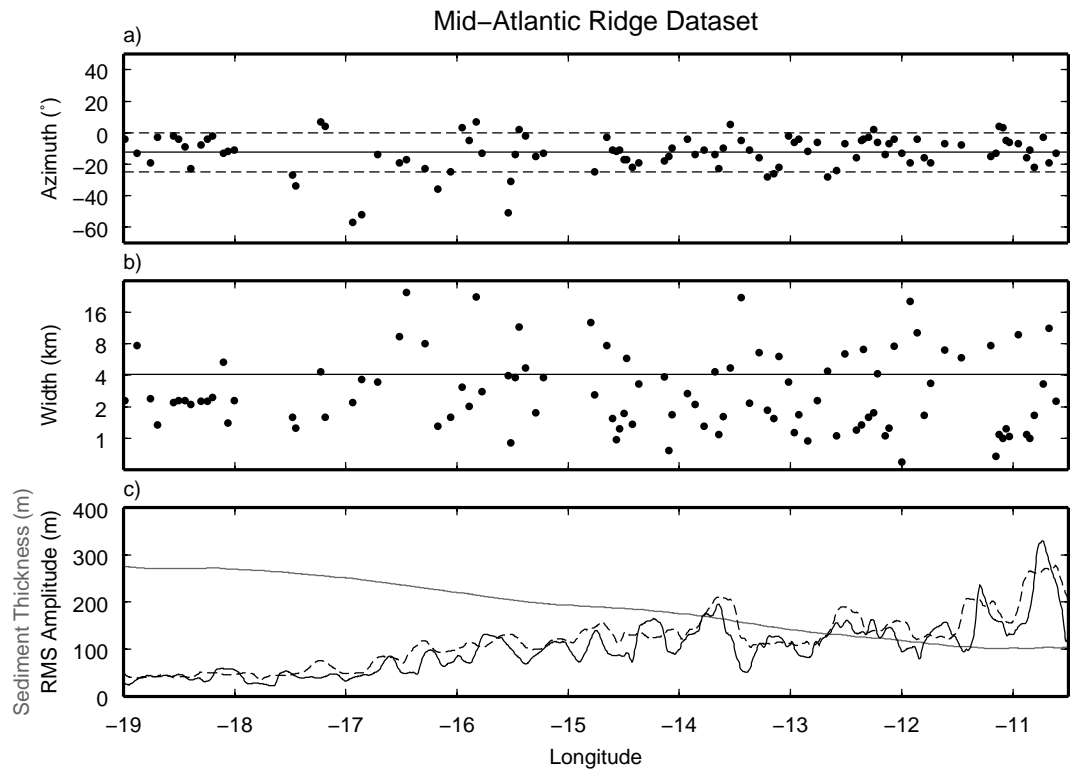
Mid−Atlantic Ridge Dataset

Figure 9: Output of the ridgelet transform algorithm for the OT multibeam data. **a)** The abyssal-hills in this figure have been separated into three groups, based on latitude, as shown by the grey lines. Group OT 1 has mean trend 98.3°, group OT 2 has mean trend 93.9° and group OT 3 has mean trend 90.6°. Watson-Williams tests [*Zar*, 1999] show that groups OT 1 and OT 3 have significantly different means, however, group OT 2's mean is not significantly different from either group OT 1 or OT 3. This change in abyssal-hill trend may be evidence of either a change in the spreading direction of the Osbourn paleo-spreading center or the presence of a triple junction trace between 22°S and 24°S. Unlike the relatively sudden change in abyssal-hill trend at the Louis Scarp, this transition in trend occurs over a larger scale. **b)** Widths of abyssal hills near the Osbourn Trough. There are no significant trends across the survey area. **c)** The RMS amplitude of abyssal hills along the survey. The amplitude is highest near the Osbourn Trough axis, and may indicate a change in spreading rate prior to extinction of the Osbourn paleo-spreading center.

Osbourn Trough Dataset
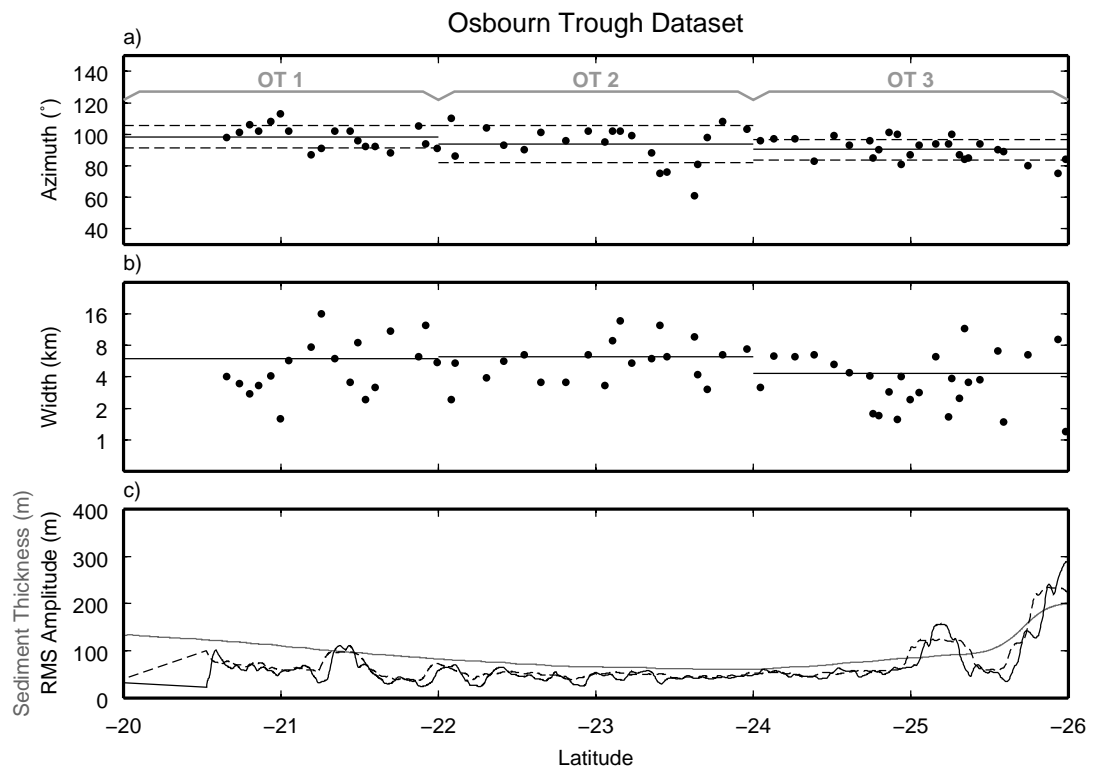
C h a p t e r   3

HISTORY OF THE CRETACEOUS OSBOURN SPREADING CENTER

Nathan J. Downey, Joann M. Stock, Robert W. Clayton and Steven C. Cande

Abstract

The Osbourn Trough is a fossil spreading center that rifted apart the Manihiki and Hikurangi Plateaus during Cretaceous time. Previous models of the Osbourn Trough are based on data collected near the trough axis, only constraining the history of the Osbourn spreading center during the last few Ma of spreading. Our dataset includes multibeam data collected northward to the Manihiki Plateau, allowing us to examine seafloor morphology created during the entire active period of the Osbourn Spreading center, as well as several additional multibeam datasets that provide the opportunity to examine the relationship between the Osbourn paleo spreading center and the Cretaceous Pacific-Phoenix ridge. The axial gravity of the trough is similar to the gravity found at other extinct slow-intermediate spreading rate ridges. Magnetic models indicate that spreading at the trough ceased during Chron C34. Abyssal-hill trends indicate that spreading direction during the early history of the Osbourn spreading center occurred at 15°-20°. The east-west component of this spreading explains the modern east-west offset of the Manihiki and Hikurangi Plateaus. Spreading rotated to 2°-5° prior to extinction. Abyssal-hill RMS amplitudes show that a decrease in spreading rate, from >7 cm/yr to 2-6 cm/yr full-spreading rate, occurred ~2-6 Ma prior to ridge extinction. Our data analysis is unable to determine the exact spreading rate on the Osbourn Spreading center prior to the slowing event. Our model resolves the conflict between regional models of the Osbourn region with models based on its axial characteristics by showing that spreading at the Osbourn spreading center was decoupled from Pacific-Phoenix spreading.

1. Introduction

The Osbourn Trough is a fossil Cretaceous spreading axis located in the Southwest Pacific Basin (Figure 1). It lies between the Manihiki and Hikurangi Plateaus, and intersects the Tonga-Kermadec Trench and Louisville Ridge at its western boundary. The Osbourn Trough was identified relatively recently [*Lonsdale*, 1997] due to a weak bathymetric expression, an absence of magnetic field reversal anomalies, and a lack of ship track data. The drilling vessel *Glomar Challenger* surveyed the Osbourn Trough at 26°S, 169°W during Deep Sea Drilling Program (DSDP) leg 91 [*Menard et al.*, 1987]. At the time of this survey the length of the Osbourn Trough was unknown, making its interpretation difficult. Global gravity datasets showed that the trough is characterized by a negative axial gravity anomaly, revealing the full extent of the Osbourn Trough for the first time [*Lonsdale*, 1997; *Sandwell and Smith*, 1997].

Lonsdale [1997] hypothesized that the Osbourn Trough is an extinct spreading center, but that result was controversial due to limited data coverage (e.g., Small and Abbott [1998]). Subsequent ship track studies [*Billen and Stock*, 2000], however, showed that the trough has morphology typical of extinct spreading ridges. The Osbourn paleo-spreading center formed when a large oceanic plateau rifted into several pieces, resulting in the creation of the Manihiki and Hikurangi plateaus [*Lonsdale*, 1997], a hypothesis that is supported by studies of the two plateaus [*Hoernle et al.*, 2004; *Mortimer and Parkinson*, 1996; *Taylor*, 2006]. Mortimer et al. [2006] present isotopic data which constrain this rifting event to prior to 115 Ma. Spreading at the Osbourn ridge presumably ceased when the Hikurangi plateau collided with the Chatham Rise paleo-subduction zone [*Lonsdale*, 1997].

The spreading rate and extinction age of the Osbourn paleo-spreading center remain controversial. Data collected at the trough axis imply a slow spreading rate and a late extinction age for the Cretaceous Osbourn spreading center. Conversely, attempts to determine the role the Osbourn spreading center plays in the tectonic history of the Southwest Pacific Basin [*Eagles et al.*, 2004; *Larter et al.*, 2002] require either a fast spreading rate for the Osbourn ridge, with a corresponding early extinction age, or complex plate geometries. A fast spreading rate is expected if the Osbourn Trough is

indeed an extinct section of the Pacific-Phoenix ridge as postulated by Lonsdale [1997]. This conflict between models results, in part, because the region surrounding the Osbourn Trough formed during the Cretaceous Long Normal Polarity Interval (Chron C34, 121-83Ma; [*Cande and Kent*, 1995]) and therefore lacks the magnetic reversal anomalies useful for determining plate histories. This deficiency has led to the formulation of models based solely on the axial characteristics of the Osbourn Trough, which may only be representative of the last few Ma before the trough's extinction. Confusion also surrounds the origin of several features of the region surrounding the trough. The Wishbone Scarp (Figure 1) is difficult to explain as a fracture zone, as it is very prominent south of the trough but there is no conjugate feature observed in the gravity field north of the trough. Furthermore the Wishbone Scarp forks to the south, which is not a feature typical of fracture zones. Mortimer et al. [2006] assert that the western arm of the Wishbone Scarp is a fracture zone that later became the location of incipient subduction. East of the Wishbone Scarp there is a linear gravity anomaly that is the northern extension of a triple junction trace (Figure 1). The identification of this feature as a triple junction trace is based on the differing distances between Chrons C34y and C33y on either side of this gravity lineation. The reconstruction of Eagles et al. [2004] shows this triple junction separated the Phoenix, Pacific and Charcot plates during the early Cretaceous.

The first extensive marine survey of the Osbourn Trough was carried out aboard the United States Antarctic Program's Research Vessel Icebreaker (*R/VIB*) *Nathaniel B. Palmer* (cruise NBP9806; [*Billen and Stock*, 2000]). Magnetic anomalies were interpreted to indicate that the Osbourn Trough ceased spreading at 71 or 83 Ma [*Billen and Stock*, 2000]. Assuming that rifting between the Manihiki and Hikurangi plateaus began shortly after their formation at the beginning of Chron C34 (121 Ma) Billen and Stock [2000] estimated an average full spreading rate (FSR) for the Osbourn paleo-spreading center of 6-8 cm/yr. This spreading rate is consistent with the trough's morphology, as imaged by multibeam bathymetry. The model proposed by Billen and Stock [2000] is similar to that originally proposed by Lonsdale [1997] except that he calculated a 15 cm/yr full spreading rate based on a 105 Ma extinction age. This

extinction age was hypothesized to correspond to the time when the Hikurangi plateau collided with the Gondwana margin.

Sutherland and Hollis [2001] estimate that the crust at DSDP site 595A (Figure 1) formed at 132-144 Ma based on the biostratigraphy of the deepest sediments cored. They use these estimates in conjunction with the observations of Billen and Stock [2000] and the 63°S paleo-latitude of creation of the crust [*Menard et al.*, 1987] to propose a different model of the history of the Osbourn spreading center. In this model, Sutherland and Hollis [2001] propose that two spreading centers were active in this region prior to 120 Ma, the Pacific-Phoenix spreading center and a spreading center to the south separating the Phoenix plate from a newly-inferred plate, which they dub the Moa Plate. Sutherland and Hollis [2001] propose that the crust at DSDP site 595 was created at the Phoenix-Moa ridge at ca. 137 Ma. After eruption of the Manihiki and Hikurangi plateaus spreading continued on the Phoenix-Moa ridge, which separated the two plateaus. The Osbourn Trough is interpreted to be the extinct western section of this ridge. In order to explain the close proximity of the Osbourn Trough and DSDP site 595, Sutherland and Hollis [2001] argue that the East Wishbone Scarp is the remnant of a transform fault that offset the Phoenix-Moa ridge, implying a ~50 Ma age discontinuity at a fracture zone west of DSDP site 595.

Recently, as data from the regions surrounding the Osbourn Trough became more available, tectonic models of these regions have been formulated. These models provide a regional framework into which any tectonic model of the Osbourn Trough must fit. Larson et al. [2002] provide a constraint on the location of the Pacific-Phoenix-Farallon triple junction (PAC-PHO-FAR, Figure 1) throughout Chron C34 by examining the changes in abyssal-hill fabric east of the Osbourn Trough. The geometry of this triple junction, along with the area of seafloor created during Chron C34 implies that spreading at the Pacific-Phoenix ridge occurred at 18-20 cm/yr FSR. They also show a change in spreading direction at the Pacific-Phoenix spreading center. Prior to ~100 Ma spreading occurred along an azimuth of ~171°, whereas the spreading direction in regions created after 100 Ma averaged ~164°.

Eagles et al. [2004] present a detailed high-resolution reconstruction of the Pacific-Antarctic ridge and associated plate kinematics from 90-45 Ma. The earliest part of this reconstruction presents a model of the region south of the Osbourn Trough that provides a late-stage boundary for models of the Osbourn region. Eagles et al. [2004] also argue that the spreading directions observed by Larson et al. [2002] cannot explain the east-west offset of the Hikurangi and Manihiki plateaus.

Taylor [2006] presents a model of the Ellice Basin, a region west of the Manihiki Plateau (Figure 1). This model shows that the Manihiki and Hikurangi Plateau were not only conjugate to each other at the time of formation, but that they were also conjugate to the Ontong Java Plateau. This single large plateau fragmented into at least three parts around 119-123 Ma. Taylor's [2006] model thus provides an early boundary condition for models of the Osbourn spreading center.

Mortimer et al.'s [2006] model of the history of the western arm of the Wishbone Scarp asserts that this scarp formed as a fracture zone prior to 115 Ma, was later the location of oblique convergence resulting in the formation of an intraoceanic subduction zone at ca. 115 Ma, and evolved into a rift margin at 92-98 Ma before becoming tectonically inactive. These results constrain the age of the formation of the Osbourn paleo-spreading center to before 115 Ma. Because the West Wishbone Scarp would have been in close proximity to the Manihiki and Hikurangi plateaus at this time, the observations of Mortimer et al. [2006] provide an important constraint on the early history of the Osbourn spreading center.

Ideally a model of the Osbourn spreading center should be compatible with the history of the Pacific-Phoenix-Farallon triple junction [*Larson et al.*, 2002], provide temporal and spatial continuity between the models of Taylor [2006] and Eagles et al. [2004] and be consistent with the observations of Mortimer et al. [2006]. A crucial observation for constraining the timing of this model is the age of the crust at DSDP sites 595 and 596 (Figure 1). $^{40}Ar/^{39}Ar$ analyses of the crust cored at site 595/6 yield a minimum age of 100 Ma [*Menard et al.*, 1987]. This estimate is compatible with the 132-144 Ma age of the radiolaria found in the basal sediments (9 m above basement) of hole 595A

[*Sutherland and Hollis*, 2001]. However, the radiolarian fossils in the deepest sediments cored at hole 595 (1.5 m above basement) indicate an age of 94-99 Ma.

In this paper we present a new set of ship track surveys of the Osbourn region. These data represent the most extensive survey of the Osbourn Trough thus far and include data collected northward to the Manihiki Plateau (Figure 1). This dataset offers us the opportunity to examine regions created continuously at the Osbourn spreading center from its formation to its extinction. We analyze and interpret these data and formulate a new tectonic model that is compatible with the regional tectonics of the Southwest Pacific Basin. We find that contrary to the models of Billen and Stock [2000] spreading at the Osbourn spreading center ceased prior to the end of Chron 34. An earlier extinction age matches the models of Eagles et al. [2004]. The reduction of the Osbourn spreading center's spreading rate as it approached extinction may be typical of ridge extinction events. This change in spreading rate explains the axial morphology of the Osbourn Trough. We also observe a change in spreading direction throughout the period of active spreading at the Osbourn Trough, which accounts for the east-west offset of the Manihiki and Hikurangi plateaus [*Eagles et al.*, 2004]. Furthermore abyssal hill trends imply that the Osbourn Trough is not an extinct section of the Pacific-Phoenix ridge and therefore that the region of seafloor containing the Hikurangi plateau must have formed a plate separate from the Phoenix plate during the active period of the Osbourn spreading center.

2. Data

We used ship track gravity, magnetic and seismic data obtained during five separate cruises in this study (Figure 1). Three of these cruises were aboard the *R/VIB Nathaniel B. Palmer*. Two of these *Palmer* cruises (NBP0304 and NBP0207) were transits, only crossing the Osbourn Trough once, while the third (NBP0304B) carried out an extensive survey at a right-stepping offset in the Trough located near 172.7°W. One Cruise (KM0413) was a transit carried out aboard the University of Hawaii's School of Ocean and Earth Science and Technology's (SOEST) Research Vessel *R/V Kilo Moana*. The fifth cruise (COOK20) was a transit aboard the Scripps Institution of Oceanography's

Research Vessel *R/V Melville*. We also use magnetic anomaly data collected during NBP9806A (Figure 1) [*Billen and Stock*, 2000].

During all five cruises, magnetic field strength and multibeam bathymetry were collected. Swath width of the multibeam surveys averages ~15-20 km for the 4000-6000 m water depths typical of this region of the Southwest Pacific Basin. The processed multibeam data obtained near the Osbourn Trough are shown in Figure 2 superimposed upon bathymetry predicted from satellite altimetry [*Smith and Sandwell*, 1997]. Profiles of the magnetic field strength recorded during our cruises, along with those of NBP9806A [*Billen and Stock*, 2000] are plotted in Figure 3a. Plotted in Figure 3b are the observed magnetic field strength data after being reduced to the pole (skewness = 60°).

In addition gravity data were collected during the three *Palmer* cruises and COOK20. These data are plotted in Figure 4, superimposed upon a series of north-south profiles taken from a global satellite dataset [*Sandwell and Smith*, 1997]. There is good agreement between the satellite data and the data collected during the three easternmost cruises. A gravimeter malfunction that occurred during NBP0304b may explain the poor agreement of the satellite data with the NBP0304b ship track data.

Single channel seismic (SCS) data were collected during NBP0207 between latitudes 27°S and 25°S; during NBP0304B, a multichannel seismic (MCS) survey was carried out at the locations shown in Figure 2. The SCS survey carried out during NBP0207 utilized two GI guns with a 3.71 litre capacity, capable of producing energy up to 150 Hz. Ship speed during this survey was 11.1 km/h, with a shot spacing of 37 m. The NBP0304b MCS survey consisted of two north-south lines flanking the 172.7°W offset in the Osbourn Trough and two short east-west lines that cross this offset. A much larger airgun source was used during this survey to image subcrustal structure beneath the Osbourn Trough. A 6 bolt-airgun array with a 34.8 litre total capacity and a shot spacing of 47 m was used for a source. 45 channels of data were recorded with a group spacing of 25 m. The seismic data exhibit a 2-reflector signature on all seismic lines collected. The uppermost reflector is the seafloor, while the lower reflector 0.0-0.2 s beneath is the

sediment-basement contact. Despite the large source sizes used and high number of channels during NBP0304b, no structures are resolved below the sediments.

3. Magnetic anomalies

The magnetic field strength profiles of Figure 3a are shifted such that they are aligned along the axis of the Osbourn Trough. If the observed anomalies are due to magnetic field reversals, there should be a correlation among all the profiles. However, the magnetic field strength profiles adjacent to each other correlate better than those far apart. In particular, NBP0304 correlates better with both NBP0207 and COOK20 (correlation coefficient, R = 0.65 and 0.79 respectively) than it does with either of the west and central profiles of NBP9806 (R = 0.34 and 0.20) even though these two NBP9806 profiles correlate well with each other (R = 0.75). Billen and Stock [2000] present models of the NBP9806 profiles that predict either a 71 Ma (preferred) or an 83 Ma extinction age for the Osbourn spreading center. However, because the correlation between the profiles in Figure 3a disappears with increasing distance between profiles, the models of Billen and Stock [2000] do not predict the shape of our magnetic anomaly data. The lack of correlation across our survey area indicates that the source of the observed anomalies cannot be magnetic field reversals, casting doubt on the extinction age estimates of Billen and Stock [2000] and on paleo-spreading rates inferred from those estimates.

The phase-shifted profiles (Figure 3b) have a strong symmetry about the axis of the Osbourn Trough indicating that the magnetic anomalies are most likely due to magnetic field strength fluctuations within Chron C34. Similar fluctuations have been observed within Chron C5 [*Bowers et al.*, 2001]. We therefore conclude that the Osbourn spreading center stopped spreading some time during Chron C34 (121-83 Ma); however, the exact extinction age cannot be determined by analysis of the observed magnetic anomalies.

4. Gravity models

4.1 Spreading rates from gravity measurements

Active spreading centers are generally characterized by a linear residual gravity anomaly coincident with the ridge axis. The shape of this anomaly depends on the ridge's spreading rate [*Small*, 1994; *Watts*, 1982]. A similar pattern is observed in the gravity fields of extinct spreading axes [*Jonas et al.*, 1991].

Jonas et al. [1991] interpret the central gravity lows observed at extinct spreading centers as changes in crustal geometry beneath the axial valley. They use this model to successfully explain the residual gravity of several extinct spreading centers. Their model is based on the observation that the basal portions of the oceanic crust emplaced at the Bay of Islands ophiolite complex formed at high pressures within the mantle. Elthon et al. [1982] propose a model in which these portions form at a depth of ~30 km beneath the ridge axis, flow upwards along an upwelling conduit of material as the oceanic plates rift apart, and are emplaced at the base of the oceanic crust. Jonas et al. [1991] propose that this conduit becomes frozen upon ridge extinction displacing higher density mantle material resulting in a gravity low. Recently, Müller et al. [2005] were able to model the gravity field of the Adare Trough using this Moho topography model.

Seismic reflection and refraction data obtained at the Labrador Sea paleo-spreading center indicate that crustal thickness decreases toward the ridge axis [*Srivastava and Keen*, 1995]. Magnetic reversal anomalies observed near the ridge axis indicate that the region of reduced crustal thickness (4-6 km vs. 6-7 km thick) was formed during a 13 million year period of slower spreading (0.6 cm/yr vs. 2 cm/yr) immediately prior to ridge extinction. This crustal thinning is accommodated by extension along numerous faults in the crust of this region and seismic velocities at the axis are anomalously low through the crust and upper 3 km of the mantle [*Srivastava and Keen*, 1995]. Osler and Louden [1992] hypothesize that these regions have undergone serpentinization resulting in lower densities and seismic velocities, a process that may have been aided by the presence of several faults that penetrate the crust near the ridge axis. The regions of

altered density may be sufficiently large to explain the gravity anomaly observed at the Labrador Sea paleo-spreading center [*Osler and Louden*, 1992].

Jung and Vogt [1997] observe that the crust thins at the axis of the Aegir ridge, located in the Norwegian Sea, similar to the observations of Osler and Louden [1992] at the Labrador ridge. Uenzelmann-Neben et al. [1992] observed a change in the amplitude of sediment-layer reflections at the axis of the Aegir ridge. This change is due to a change in pore fluids in the sediments of the axial region. Observing that the Aegir Ridge is characterized by a residual gravity low, Uenzelmann-Neben et al. [1992] infer that the sediment pore fluids of the axial region were released from a crustal magma chamber as it solidified during its extinction. The residual gravity low at the Aegir Ridge may therefore be due to a low density region within the crust.

4.2 Osbourn Trough gravity

The gravity field of the Osbourn Trough is similar to that observed at the Labrador Sea, Aegir Ridge and other extinct spreading centers. In Figure 4, the axis of the Osbourn Trough coincides with the gravity low centered at 26°S east of 172.5°W. The trough shifts northward west of this point and coincides with a similar gravity low at 25.75°S. In fact the Osbourn Trough is a more prominent feature in gravity datasets than in bathymetric datasets and it is not surprising that the trough was not originally identified on bathymetric maps but rather was recognized by its axial gravity anomaly [*Lonsdale*, 1997].

The observed gravity profiles (Figure 4) are composed of several components. A 15-20 mGal, 30 km wavelength gravity low centered on the axis of the Osbourn Trough is seen in all shiptrack and satellite profiles. Superimposed upon this, the gravitational expression of abyssal hills correlates with bathymetry and is reflected as 5-10 mGal ~20 km wavelength oscillations present throughout the profiles (compare the seismically-determined bathymetry in Figures 5a-c with the observed gravity). The longest wavelength components of the gravity field could be caused by changes in crustal thickness or large-scale density anomalies located in the mantle. The amplitude of the

axial gravity anomaly cannot be explained by bathymetry and sediment cover. Billen and Stock [2000] argued that the axial gravity anomaly seen at 173.7° W would require an increased sediment thickness in the trough axis, and they predicted that at this location, to account for the gravity anomaly, sediment cover would have to be 350 m thick. Our seismic data show, however, that sediments in the trough axis at the locations of our seismic surveys (Figure 2) are only 60-70 m thick. Note also that single-channel seismic reflection data obtained during Deep-Sea Drilling Project (DSDP) leg 91 by the drilling vessel *Glomar Challenger* demonstrate that the Osbourn Trough at 26°S 169°W is 500 m deep and contains a thin (<70 m) sediment infill [*Menard et al.*, 1987]. The thin sediment infill of the Osbourn Trough implies that the axial anomaly must be due to density anomalies in the crust or uppermost mantle—density anomalies that may be explained by the serpentinization, Moho topography or low density crustal body models that have been invoked to explain the gravity anomalies of other extinct spreading centers.

4.3 Gravity models of the Osbourn Trough

Nettleton's [1939] method of gravity interpretation uses the topography and free air anomaly of a region to determine average subsurface density. This method is valid as long as topography and density do not correlate, such as would occur if the topography were locally compensated. In our analysis we extend Nettleton's [1939] method to more complex models. The model domain is separated into several sub-domains each of which has a constant density and represents a particular model element (e.g. sediments, crust etc.). The gravitational field of each sub-domain for a unit density is calculated using Parker's [1972] method. The modeled gravity is given by the equation:

$$g(x) = \sum_{j=1}^{N} \rho_j \varphi_j(x) + b \qquad (1)$$

where g(x) is the modeled gravity along the profile; $\phi_j(x)$ is the unit density gravity field of the jth sub-domain; N is the total number of sub-domains; b is the average background gravity of the region; and ρ_j is the density of the jth model element. This approach requires us to prescribe only the shape of the model elements; the densities (ρ_j) are

determined by a least squares inversion of the measured gravity field. Our method requires non-local topographic compensation, and at the wavelengths considered in our model (≤ 50 km) this requirement is satisfied for typical oceanic regions [*Watts*, 2001].

To incorporate the seismic observations into this modeling process, the water-bottom and sediment-basement interfaces were interpreted from the migrated seismic sections. A time to depth conversion was then carried out using a 1500 m/s velocity for the water column and a 1600 m/s velocity for the sediments, based on measurements at DSDP site 204 (Figure 2 [*Burns*, 1973]). This time-depth conversion provides the geometry of the sediment and basement layers in the gravity models.

We have constructed three models that predict the Osbourn Trough's gravity field (Figure 5 and Table 1). Model 1 contains an elliptical low-density body within the crust. A tradeoff exists between the density contrast of this body with the crust and the thickness of this ellipse; however, for a given depth, the width remains fixed regardless of density contrast. The depth of this ellipse can also vary without affecting the calculated densities. Deeper ellipses are narrower than shallow ones.

The limit of a superposition of a large number of ellipses at a range of depths leads to model 2. This model presents serpentinization as the cause of the axial gravity anomaly. The geometry of this serpentinized zone is well-constrained by the gravity data, assuming that it extends from the surface of the crust to the Moho. A depth of alteration greater than or less than the Moho would yield density contrasts between the altered zone and normal crust less than or greater than those in Table 1, respectively.

Our third model is based upon the model of Jonas et al. [1991], with the gravity signature of the Osbourn Trough resulting from the geometry of the Moho alone; no low-density anomaly within the crust is required. There is a tradeoff between the width and depth extent of the crustal root. If the root extends to 30 km deep, as postulated by Jonas et al. [1991], it would become a conduit only a few kilometers wide.

These three models may be overly simplistic, but they are a useful starting point for examining the gravity anomalies. We have assumed constant density within each model

element but our method is insensitive to vertical density gradients. Models that contain such gradients and also preserve the density contrasts between elements produce identical results. Each of our three models explains observations equally well and yields densities for their common elements (crust, mantle and sediments) that are similar (Table 1).

Our gravity models do not allow us to draw unique conclusions about the density structure of the Osbourn Trough. They do, however, show that the gravity field of the Osbourn Trough is typical of that at other extinct spreading axes. Furthermore, the amplitude of the axial anomaly is similar to that observed at the axes of extinct ridges with a 5.5 cm/yr full paleo-spreading rate [*Jonas et al.*, 1991]. This estimate provides an important constraint on the history of the Osbourn spreading center immediately prior to extinction.

5. Abyssal-hill fabric

5.1 Spreading rate and direction from abyssal-hill fabric

Abyssal hills are elongate ridges on the ocean floor whose shape varies by region [*Goff and Jordan*, 1988; *Hayes and Kane*, 1991; *Menard*, 1967]. They are created at spreading centers and form the uppermost layer of oceanic crust and, post-creation, form a series of flanking ridges whose long axis parallels the spreading center. The primary control on abyssal-hill morphology is faulting, which occurs at mid-ocean ridges shortly after crustal formation [*Buck and Polikov*, 1998; *Goff et al.*, 1995; *Macdonald et al.*, 1996]. This faulting process is controlled by the stress state at the ridge, leading to a correlation between abyssal-hill shape and ridge characteristics [*Goff*, 1991; *Goff et al.*, 1997; *Kriner et al.*, 2006]. These characteristics include spreading rate, spreading direction and ridge axial-valley morphology. Thus evaluating abyssal-hill morphology makes it possible to reconstruct the tectonic history of a region in the absence of magnetic reversal anomalies [*Menard*, 1967]. It is not possible, however, to directly determine seafloor ages from abyssal-hill morphology, making it necessary to infer ages from other data types (e.g. biostratigraphy and isotopic dating of core or dredge samples) in regions devoid of magnetic reversal anomalies.

During their creation, the long axes of abyssal hills preferentially align with the trend of the ridge; therefore, because spreading is generally perpendicular to the ridge axis, the direction normal to abyssal-hill strike is an indicator of paleo-spreading direction. The alignment of abyssal hills is not perfect, however, and some scatter of azimuths is observed within regions created at a single spreading center. This scatter makes is necessary to define regions of relatively constant trend over which a single estimate of abyssal hill trend can be made. By observing where abyssal-hill trends change from generally north-south to east-west, Larson et al. [2002] were able to determine the spreading directions of the Pacific-Phoenix and Pacific-Farallon spreading centers during Chron C34.

Menard [1967] observed that the root-mean-square (RMS) amplitude of abyssal hills negatively correlates with the spreading rate of the parent ridge during abyssal-hill formation. Later studies [*Goff*, 1991; *Goff et al.*, 1997; *Hayes and Kane*, 1991] confirm this correlation for slow spreading ridges with RMS amplitudes varying from ~220 m for regions created at ridges with a full spreading-rate (FSR) of 2 cm/yr, to ~60 m for regions created at ridges with spreading at 7 cm/yr FSR. Goff et al. [1997] find that this correlation breaks down for areas formed by ridges spreading faster than 7 cm/yr. Faster-spreading (>7 cm/yr FSR) ridges produce seafloor whose RMS amplitude is 50-60 m and independent of spreading rate.

Abyssal-hill width is defined as the horizontal scale of abyssal hills measured perpendicular to the hill's azimuth. Goff et al. [1991; 1997] observe that as abyssal hills get higher they also get wider. As a result, there is also a correlation between abyssal-hill width and the spreading rate of the parent spreading center during abyssal-hill formation. The characteristic width of abyssal hills decreases from ~8 km for crust created at 2 cm/yr FSR to ~2 km for crust created at 7 cm/yr FSR. Characteristic width increases with increasing spreading rate for faster rates, from 2 km at 7 cm/yr FSR to 3 km for crust created at 16 cm/yr FSR. Goff et al. [1991] attribute this increase to the complex spreading histories typical of extremely fast spreading ridges.

The degree of abyssal hill asymmetry, defined as the difference in slope magnitude between the inward-facing (towards the spreading axis) and outward-facing sides of an abyssal hill, also correlates with spreading rate [*Kriner et al.*, 2006]. Unlike the correlations between abyssal-hill width and spreading rate and between abyssal-hill RMS amplitude and spreading rate, the correlation between abyssal-hill asymmetry and spreading rate does not change at the transition between axial-valley and axial-high morphology at ~7 cm/yr FSR.

5.2 Osbourn Trough abyssal-hill morphology

We hope to answer the following two questions by analyzing the abyssal-hill fabric observed near the Osbourn Trough:

> 1. Was there ever an east-west component of spreading on the Osbourn spreading center that can explain the east-west offset of the Manihiki and Hikurangi plateaus?

> 2. Was there a change in spreading rate prior to the extinction of the Osbourn spreading center and if so, how does that change the inferred extinction age for the Osbourn spreading center?

Our surveys are ideal for this type of analysis because they extend away from the trough for several hundred kilometers. Two surveys (those conducted during NBP0304 and NBP0207) extend northward to the Manihiki plateau, providing a record of abyssal hills generated at the Osbourn spreading center throughout its entire active period. In addition to the labeled ship tracks in Figure 1, we also analyze abyssal hill trends observed in several other multibeam surveys (dotted lines in Figure 1). These additional surveys provide continuous coverage between regions created at the Osbourn spreading center and the regions created at the Pacific-Phoenix ridge, discussed by Larson et al. [2002].

The location of changes in abyssal-hill morphology cannot be identified *a priori* so we use a technique of parameter estimation that is spatially local to define regions of

relatively constant abyssal hill properties. For abyssal hill trends a single estimate of paleo spreading direction is then made for each region.

In this paper we estimate abyssal hill statistics by the application of a ridgelet transform method to the multibeam bathymetry data (Appendix A). This method utilizes the ridgelet transform of Candès [1998] and Candès and Donoho [1999] to locally estimate abyssal-hill azimuth, width and RMS amplitude. An issue that arises in the use of abyssal fabric is the effect of erosion and sedimentation on the estimates. Fortunately, seismic data are available to allow us to quantify this effect. In Appendix A, we also discuss the effect of sedimentation on abyssal-hill parameter estimates.

Application of the ridgelet transform procedure to our multibeam data shows that the abyssal hills observed north and south of the Osbourn Trough can be divided into four groups based on azimuth trends and location (Figure 6). The first group, designated the "Manihiki" abyssal hills, consists of the abyssal hills observed between the southern side of the Manihiki Plateau and 22°S. The mean azimuth of this population is 104.7°+/-1.7° (95% confidence interval; Figure 6). The second group, the "North Osbourn" abyssal hills in Figure 6, consists of the abyssal hills observed between 22°S and the axis of the Osbourn Trough at 26°S. These abyssal hills have a mean azimuth of 92.1°+/-3.1°, and the results of a Watson-Williams test [*Zar*, 1999] show that this group has a different mean from the Manihiki abyssal hills with 95% confidence. Further subdivision of the observed azimuths into smaller populations does not yield any populations with average azimuths intermediate to those of the Manihiki and North Osbourn abyssal hills. South of the Osbourn Trough a similar pattern is observed. The "South Osbourn" abyssal hills, those observed between 30°S and the Osbourn Trough, have a mean azimuth of 94.8°+/-3.5°, similar to the mean azimuth of the North Osbourn abyssal hills. South of 30°S the fourth group, the "Hikurangi" abyssal hills have mean trend of 110.1°+/-7.3°, which likewise is similar to the azimuth of the Manihiki abyssal hills. Like the Manihiki and North Osbourn Abyssal hills, the two groups south of the Osbourn Trough also have differing means at a 95% confidence level. However, the sharpness of the transitions between the groups at 22°S and 30°S cannot be accurately determined from our data. We estimate that these locations of these transitions are accurate to approximately 1°. The

symmetric pattern of abyssal hill azimuths about the Osbourn Trough is in agreement with the spreading center origin of the Osbourn Trough. The change in abyssal-hill azimuth indicates that the spreading direction of the Osbourn paleo-spreading center changed from an azimuth of ~13.0° to ~2.8° at time when the crust near 22°S and 30°S were simultaneously being created.

Two groups of abyssal hills east of those created at the Osbourn Trough are also shown in Figure 6. These populations are those described by Larson et al. [2002] as being created at the Pacific-Phoenix spreading center during Chron C34. North of the Austral Fracture Zone (AFZ; Figure 1) we observe the "North PAC-PHO" abyssal hills, whose mean azimuth is 78.4°+/-6.5°. South of the AFZ are the "South PAC-PHO abyssal hills, which have mean azimuth 74.1°+/-3.5°. Both of these populations have means that are different from the four Osbourn abyssal hill groups as well as from each other at a 95% confidence level.

The output of the RMS amplitude and width analysis of the abyssal hills created at the Osbourn spreading center is shown in Figures 7 and 8 respectively. These two statistics are affected by sediment cover, so we restrict our analysis to the ship tracks near the western end of the Osbourn Trough where sediments are thinnest and where we have seismic data constraints on sediment thickness. The results of this analysis are shown for latitudes between 26°S and 20°S. North and south of these latitudes, thick sediments blanket the abyssal-hill fabric, casting doubt on our estimates of the abyssal-hill RMS amplitude and width (see Appendix A). Similarly, ship tracks approaching the Tonga-Kermadec subduction zone pass into terrain faulted by extension related to subduction. We have also avoided the region of anomalous bathymetry north of the 172.7°W trough offset (i.e., a "discordant zone", [*Macdonald et al.*, 1991]). In the locations presented in Figures 7 and 8 our estimates of abyssal-hill width and amplitude are believed to be representative of the basement topography created at the Osbourn spreading center. The RMS amplitude of the bathymetry decreases from 250-300 m at the trough axis near 26°S to 50 m north of 25°S (Figure 7). The RMS amplitude north of 25°S is approximately 50-60 m for all ship tracks northward until latitude 23.3°S. North of this point the RMS amplitudes begin to fluctuate about 50 m with a maximum excursion of ~110 m and a

minimum of ~25 m. The largest excursions occur in regions of increasing sediment thickness at the northern ends of NBP0207 and NBP0304 (grey curves in Figure 7).

The general trend north of 25°S is that where sediments are thin (< 80 m thick) RMS amplitudes are small, approximately 40-70 m with a few excursions to 100 m. The results of Goff et al. [1997] and Hayes and Kane [1991] allow us to estimate spreading rates for the region of our analysis. The decrease in RMS amplitude from 250 m to 50 m between 26°S and 25°S corresponds to a drop in spreading rate from > 7 cm/yr FSR at the time of formation of the crust at 25°S to 2 cm/yr FSR immediately prior to extinction of the Osbourn spreading center. The region north of 25°S where RMS amplitude is 50-70 m corresponds to formation at spreading rates > 7 cm/yr FSR. Unfortunately, as discussed above, we cannot constrain the exact spreading rate for this region as the correlation between RMS amplitude and spreading rate only holds for rates less than 7 cm/yr FSR.

The widths of abyssal hills in this region also vary (Figure 8). Between 24.5°S and 26°S widths range from 1.5 to 16 km. North of 24.5°S the smallest scales are subdued with widths generally ranging from 2-16 km. Abyssal-hill widths less than 2 km correspond to a spreading rate of ~8 cm /yr FSR [*Goff et al.*, 1997]. The smaller widths at the trough axis may be explained by increased faulting near the axis of the Osbourn spreading center during the last few million years of spreading. Increased faulting immediately prior to the extinction of the Labrador ridge was observed by Srivastava and Keen [1995].

It is difficult to use abyssal-hill widths to constrain the spreading rate of the Osbourn spreading center as we observe a wide range of scales in all regions of our survey and are unable to designate any particular width as dominant (Figure 8). Furthermore, as increasing sediment thickness obscures the finest scales first, the true range of scales may be even larger than what we observe. This wide range of observed scales is interesting in itself as it indicates that the faulting process that forms abyssal hills can create them at several scales simultaneously.

The abyssal hill analysis yields some important constraints on the tectonic history of the Osbourn spreading center. When the Hikurangi and Manihiki Plateaus rifted, the subsequent spreading that continued to separate the two plateaus took place along a 15°-20° azimuth. The east-west component of this spreading may explain the modern east-west offset of the Hikurangi and Manihiki plateaus. At some point prior to extinction the spreading direction at the Osbourn spreading center changed relatively suddenly to an azimuth of 2°-5° ~450 km from the modern trough axis. We also know that the spreading rate slowed significantly immediately prior to the extinction of the spreading center. If the last 110 km of the crust north and south of the trough was emplaced at an average full spreading rate of 4-11 cm/yr (a range that is in agreement with RMS amplitudes, gravity and morphology observed at the trough axis) then this slowing began 4-11 Ma before ridge extinction. The RMS amplitude of bathymetry also indicates that prior to this slowing the spreading rate was > 7 cm/yr FSR. In order to better constrain this spreading rate and determine the timing of the events outlined by the abyssal-hill strikes we must combine our results with other data obtained near the Osbourn region.

Two additional features of interest in the bathymetry of the Osbourn region are shown in Figures 9 and 10. The region in Figure 9, east of the Wishbone Scarp contains two long linear features (highlighted with dashed lines) that may be the bathymetric expression of fracture zones. These two features are sub-parallel to and located between the Southeast Manihiki Scarp and the triple junction trace described by Eagles et al. [2004] (Figure 1). However we are unable to determine if these features are connected to either the triple junction trace or the Southeast Manihiki Scarp due to a lack of data north and south of these lineations. Several short lines delineate a series of ridges observed southwest of the Manihiki Plateau in Figure 10. These ridges are isolated to this region and their trend parallels neither the local abyssal hill fabric nor the trend of the Southeast Manihiki Scarp. These ridges may result from the rifting event that first separated the Manihiki and Hikurangi plateaus as they are approximately parallel to the trend of the southwest margin of the Manihiki Plateau.

6. Tectonic model

6.1 Geometry of Osbourn spreading

Abyssal-hill strikes provide constraints on the geometry of spreading at the Osbourn spreading center. Spreading initially occurred at an azimuth of approximately 15°-20°, based on the trends of the Hikurangi and Manihiki abyssal hills, but later rotated to a 2°-5° azimuth as indicated by the near east-west strike of the abyssal hills that flank the Osbourn Trough. Based on these constraints we have formulated a geometrical model of spreading at the Osbourn paleo spreading center (Figure 11).

Figure 11a shows the initial configuration of the Manihiki and Hikurangi Plateaus immediately prior to their separation. This configuration matches that proposed by Taylor [2006] and predates to the opening of the Ellice basin to the west (Figure 1). The configuration in Figure 11b is that corresponds to 1200 km of separation of the Hikurangi and Manihiki plateaus. The east-west component of spreading explains the east-west offset of the plateaus described by Eagles et al. [2004]. This spreading direction also closely parallels the 14° trend of the Southeast Manihiki Scarp. The Southeast Manihiki scarp also appears to be the location of the boundary between the Northern PAC-PHO and Manihiki abyssal hills. In agreement with the results presented by Larson et al. [2002], our measurements of the trend of PAC-PHO abyssal hills indicate that the spreading southeast of the Manihiki Plateau occurred along an azimuth of 168° and later rotated to 164° as the PAC-PHO ridge migrated southward. The different spreading directions observed southeast and southwest of the Manihiki Plateau imply that these regions were created at different plate boundaries, and therefore there were at least three plates separated by these boundaries. These three plates consisted of the plate containing the Manihiki Plateau which, following Larson et al. we call the Pacific Plate (although which plate should be considered the ancestor of the modern Pacific plate at this time is debatable, as both the plates that contained the Hikurangi and Ontong Java plateaus during the Early Cretaceous now make up portions of the modern Pacific Plate), the Hikurangi plate, south of the Osbourn paleo spreading center and the Phoenix plate, south of the Cretaceous Pacific -Phoenix ridge. The boundary between the Hikurangi plates

and the Phoenix plates appears to have been at the location of the Southeast Manihiki Scarp, although the exact configuration of this triple junction between the three plates cannot be determined from our data. In Figure 10b we also show the location of the Western Wishbone Scarp as conjugate to the Southeast Manihiki Scarp and therefore it may also be a remnant of the Hikurangi-Phoenix plate boundary. This configuration is an agreement with the fracture zone origin of the West Manihiki Scarp presented by Mortimer et al. [2006]. Determining the exact role of the two ridges, and the nature of the boundaries between them, requires more detailed marine geophysical surveys of the West Wishbone Scarp, and Southeast Manihiki Scarp and surrounding areas.

After a total of ~2400 km of spreading between the Plateaus, the spreading direction changed to 2°-5° relative to the Manihiki Plateau.   Following this rotation another ~900 km of crust was accreted at the Osbourn ridge before the spreading rate of the ridge slowed. The configuration of the Osbourn region immediately prior to this slowing event is shown in Figure 11c. At no location are the abyssal hills created at the Osbourn spreading center parallel to those created at the Pacific-Phoenix ridge. Thus it appears that the Hikurangi plate remained separated from the Phoenix plate throughout its entire lifetime.   The fracture zones observed in Figure 9 may mark the location of the easternmost extent of the Hikurangi Plate at the time of Figure 11c.

We propose, following Lonsdale [1997] that the slowing event, and eventual extinction of the Osbourn Trough was caused by the entrance of the Hikurangi plateau into a subduction zone that under-thrust the Gondwana section of the Antarctic Plate.

Figure 11d shows the configuration of the spreading center and subduction zone at the time of extinction of the Osbourn Trough, overlain on their modern locations on the Pacific Plate. After the capture of the Hikurangi plate by the Pacific plate, the relative motion between the Pacific plate and Gondwana was divergent, the captured piece thus began to move northward away from Gondwana. This motion was accommodated by extension in the Zealandia sector of Gondwana as outlined by Luyendyk [1995]. Extension continued until ~85 Ma when the Campbell Plateau and Chatham Rise rifted away from Antarctica at the modern Pacific-Antarctic ridge.

It may have been possible that as the Osbourn spreading center died, the eastern arm of the Wishbone Scarp began forming. As the Hikurangi plateau entered the subduction zone it stalled subduction at this location causing the drastic reduction in spreading rate at the western part of the Osbourn ridge. A piece of the eastern part of the Hikurangi plate may have continued to move southward into the subduction zone, eventually becoming the Charcot plate of Eagles et al. [2004]. In such a scenario, the eastern arm of the Wishbone Scarp would have been the location of a strike slip boundary between the Charcot Plate and the (now captured) Hikurangi portion of the Pacific Plate. However, as there is little data in the region surrounding the Wishbone scarp, such a model remains speculative, and is omitted from Figure 11.

6.2 Timing of Osbourn spreading

Despite their strong geometrical constraints on Osbourn spreading, our data provide little temporal constraint on the events of Figure 11. The magnetic anomaly profiles of Figure 3 imply that the extinction of the Osbourn Spreading Center occurred sometime during Chron C34. Abyssal-hill statistics show that spreading at the Osbourn spreading center slowed significantly 4-11 Ma prior to extinction. This slowing event is expressed as a change in the average abyssal-hill amplitude near 25°S north of the Osbourn Trough (Figure 2b). Sediment thickness in the region of Figure 2 is constant at about 60-70 m, so the increased smoothness north of 25°S cannot result from increased sedimentation. We estimate a spreading rate of 4-11 cm/yr FSR after the slowing event and > 7 cm/yr FSR prior to slowing, based upon abyssal hill amplitudes; however, the exact rate before slowing cannot be determined.

We must therefore rely on other data to constrain the timing of these events. One such constraint is provided by the age of the crust at DSDP site 595. Preliminary work estimated a 100 Ma minimum age of the crust at this site [*Menard et al.*, 1987]. Sutherland and Hollis [2001] however estimate the crust at this site to be 132-144 Ma based upon biostratigraphy of cored sediments. Previous models of the Osbourn spreading center have assumed that rifting between the Hikurangi and Manihiki plateaus began shortly after their formation around 119-121 Ma. However Mortimer et al. [2006]

show that this rifting only needs to have occurred before the formation of the West Wishbone Scarp at ca. 115 Ma.

The age estimate of Sutherland and Hollis [2001] implies that the crust at DSDP site 595 formed prior to the eruption of the Hikurangi and Manihiki Plateaus, an assertion that is difficult to explain if this crust was indeed formed at the Osbourn Trough. However, our data do not directly contradict the model of Sutherland and Hollis [2001]. The one ship track that we do have at the Longitude of DSDP site 595 shows no evidence of the fracture zone implied by Sutherland and Hollis [2001], however data in this region is too sparse to eliminate its presence entirely. In the context of their model, the scenario presented in Figure 11 describes the late evolution of the Pacific-Moa plate boundary. Another explanation for the anomalous ages determined by Sutherland and Hollis [2001] is that deep sea currents transported older sediments to the location of DSDP site 595.

7. Conclusions

Our data analysis yields several important clues to explaining the tectonic history of the Osbourn Trough. Analysis of the magnetic data shows that the Osbourn paleo-spreading center stopped spreading during Chron C34. The most fruitful part of our analysis is the examination of the seafloor fabric away from the trough axis. A change in seafloor RMS amplitude fabric shows that spreading slowed 4-11 Ma prior to the extinction of the Osbourn Trough. Change in abyssal-hill strike also shows that spreading direction changed from NNE-SSW to approximately N-S (measured in a modern Manihiki Plateau reference frame) some time prior to the slowing event. Using our results, we formulated a new model of the Osbourn Trough's tectonic history.

Our model successfully explains the conflict between Osbourn paleo-spreading models and regional models by showing that spreading on the Osbourn spreading center was decoupled from that of the Pacific-Phoenix ridge, and by showing that the Osbourn spreading center spread at a rate faster than predicted by its axial characteristics. Correspondingly, our model predicts that the Osbourn spreading center ceased spreading prior to previous estimates. A rifting age of 115 Ma for the Hikurangi and Manihiki

Plateaus predicts spreading ceased prior to 87 Ma, while a 121 Ma extinction age implies that spreading stopped before 93 Ma.

One aspect of our tectonic model warranting further study is the interaction of the western end of the Pacific-Phoenix ridge with the Ellice basin spreading center postulated to be active at this time [*Taylor*, 2006]. The presence of the Ellice ridge implies that there must be a triple junction trace somewhere southwest of the Manihiki plateau, although no such feature has been identified. As this region is heavily sedimented and has been subject to much intra-plate volcanism further marine geophysical surveys are required to elucidate the details of formation of this area. The Wishbone Scarp is also sparsely surveyed, and more data are required to elucidate the origin of this anomalous feature. Another aspect warranting further investigation is the extent of the fracture zones of Figure 9 and whether they are contiguous with either the southeast Manihiki scarp or the Charcot-Phoenix-Pacific triple junction trace described by Eagles et al. [2004].

Appendix A: The effect of sedimentation on spreading rates and direction estimates from Abyssal-Hill fabric

Our seismic data provide a means to quantify the effects of sedimentation on abyssal-hill statistics. The NBP0207 seismic line runs north-south perpendicular to the trend of the abyssal-hill fabric. The two-dimensional nature of the seafloor morphology perpendicular to the seismic line implies that the observed seismic bathymetry and basement depth are a good approximation to the average bathymetry and basement topography along an azimuth of 90° (i.e., the bathymetry and basement topography along the seismic line is expected to be similar in shape to the Radon transform of the 2D bathymetry and basement topography at $\theta=90°$). The unusual fabric near the NBP0304b seismic lines precludes their use in this analysis as the bathymetry along the seismic line is not representative of the bathymetry across the NBP0304b multibeam swath.

By comparing the RMS amplitude and scales of the seismically determined bathymetry and basement topography profiles, we are able to determine the effect of sedimentation on these quantities. Figure A1a[1] shows the bathymetry and basement topography interpreted from the NBP0207 seismic data. Figure A1b shows the sediment thickness observed along this line after the application of a mean filter of 5 km half-width. Part c) of Figure A1 displays the ratio of the bathymetry RMS amplitude to the basement RMS amplitude, each of which have been calculated using a 20 km moving window. The rough negative correlation between this ratio and the sediment depth in b) indicates that thicker sediments reduce the RMS amplitude of the bathymetry relative to that of the basement more effectively than do thinner sediments. Furthermore where sediment thickness is less than 75-100 m, the ratio in Figure A1c is very near to 1, indicating that a sediment cover of this thickness does not significantly reduce the RMS amplitude of the bathymetry relative to the RMS amplitude of the basement. Similar results have been reported by Goff [1991] and Goff et al. [1995; 1997] and are predicted by the sedimentation model of Webb and Jordan [1993].

---

[1] Available as an online supplement at www.agu.org/pubs/crossref/2007/2006JB004550.shtml

Figures A1d –A1f demonstrate the effects of sedimentation on scale. Parts d and e are the wavelet transforms of the basement topography and bathymetry respectively. Part f is the difference between parts d and e. The two wavelet transforms are very similar in shape, but their amplitudes differ for widths less than 8 km (Figure A1f). Thus the effect of sedimentation is to preferentially reduce the features of small scale. We do not observe a correlation between the range of scales affected and the sediment thickness. Such a correlation has been observed by Goff [1991] and Goff et al. [1997; 1995], where sediments progressively dampen larger scales with increasing sediment thickness.

In order to accurately interpret the results of our multibeam analysis it is important to know the sediment depth near our survey locations. Where sediments are relatively thin (< 70-100 m) we can be confident that our RMS amplitude is an accurate estimate of the RMS amplitude of basement. Our scale measurements will be affected by sedimentation regardless of sediment depth. Where possible we can use our seismically-determined sediment thickness. Elsewhere we must rely on the NGDC global sediment thickness database [*Divins*, 2006]. Sedimentation, however, should have no effect on abyssal-hill azimuths because sedimentation acts to change abyssal-hill widths and amplitudes only.

References

Billen, M., and J. Stock (2000), Morphology and origin of the Osbourn Trough, *Journal of Geophysical Research*, *105*, 13481-13489.

Bowers, N. et al. (2001), Fluctuations of the paleomagnetic field during Chron C5 as recorded in near-bottom marine magnetic anomaly data, *Journal of Geophysical Research*, *106*, 26379-26396.

Buck, W., and A. Polikov (1998), Abyssal hills formed by stretching oceanic lithosphere, *Nature*, *392*, 272-275.

Burns, R. et al. (1973), *Initial Reports, DSDP, 21*, U.S. Govt. Printing Office, Washington.

Cande, S., and D. Kent (1995), Revised calibration of the geomagnetic polarity time scale for the late Cretaceous and Cenozoic, *Journal of Geophysical Research*, *100*, 6093-6095.

Candes, E. (1998), Ridgelets: Theory and application, Ph.D. thesis, pp. 116, Stanford University, Stanford.

Candes, E., and D. Donoho (1999), Ridgelets: a key to higher dimensional intermittency, *Philosophical Transactions of the Royal Society of London*, *357*, 2495.

Divins, D. L. (2006), NGDC Total sediment thickness of the world's oceans & marginal seas, http://www.ngdc.noaa.gov/mgg/sedthick/sedthick.html, *National Geophysics Data Center, Boulder CO*.

Eagles, G. et al. (2004), High-resolution animated tectonic reconstruction of the South Pacific and West Antarctic Margin, *Geochemistry Geophysics Geosystems*, *5*, Q07002,doi:07010.01029/02003GC000657.

Elthon, D. et al. (1982), Mineral chemistry of ultramafic cumulates from the North Arm Mountain massif of the Bay of Islands ophiolite: Evidence for high-pressure crystal fractionation of oceanic basalts, *Journal of Geophysical Research*, *87*, 8717-8734.

Goff, J. (1991), A global and regional stochastic analysis of near-ridge abyssal hill morphology, *Journal of Geophysical Research*, *96*, 21713-21737.

Goff, J., and T. H. Jordan (1988), Stochastic modeling of seafloor morphology: Inversion of Sea Beam data for second-order statistics, *Journal of Geophysical Research*, *93*, 13589-13608.

Goff, J. et al. (1997), Stochastic analysis of seafloor morphology on the flank of the Southeast Indian Ridge: The influence of ridge morphology on the formation of abyssal hills, *Journal of Geophysical Research*, *102*, 15521-15534.

Goff, J., and B. Tucholke (1997), Multiscale spectral analysis of bathymetry on the flank of the Mid-Atlantic Ridge: Modification of the seafloor by mass wasting and sedimentation, *Journal of Geophysical Research*, *102*, 15447-15462.

Goff, J. et al. (1995), Quantitative analysis of abyssal hills in the Atlantic Ocean: A correlation between inferred crustal thickness and extensional faulting, *Journal of Geophysical Research*, *100*, 22509-22522.

Hayes, D., and K. Kane (1991), The dependence of seafloor roughness on spreading rate, *Geophysical Research Letters*, *18*, 1425-1428.

Hoernle, K. et al. (2004), New insights into the origin and evolution of the Hikurangi oceanic plateau, *EOS, Transactions of the American Geophysical Union*, *85*, 401.

Jonas, J. et al. (1991), Gravity anomalies over spreading centers: A test of gravity models of active centers, *Journal of Geophysical Research*, *96*, 11759-11777.

Jung, W., and P. Vogt (1997), A gravity and magnetic anomaly study of the extinct Aegir Ridge, Norwegian Sea, *Journal of Geophysical Research*, *102*, 5065-5089.

Kriner, K. et al. (2006), Bathymetric gradients of lineated abyssal hills: Inferring seafloor spreading vectors and a new model for hills formed at ultra-fast rates, *Earth and Planetary Science Letters*, *242*, 98-110.

Larson, R. et al. (2002), Mid-Cretaceous tectonic evolution of the Tongareva triple junction in the southwest Pacific Basin, *Geology*, *30*, 67-70.

Larter, R. et al. (2002), Tectonic evolution of the Pacific margin of Antarctica 1. Late Cretaceous tectonic reconstructions, *Journal of Geophysical Research*, *107*, 2345.

Lonsdale, P. (1997), An incomplete geologic history of the south-west Pacific basin, *Geological Society of America Abstract Programs*, *29*, 4574.

Luyendyk, B. (1995), Hypothesis for Cretaceous rifting of east Gondwana caused by subducted slab capture, *Geology*, *23*, 373-376.

Macdonald, K. et al. (1996), Volcanic growth faults and the origin of Pacific abyssal hills, *Nature*, *380*, 125-129.

Macdonald, K. et al. (1991), Mid-ocean ridges: Discontinuities, segments and giant cracks, *Science*, *253*, 986-994.

Menard, H. W. (1967), Sea floor spreading, topography and the second layer, *Science*, *157*, 923-924.

Menard, H. W. et al. (1987), *Initial Reports, DSDP, 91*, U. S. Govt. Printing Office, Washington.

Mortimer, N. et al. (2006), New constraints on the age and evolution of the Wishbone Ridge, southwest Pacific Cretaceous microplates, and Zealandia-West Antarctica breakup, *Geology*, *34*, 185-188.

Mortimer, N., and D. Parkinson (1996), Hikurangi Plateau: A Cretaceous large igneous province in the southwest Pacific Ocean, *Journal of Geophysical Research*, *101*, 687-696.

Muller, R. et al. (2005), Crustal structure and rift flank uplift of the Adare Trough, Antarctica, *Geochemistry Geophysics Geosystems*, *6*.

Nettleton, L. (1939), Determination of density for reduction of gravimeter observations, *Geophysics*, *4*, 176-183.

Osler, J., and K. Louden (1992), Crustal structure of an extinct rift axis in the Labrador Sea: preliminary results from a seismic refraction survey, *Earth and Planetary Science Letters*, *108*, 243-258.

Parker, R. (1972), The rapid calculation of potential anomalies, *Geophysical Journal of the Royal Astronomical Society*, *31*, 447-455.

Sandwell, D. T., and W. H. F. Smith (1997), Marine gravity anomaly from Geosat and ERS-1 satellite altimetry, *Journal of Geophysical Research*, *102*, 10039-10054.

Small, C. (1994), A global analysis of mid-ocean ridge axial topography, *Geophysical Journal International*, *116*, 64-84.

Small, C., and D. Abbott (1998), Subduction obstruction and the crack-up of the Pacific Plate, *Geology*, *26*, 795-798.

Smith, W. H. F., and D. T. Sandwell (1997), Global sea floor topography from satellite altimetry and ship depth soundings, *Science*, *277*, 1956-1962.

Srivastava, S., and C. Keen (1995), A deep seismic reflection profile across the extinct Mid-Labrador Sea spreading center, *Tectonics*, *14*, 372-389.

Sutherland, R., and C. Hollis (2001), Cretaceous demise of the Moa plate and strike-slip motion at the Gondwana margin, *Geology*, *29*, 279-282.

Taylor, B. (2006), The single largest oceanic plateau: Ontong Java-Manihiki-Hikurangi, *Earth and Planetary Science Letters*, *241*, 372-380.

Uenzelmann-Neben, G. et al. (1992), The Aegir Ridge: Structure of an extinct spreading axis, *Journal of Geophysical Research*, *97*, 9203-9218.

Watts, A. (1982), Gravity Anomalies over oceanic rifts, in *Continental and Oceanic Rifts, Geodynamics series 8*, edited by G. Palmeson, pp. 99-105, American Geophysical Union, Washington.

Watts, A. (2001), *Isostasy and Flexure of the Lithosphere*, pp. 458, Cambridge University Press, Cambridge, U.K.

Webb, H., and T. H. Jordan (1993), Quantifying the distribution and transport of pelagic sediments on young abyssal hills, *Geophysical Research Letters*, *20*, 2203-2206.

Zar, J. (1999), *Biostatistical Analysis*, Prentice Hall, Upper Saddle River, New Jersey.

Tables:

Table 1: Densities of gravity model elements

	R^2	$\rho_{sediment}$ (g/cm^3)	ρ_{crust} (g/cm^3)	ρ_{mantle} (g/cm^3)	ρ_{body} (g/cm^3)
Model 1 (Magma Chamber)	0.88	1.61 +/- 0.20	2.48 +/- 0.04	3.26 +/- 0.06	2.04 +/- 0.04
Model 2 (Serpentinization)	0.87	1.67 +/- 0.21	2.52 +/- 0.04	3.32 +/- 0.06	2.36 +/- 0.04
Model 3 (Crustal Root)	0.88	1.77 +/- 0.13	2.47 +/- 0.13	3.28 +/- 0.05	-

Figure 1: Bathymetric map [*Smith and Sandwell*, 1997] of the Southeast Pacific Basin near the Osbourn region. The locations of the tectonic features discussed in the text are labeled. The location of this Figure is shown on the inset globe. The Pacific-Phoenix-Farallon triple junction trace (PAC-PHO-FAR) is plotted as a thick dashed line. The Chatham rise paleo-subduction zone is plotted as a line with triangular teeth. The direction of these teeth indicates the direction of paleo-subduction. The Osbourn Trough appears as an east-striking bathymetric low near 26°S, the eastern end of which terminates at the intersection with the northern end of the Wishbone Scarp near 165°W. The cruises discussed in the gravity and magnetic data sections are labeled. In addition to these, the sections of multibeam data from several additional cruises analyzed in section 5 are shown as thin dotted lines. The survey geometry provides us the opportunity to study crust created throughout the entire spreading history of the Osbourn spreading center. The locations of Deep Sea Drilling Program sites 205 and 595 are shown as a star and a dot respectively. At the southern end of the figure the locations of anomalies 34y and 33y on either side of a gravity lineation east of the Wishbone Scarp are plotted as taken from Larter et al. [2002]. The differing distance between these anomalies on either side of this lineation demonstrate that it is the location of a paleo plate boundary. The three white boxes labeled 2, 8 and 9 delineate the locations of Figures 2, 8 and 9 respectively.
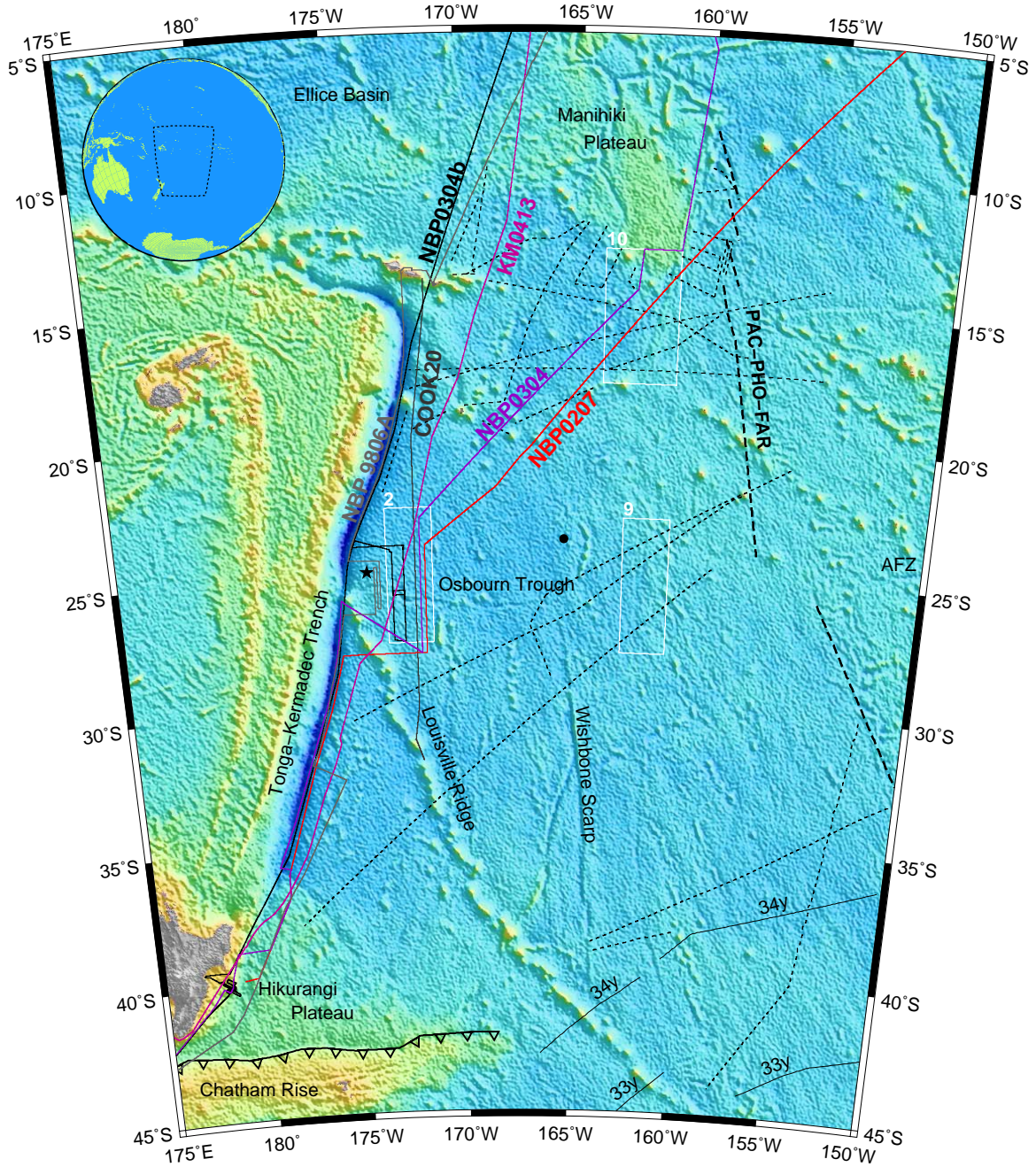
Figure 2: **a)** Multibeam data collected near the Osbourn Trough during our cruises, superimposed upon predicted bathymetry from satellite altimetry [*Smith and Sandwell*, 1997]. The locations of the NBP0207 SCS and NBP304b MCS surveys are shown by the locations of the red and black dashed lines respectively. The white box outlines the location of b). **b)** Close-up of a) highlighting the change in abyssal-hill character that occurs between 24°S and 25°S. The abyssal-hill fabric north of 24.5°S is much smoother than the fabric south of 24.5°S. This change in texture is not accompanied by a change in sediment thickness, so the subdued fabric to the north cannot result from sediment smoothing.

a)

NBP0207

NBP0304b

b)
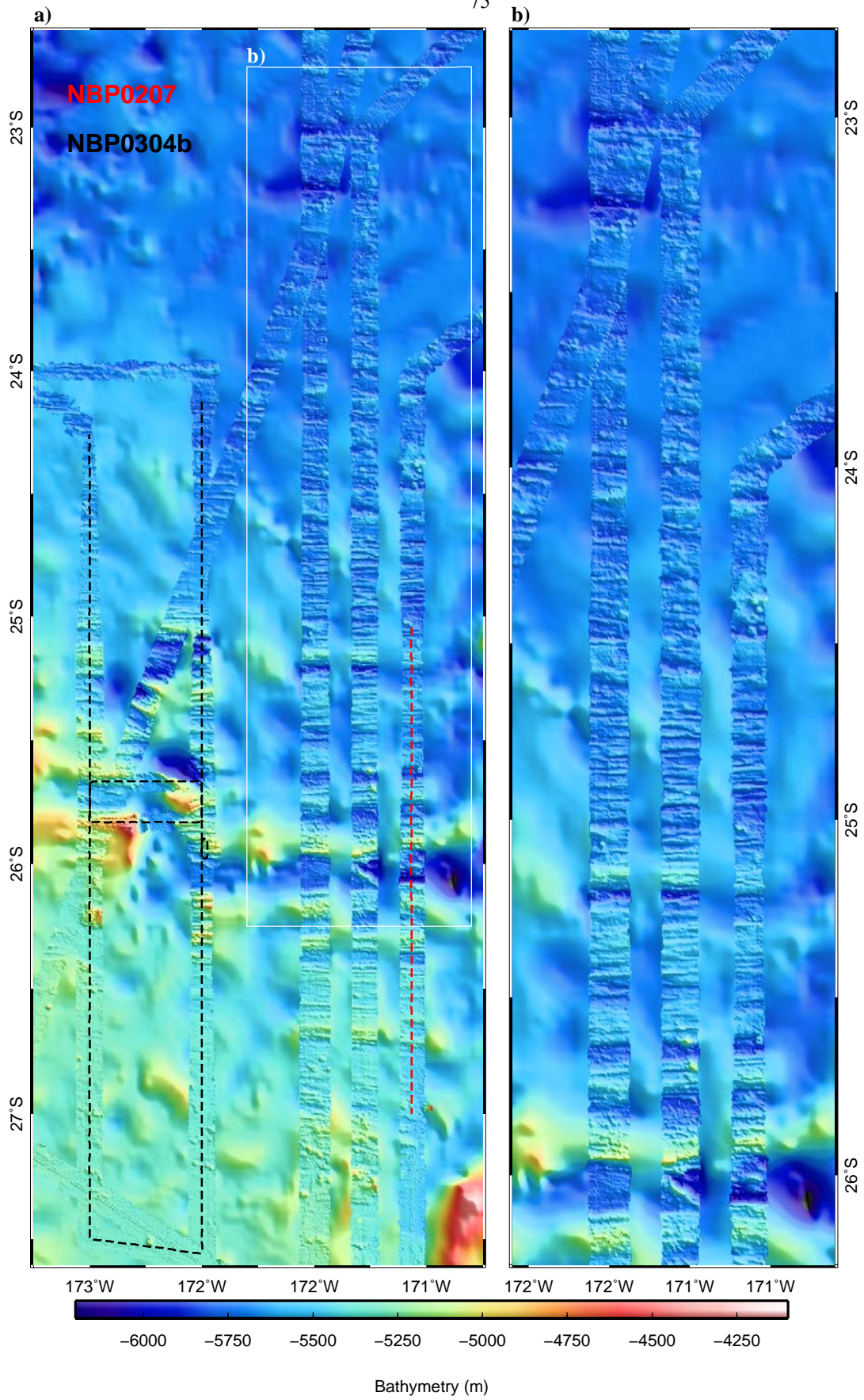
Figure 3: a) Magnetic anomaly data observed at the Osbourn Trough. The magnetic profiles have been aligned along the axis of the Osbourn Trough (the trough axis coincides with the central solid vertical gridline). Included in this Figure are our data along with that of a previous survey, NBP9806 [*Billen and Stock*, 2000]. The lack of correlation across the survey area indicates that the magnetic anomalies cannot result from magnetic field reversal. **b)** Magnetic anomaly data in a) after application of a reduction to the pole filter (skewness=60°). The symmetry of the phase-shifted profiles shows that these anomalies may result fluctuations in the magnetic field strength during Chron C34. Similar fluctuations have been observed to occur during Chron C5 [*Bowers et al.*, 2001].

a)

b)

Distance North of Trough Axis (km)
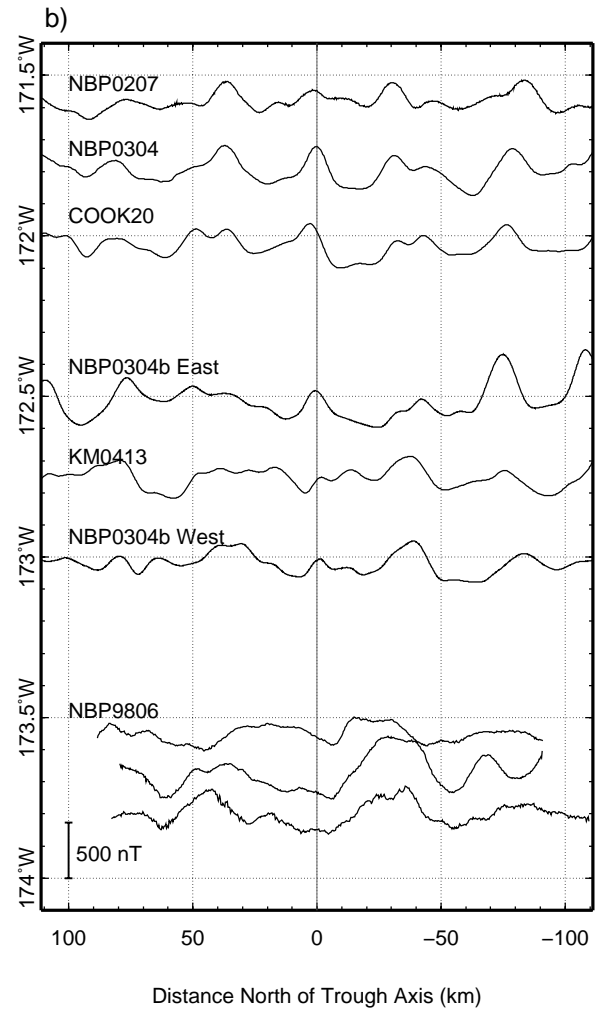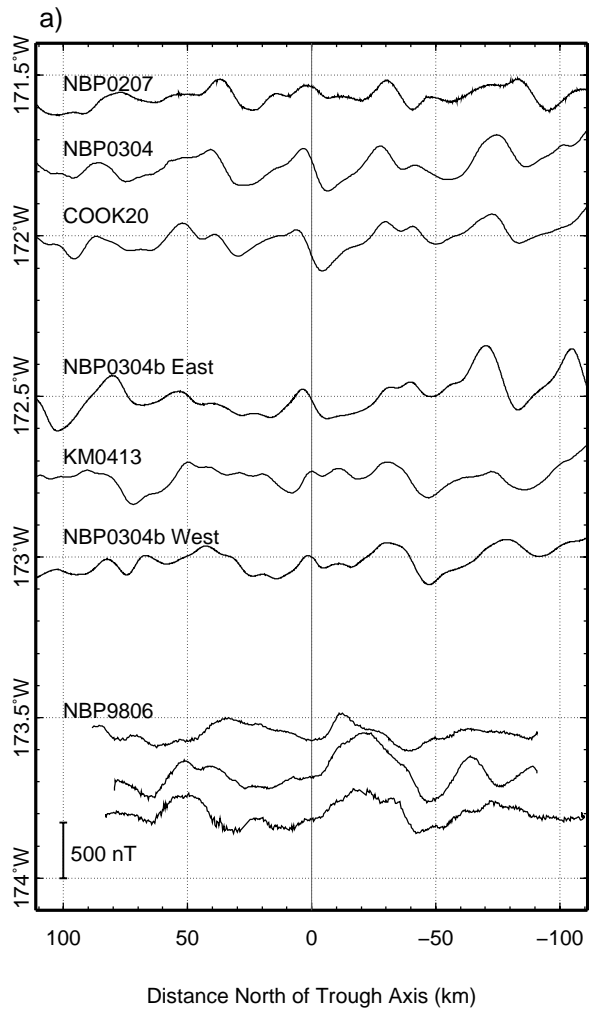
Figure 4: Gravity data observed near the Osbourn Trough after the removal of regional values. Our ship track data are shown as solid lines. The dashed lines are north-south profiles taken from a global gravity dataset [*Sandwell and Smith*, 1997]. The straight dotted lines show the zero value for each profile. The solid gray line follows the Osbourn Trough axis. The Osbourn Trough coincides with the gravity lows at 26°S and 25.2°S, east and west of 172.7°W, respectively.

NBP0207

NBP0304

COOK20

20 mGal

NBP0304b East

NBP0304b West

171.5˚W
171.75˚W
172˚W
172.25˚W
172.5˚W
172.75˚W
173˚W

25˚S   25.5˚S   26˚S   26.5˚S   27˚S
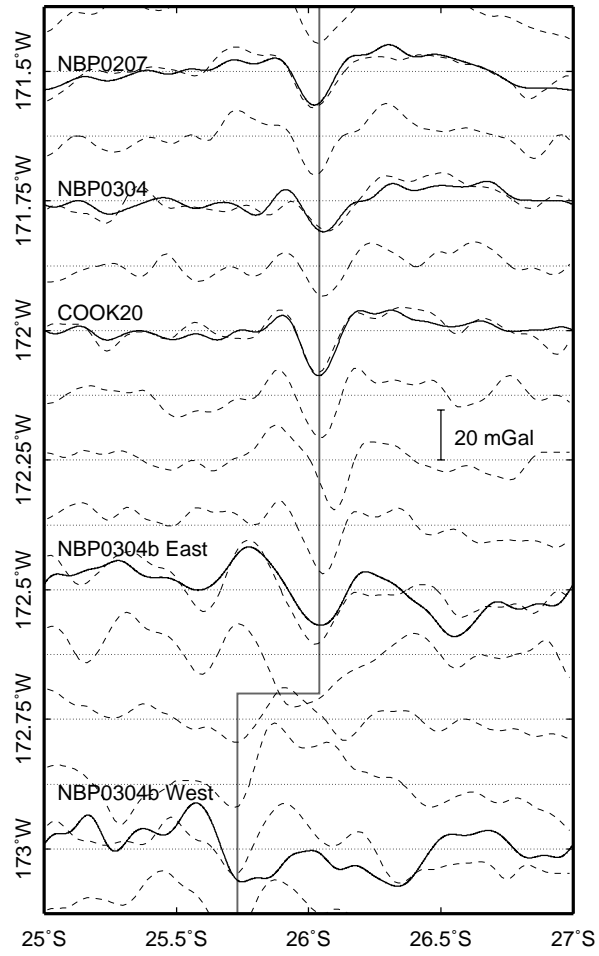
Figure 5: Models of the density structure of the Osbourn Trough that accurately predict the observed data. **a)** A single low-density region beneath the trough axis. **b)** A serpentinization model where the crust density has been modified by hydrothermal alteration. **c)** The Moho topography model of Jonas et al. [1991] Densities for each of these models that provide the best fit to the data are given in Table 1. The output of each of these models (upper panel) fits the data equally well.
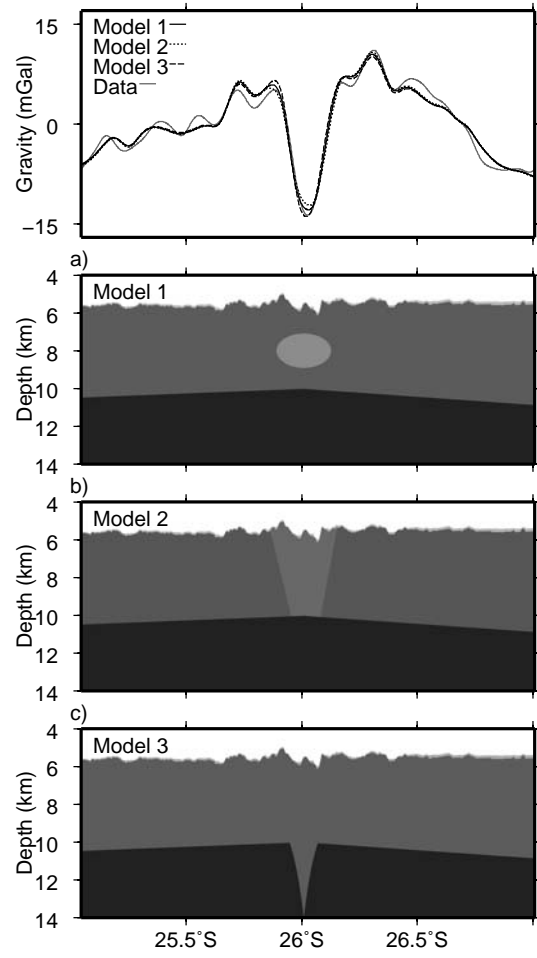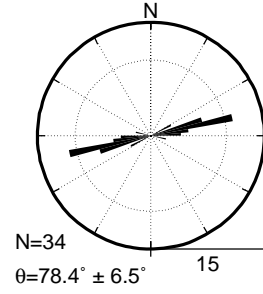
Figure 6: Abyssal hill azimuths as determined via ridgelet transform. The azimuth estimates have been split into six populations, the Manihiki, North Osbourn, South Osbourn and Hikurangi abyssal hills, all of which were created at the Osbourn spreading center and the North and South Pacific-Phoenix abyssal hills. Note that in the left panel, azimuth estimates falling outside the range of azimuths shown are plotted on the left and right boundaries at appropriate latitude. A rose diagram of each population is shown. The size of each population is presented along with the mean azimuth and 95% confidence interval. The difference between the strikes of the Manihiki/Hikurangi populations and the Osbourn abyssal hill populations indicates a change of spreading direction at the Osbourn spreading center. Furthermore the difference between the Osbourn and Pacific-Phoenix abyssal hills indicates that the Osbourn spreading center was not a section of the Cretaceous Pacific-Phoenix ridge.
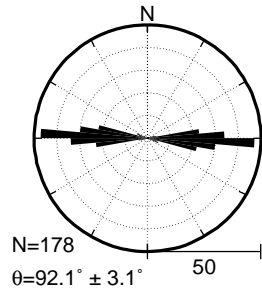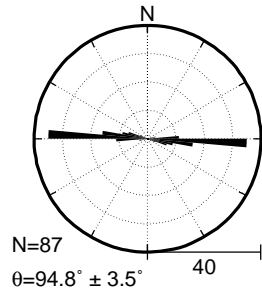
Manihiki Abyssal Hills
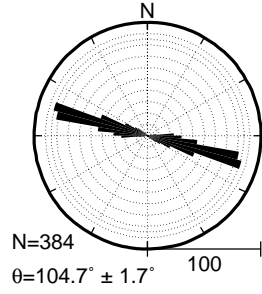
N

N=384
θ=104.7° ± 1.7°   100
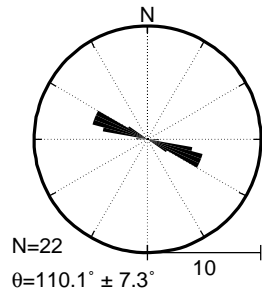
North PAC–PHO Abyssal Hills

N

N=34
θ=78.4° ± 6.5°   15

North Osbourn Abyssal Hills

N

N=178
θ=92.1° ± 3.1°   50

South Osbourn Abyssal Hills

N

N=87
θ=94.8° ± 3.5°   40

Hikurangi Abyssal Hills

N

N=22
θ=110.1° ± 7.3°   10

South PAC–PHO Abyssal Hills

N

N=152
θ=74.1° ± 3.5°   50

170°W   160°W   150°W
10°S   10°S

20°S   20°S

30°S   30°S

40°S   40°S
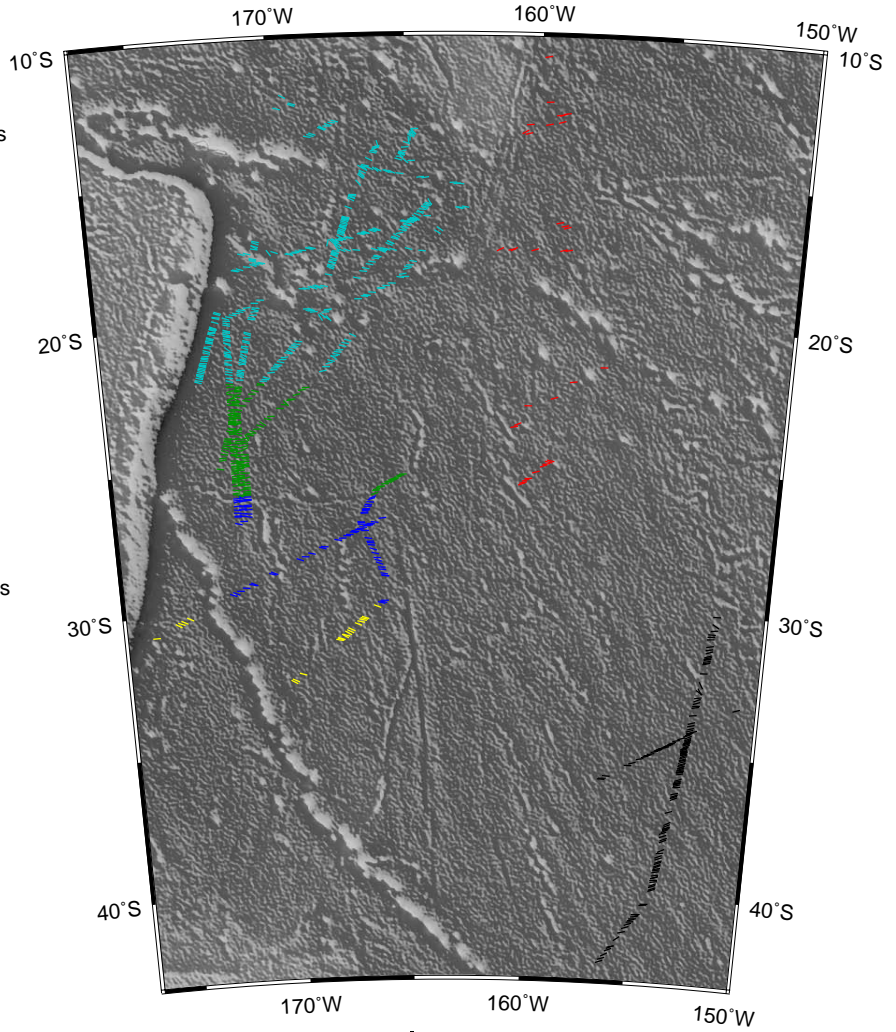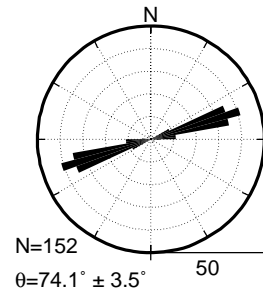170°W   160°W   150°W

Figure 7: Abyssal hill RMS amplitude for regions not contaminated by seamounts or deep sediments. The solid gray lines show sediment depth along each ship track taken from the NGDC global sediment database. The solid black lines are the RMS amplitude of bathymetry calculated along the profiles. RMS amplitude increases greatly south of 25°S. North of this latitude it remains relatively stable at 50-60 m, with some fluctuations occurring as sediments get thicker. The gray dashed line in the NBP0207 panel denotes the sediment thickness interpreted from the NBP0207 SCS data. The agreement between this thickness estimate and the NGDC database is closest northward, away from the Osbourn Trough. The KM0413 data are presented north of 25°S, as south of this latitude KM0413 passes into the "discordant zone" associated with an offset in the Osbourn Trough. The results are also similar with very smooth bathymetry being observed northward to 20°S. The gray dashed line in the KM0413 panel is the sediment thickness at the northern end of the eastern NBP0304b MCS line (see Figure 2 for location).
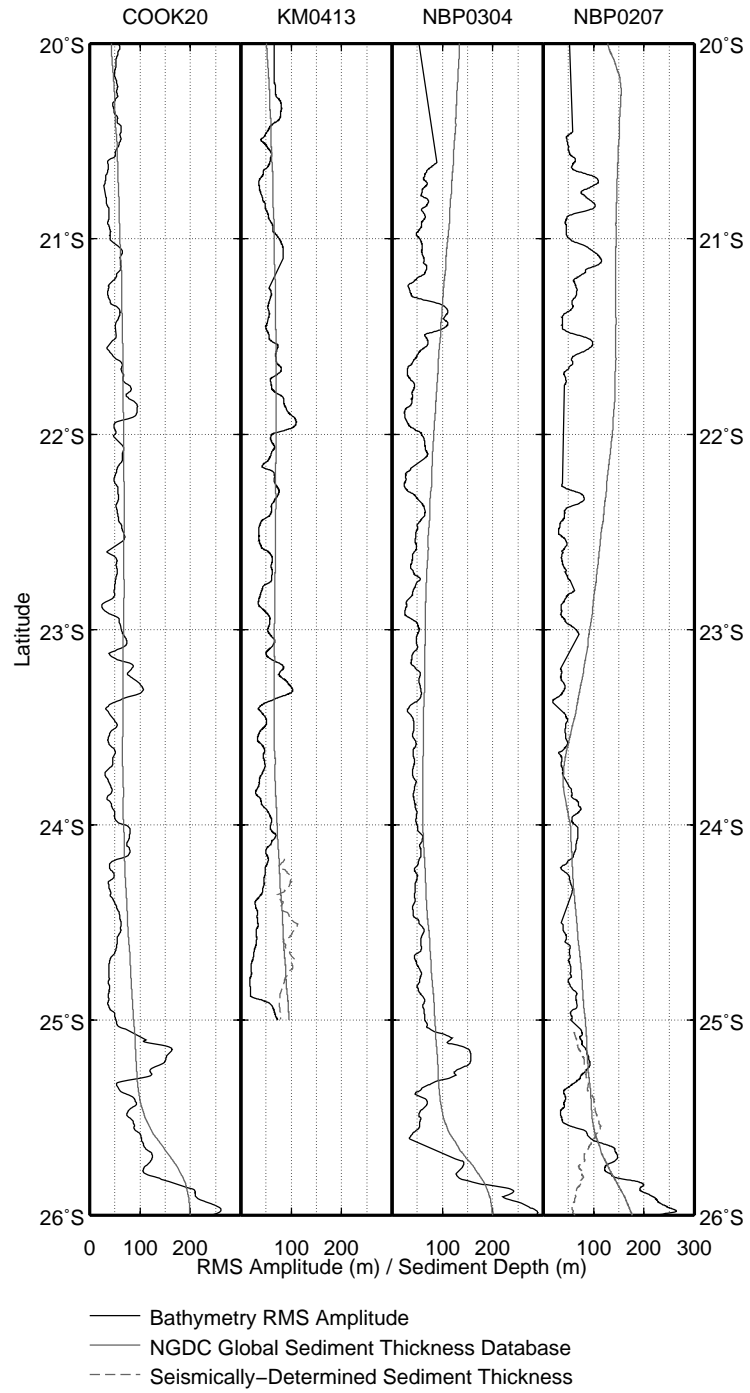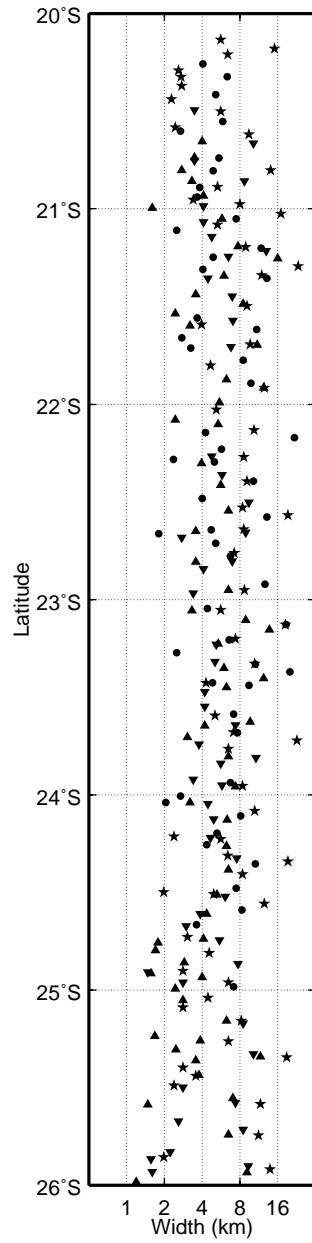
| COOK20 | KM0413 | NBP0304 | NBP0207 |

RMS Amplitude (m) / Sediment Depth (m)

Latitude

—— Bathymetry RMS Amplitude
—— NGDC Global Sediment Thickness Database
---- Seismically−Determined Sediment Thickness

Figure 8: Widths of abyssal hills as determined via ridgelet transform. All cruises display similar behavior, with no particular scale being dominant for any latitude band. There is an increase in small-width abyssal hills near the Osbourn Trough axis at 26°S. These small scales may result from increased faulting near the axis. This figure demonstrates that the process that creates abyssal hills at trough axes does so at a variety of scales simultaneously.

Figure 9: Detail of a region east of the Osbourn Trough showing the presence of two bathymetric lineations (marked by dashed lines) that may mark the locations of fracture zones. These features may be continuous with either the Southeast Manihiki Scarp or the Pacific-Phoenix-Charcot triple junction trace (Figure 1). These features may mark the most easterly extent of the Hikurangi plate during Chron C34.
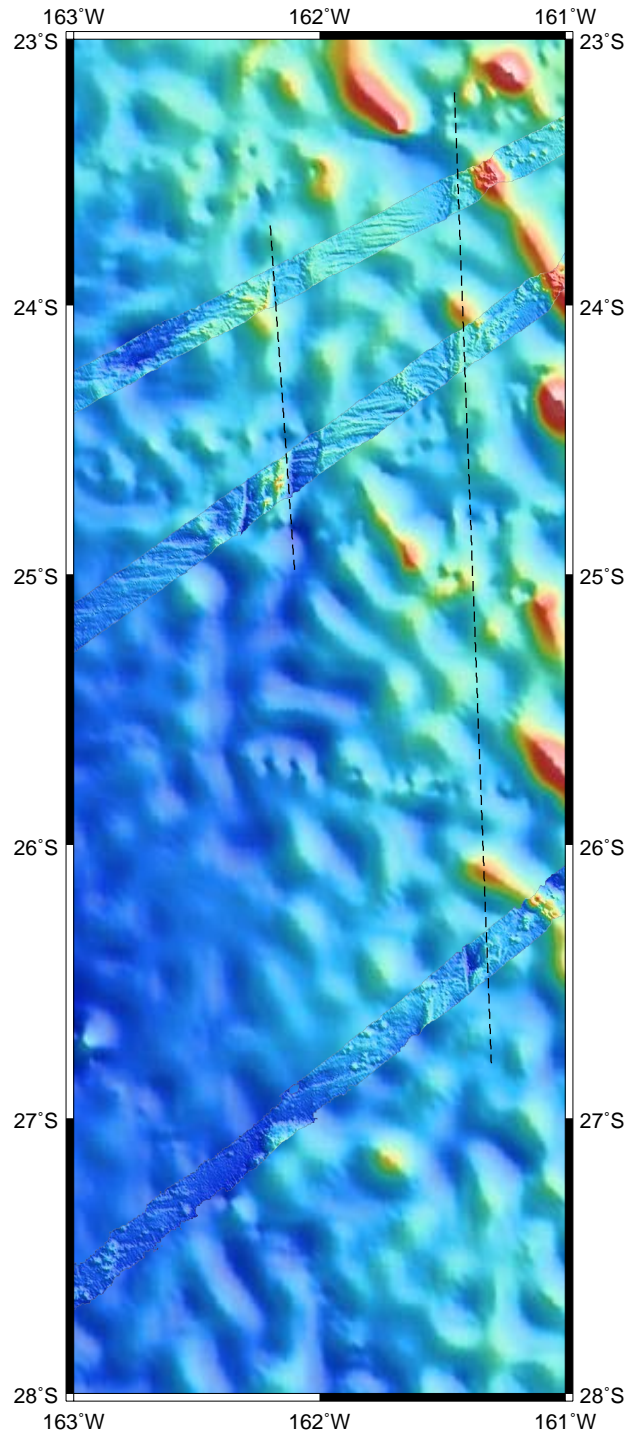
Figure 10: Detail of the southern Manihiki Plateau and Southeast Manihiki Scarp. The short black dashed lines mark the locations of several anomalous ridges that parallel neither the local abyssal hill fabric nor the trend of the Scarp. These features are isolated to this region and as they are sub-parallel to the southwest side of the Manihiki Plateau may have resulted from the rifting that initially separated the Hikurangi and Manihiki Plateaus.
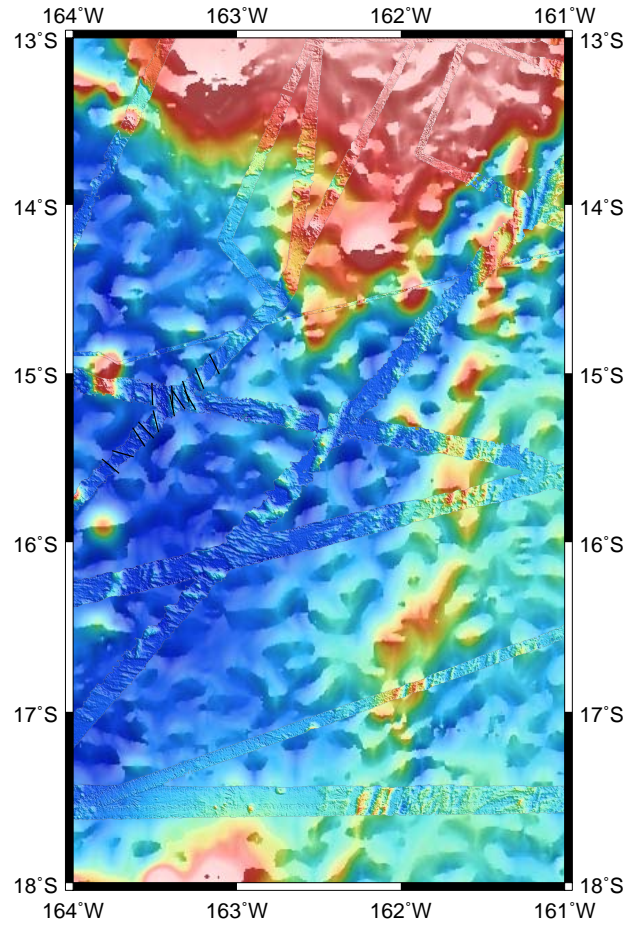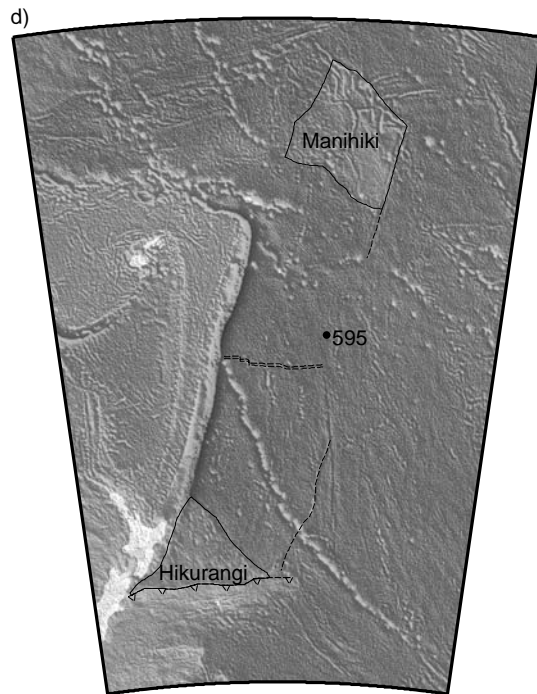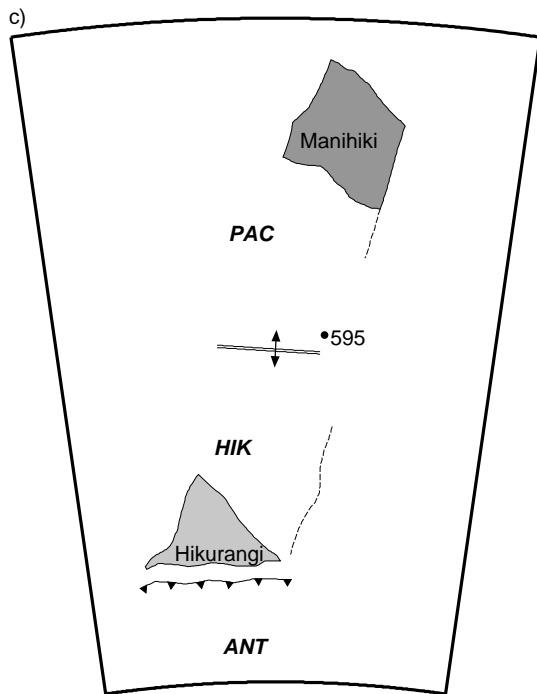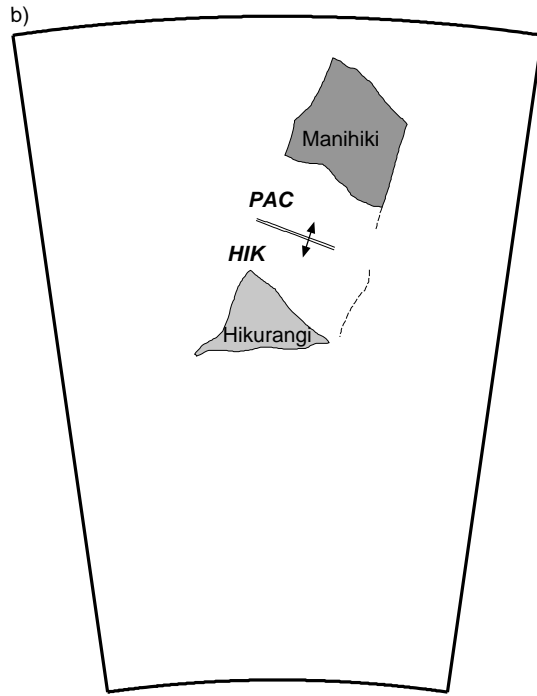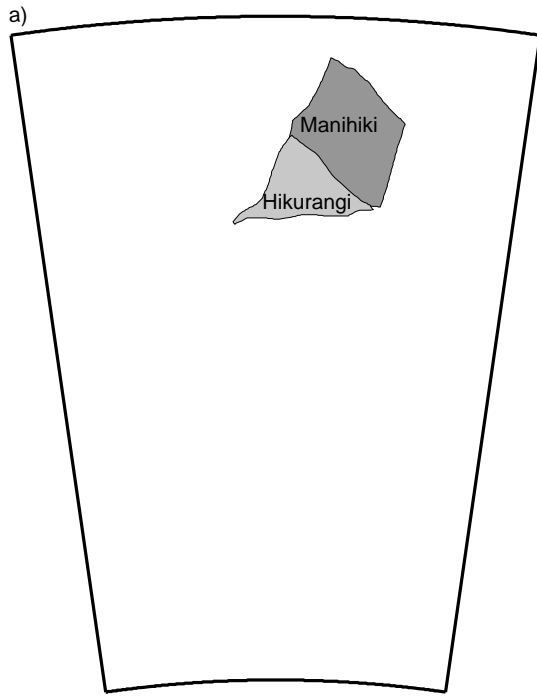
Figure 11: Tectonic model of the Osbourn region, presented in a Manihiki Plateau reference frame. Our model begins with the Hikurangi and Manihiki Plateaus conjugate, in agreement with Taylor's [2006] model. Spreading directions determined by abyssal-hill strikes are shown as double-headed arrows and the locations of the Southeast Manihiki and Western Wishbone Scarps are outlined with dotted lines. The Pacific Plate is labeled PAC, the Hikurangi plate HIK and the Antarctic sector of Gondwana ANT. **a)** Beginning location for the Manihiki and Hikurangi plateau. **b)** Configuration after 1200 km of total separation between the Plateaus. The spreading direction during the early history of the Osbourn spreading center roughly parallels the strike of the West Wishbone Scarp and the Southeast Manihiki Scarp. The formation of these scarps may be related to the plate boundary that existed here at this time, as implied by the differing azimuths of abyssal hills east and west of the southeast Manihiki scarp. **c)** The configuration of the Osbourn Spreading center immediately prior to the slowing of spreading. By this time the crust at DSDP site 595 has formed. **d)** The configuration of the Osbourn region at the time of extinction of the Osbourn Trough superimposed on the bathymetry of the Southwest Pacific Basin.

a)

b)

Manihiki

Hikurangi

Manihiki

PAC

HIK

Hikurangi

c)

Manihiki

PAC

•595

HIK

Hikurangi

ANT

d)

Manihiki

•595

Hikurangi

Chapter 4

INSTANTANEOUS DYNAMICS OF THE CRATONIC CONGO BASIN

Nathan J. Downey

Abstract

Understanding the formation mechanisms of cratonic basins provides an examination of the rheological, compositional and thermal properties of continental cratons. However these mechanisms are poorly understood because there are few currently-active cratonic basins. One basin thought to be active is the cratonic Congo basin located in equatorial Africa. The Congo basin is coincident with a large negative free-air gravity anomaly, an anomalous depression of the Earth's surface and a large positive upper-mantle shear-wave velocity anomaly. Localized admittance models show that the gravity anomaly cannot be explained by a flexural support of the topographic depression at the Congo. We analyze these data and show that they can be explained by the depression of the Congo basin by the action of a downward dynamic force on the lithosphere resulting from a high-density object within the lithosphere. We formulate instantaneous dynamic models describing the action of this force on the lithosphere. These models show that the gravity and topography of the Congo basin is best explained by viscous support of an anomalously dense region located at 100 km depth within the lithosphere. The density anomaly has a magnitude within the range of 27-60 kg/m^3 and is most likely compositional in origin. Our models do not provide a constraint on the lithospheric viscosity of the Congo craton because the shallow location of the anomaly ensures strong coupling of the anomaly to the surface regardless of viscosity structure. In addition we show that our models are consistent with results of tomographic imaging by using a filtering process to examine how various seismic-velocity structures within the upper mantle would be expressed in tomographic images.

1. Introduction

Our understanding of the rheology of the lithosphere comes primarily from observations and modeling of active and ancient lithospheric deformation. On a large scale, this deformation is usually coincident with either modern or ancient plate boundaries. Interpretation of these deformation processes becomes more difficult the farther back in time they occurred, due to tectonic overprinting or erosion. Consequently, for regions where little deformation has occurred or that have not recently been associated with plate boundary processes, such as continental cratons, there are few observational constraints on models of lithospheric rheology.

One type of cratonic deformation that has occurred throughout the geologic record is the vertical motions associated with the development of intracratonic sedimentary basins. These basins are observed in the major cratonic areas, and are often significant sources of hydrocarbons. As a result, these basins have been well studied, especially the Paleozoic Michigan, Illinois and Williston basins of North America. The relation between the forces driving intracratonic basin subsidence and the style and magnitude of that subsidence is determined by the structure, rheology and composition of cratonic lithosphere. For example the thickness of the lithosphere beneath North American intracratonic basins has been constrained using a model of two-dimensional thermal-lithosphere contraction resulting in basin subsidence [*Kaminsky and Jaupart*, 2000]. By modeling cratonic basin subsidence it is possible to estimate the rheology of the subcratonic lithosphere and asthenosphere and to quantify the magnitude of buoyancy within cratonic lithosphere. Thus, understanding the formation mechanisms of intracratonic basins is important not only for economic reasons, but also for understanding the mechanical properties of cratonic lithosphere.

Intracratonic sedimentary basins, defined in terms of their plate-tectonic setting, are those basins contained within continental interiors and not associated with plate boundaries [*Ingersoll and Busby*, 1995]. Despite the economic and geodynamic importance of intracratonic basins, their formation mechanisms are still not fully understood. This lack of understanding partly results from the unusual properties of these basins [*Sloss*, 1990].

Intracratonic basins typically undergo several periods of active subsidence, are extremely long lived and subsidence in different basins appears, at least on a long time scale, to be synchronous [*Leighton and Kolata*, 1990]. The most successful formation mechanisms rely on motions of anomalous masses in the lithosphere and/or asthenosphere caused by changes in the stress-state or thermal structure of the lithosphere during supercontinent breakup and/or formation [*DeRito et al.*, 1983; *Sloss*, 1990]. However, these models have not been fully explored because the relation between mantle flow and surface deformation was poorly understood when they were proposed. In addition, verification of these mantle flow models requires detailed knowledge of the dynamic subsidence and gravity fields associated with the basin-forming event. Since there are few modern active intracratonic basins these data are generally not available; the primary barrier to understanding intracratonic basin formation is the lack of modern active intracratonic basins.

Two intracratonic basins that are thought to be currently active are the Chad and Congo basins, situated in relatively close proximity within central Africa (Figure 1). The Chad basin is currently, and for much of its history since the Neogene has been, the location of a variable-sized lake at the center of an endoreic watershed. The sedimentary fill of the Chad basin covers an area of 8×10^5 km^2, is approximately 500 m thick and consists largely of lacustrine sediments deposited in a continental environment [*Burke*, 1976]. *Burke* [1976] hypothesized that deposition at the location of Lake Chad is a passive response to erosion of surrounding dynamic uplifts.

The Congo basin is much older, larger and deeper than the Chad basin, and also bears a greater resemblance to the Paleozoic intracratonic basins of North America. Covering an area of 1.2×10^6 km^2, roughly the size of Hudson Bay, the Congo basin is among the largest intracratonic basins. The basin straddles the equator in central Africa and is contained within the Congo craton, an amalgamation of crustal blocks that formed during the Proterozoic [*De Waele et al.*, 2008]. The seismically-determined crustal thickness of the Congo craton is within the range 30-45 km with thickest crust observed beneath the Congo basin [*Pasyanos and Nyblade*, 2007]. The basin overlies a faulted basement similar to that beneath the Williston. Sediment infill of the basin is up to 9 km thick and

consists of several unconformity-bounded packages that date in age from late Proterozoic to Quaternary [*Daly et al.*, 1992]. This pattern is similar to that observed in other intracratonic basins and indicates multistage basin development. The majority of these sediments are proposed to have been deposited in response to thermal contraction after a late Proterozoic rifting event. However, since the latest Jurassic or earliest Cretaceous the basin has been subsiding by an unknown mechanism.

Using gravity data acquired during the Gravity Recovery and Climate Experiment (GRACE) [*Tapley et al.*, 2005] and topography from the Shuttle Radar Topography Mission (SRTM) [*Farr et al.*, 2007], we reexamine the admittance (an estimate of the linear transfer function between topographic and gravitational spectra) of the Congo basin. The admittance estimates obtained using these data imply that the topography of the Congo basin is dynamically supported. Using active-source seismic data [*Daly et al.*, 1992] we construct a new isopach of the anomalous early-Cretaceous to Quaternary sediments. This isopach is used to correct the SRTM data to highlight the topographic structure of the anomalous subsidence of the Congo basin, which we hypothesize has a dynamic origin. We then present three-dimensional models of the instantaneous dynamics of the cratonic Congo basin, calculated using the convection code CitcomT [*Billen et al.*, 2003], which are constrained using this anomalous topography and gravity. We discuss the compatibility of these models with the deeper seismic velocity structure beneath the Congo as revealed by tomography. Our models demonstrate that the Cretaceous-Quaternary anomalous subsidence of the Congo basin results from viscous support of a high-density region in the uppermost mantle. The preferred location of this anomaly is at 100 km depth with a maximum density anomaly of 27-60 kg/m^3. The location of this anomaly within the uppermost mantle, however, makes it difficult to uniquely determine the viscosity structure of the Congo lithosphere.

2. Previous studies of the cratonic Congo basin

The Congo basin is located almost entirely within the Democratic Republic of the Congo (formerly Zaire and the colonial Belgian Congo), with its northern and northwestern extents reaching into the Republic of the Congo and the Central African Republic. It is

one of the least studied intracratonic basins due to its relative inaccessibility and long-term regional political instability. Geological study during colonial (pre-1960) times largely consisted of geological mapping [*Cahen*, 1954] with some preliminary geophysics [*Évrard*, 1957] and the drilling of two exploratory boreholes [*Cahen et al.*, 1959, 1960]. The major results of this colonial work are summarized in *Giresse* [2005]. Since 1960 the majority of geological study of the Congo basin has been carried out by oil exploration companies and is proprietary. However *Daly et al.* [1992] present an interpretation of seismic and well data collected in the early 1980's. Much of our current knowledge of the Congo basin's tectonic history is reliant upon interpretation of these seismic and well data.

As is typical for intracratonic basins, the Congo basin developed in stages. These stages are represented by four Paleozoic unconformity-bounded sedimentary sequences capped by a *ca*. 1-2 km thick late-Jurassic/early-Cretaceous to Quaternary sediment package [*Daly et al.*, 1992]. The oldest sedimentary rocks in the basin are late Proterozoic. It is not clear if rifting on the basin's basement faults predated or was coincident with deposition of the lowest sedimentary package. It is clear however that motion on these faults was reversed in response to collisional events related to the formation of Gondwana during the early and late Paleozoic [*Daly et al.*, 1991]. The evidence for these two collisional events is deformed, basinal sediments that are truncated by the sequence bounding unconformities. *Daly et al.* [1992] cite thermal relaxation after a late Proterozoic rifting event as the primary mechanism driving subsidence during deposition of the lower four stratigraphic packages. Since the early Mesozoic, the Congo craton has remained stable, with no internal collisional or rifting events taking place, making it difficult to determine the subsidence mechanism of the early-Cretaceous to Quaternary basin sediments. *Sahagian* [1993] tentatively proposes a passive sediment catchment model for this latest deposition within the basin, similar to that proposed by *Burke* [1976] for the Chad.

The lithosphere underlying the Congo basin is being compressed between the East-African Rift Zone and the Mid-Atlantic Ridge as evidenced from earthquake focal mechanisms [*Atalay*, 2002]. The state of stress in the North American craton during the

periods of active subsidence in the Michigan, Williston and Illinois basins is also thought to be compressional, as evidenced by the correlation of basin subsidence with orogenic events [*Sloss*, 1988]. Other geophysical characteristics of the Congo basin are not typical of intracratonic basins. *Hartley and Allen* [1994] observe a long-wavelength Bouguer gravity low over the Congo. This gravity anomaly in combination with the long-wavelength topographic expression of the Congo basin gives large admittance values at long-wavelengths, yielding an effective elastic thickness (EET) of 101 km for the lithosphere beneath the Congo basin [*Hartley and Allen*, 1994; *Hartley et al.*, 1996]. This estimate, while similar to estimates of EET in other cratonic regions, may only be an upper bound on the true elastic thickness of the Congo lithosphere [*McKenzie and Fairhead*, 1997]. Nevertheless, the ~2000 km wavelength of the Congo basin suggests that flexural support is not the primary mode of compensation for its topographic expression. *Hartley and Allen* [1994] suggest that the anomalous gravity and topography of the Congo basin results from the action of a downward dynamic force on the base of the lithosphere caused by convective downwelling in the mantle.

3. Observations and data

3.1 Gravity

The free-air anomaly gravity of Africa, derived from the GRACE satellite-only geopotential model GGM02S [*Tapley et al.* 2005], expanded out to degree l = 110 ($\lambda \approx 362$ km) shows that the Congo basin is coincident with an approximately 70 mGal free-air gravity low (Figure 2a). This gravity low is the dominant feature of the gravity field over continental Africa. A geoid height anomaly calculated from GGM02S for the same waveband (Figure 2b) is coincident with the Congo basin, but the correlation is less dominant than evidenced in the free-air anomaly; the Congo basin is coincident with an embayment in the longer wavelength Indian geoid low.

In order to explore the nature of this gravity anomaly we examine the free-air gravity spectrum using a spatio-spectral localization technique [*Simons*, 1996; *Simons et al.*, 1997]. The basis of this localization scheme is a windowing function centered at a

specific geographic location and derived from a spherical cap, a function on the surface of the sphere whose magnitude equals one within a specified angular radius from its central location and zero outside that radius. The spectrum of this windowing function is given by truncating the spectrum of spherical cap of radius θ_c at a maximum spherical harmonic degree of L_{win}. θ_c is given by:

$$\theta_c = \frac{\pi}{\sqrt{l_s(l_s + 1)}} \tag{1}$$

where $l_s = l / f_s$ is the ratio of the spherical harmonic degree of interest to a real-valued scaling factor $f_s \geq 1.0$. L_{win} is given by $L_{win} = \lceil l_s \rceil$ where $\lceil \bullet \rceil$ denotes the ceiling function. The Nyquist condition for this windowing process is given by:

$$L_{Nyq} = L_{obs} - L_{win} . \tag{2}$$

where L_{obs} is the maximum spherical harmonic degree of the observations. Two schemes for choosing f_s have been used. *McGovern et al.* [2002] chose f_s proportional to l so that l_s is constant, implying that θ_c and L_{win} are also constant. This choice results in a constant windowing function for all spherical harmonic degrees, most suitable for analyzing a particular geographic region. This windowing scheme has a constant spatial resolution, but a spectral resolution that increases with l. The Nyquist condition (2) for this windowing scheme, along with the bounds on f_s restricts the waveband over which this scheme can be applied to:

$$L_{win} \leq l \leq L_{obs} - L_{win} \tag{3}$$

Simons et al. [1997] use a different scheme for the windowing process in which f_s is constant for all windows, and as a result, window size varies with spherical harmonic degree, l. This scheme highlights the physical meaning of f_s, namely that it is the number of wavelengths contained within the windowing function. This scheme is well suited to analyzing large bandwidth signals. For different l, the wavelength varies and the window

size is dilated so that the spectral resolution remains constant and spatial resolution increases with *l*. The Nyquist condition for this windowing scheme is:

$$L_{Nyq} = \frac{f_s}{f_s + 1} L_{obs}.$$ (4)

These two windowing schemes are analogous to standard localized spectral analysis methods commonly used to analyze functions in the plane. The *McGovern et al.* [2002] scheme is similar to the 2D isotropic short-time Fourier transform, while the dilations of the window used in the scheme of *Simons et al.* [1997] are similar to the dilations of the 2D isotropic wavelet transform. By windowing a spherical harmonic field near a given location using this method we can then apply standard spectral analysis techniques in a localized sense.

The anomalous root-mean-square (RMS) amplitude spectrum of the GGM02S free-air gravity anomaly localized near the Congo basin at 22.00°E, 1.75°S is calculated by subtracting the globally-averaged local RMS amplitude spectrum of the free-air gravity from the RMS amplitude spectrum localized near the Congo (Figure 3). We utilize the windowing scheme of *Simons et al.* [1997] with a scaling factor, f_s = 1.5. The free-air gravity near the Congo has anomalously large amplitudes throughout waveband 10 < *l* < 45 (880 km < λ < 3817 km; Figure 3a). We use this spectral signature to design a filter that decomposes the GGM02S free-air gravity model into two parts. By using a band pass trapezoidal filter (*l* = 5-10-45-60) and its corresponding band reject filter it can be seen that the large gravity low associated with the Congo basin is wholly contained within the waveband of anomalously high RMS amplitude (Figures 2c and d). Even though we are focused upon a particular geographic region, we use the windowing scheme of *Simons et al.* [1997], with f_s = 1.5, in preference to that of *McGovern et al.* [2002] throughout this paper. Because the Congo gravity anomaly has a large bandwidth, the window size required to analyze the longest wavelength components of the gravity anomaly is much larger than that required to analyze the shortest wavelength components. Were we to choose a window large enough to analyze the entire signal, we would have poor spatial resolution at the shortest wavelengths of the gravity anomaly. Conversely by choosing a

smaller window we would be gaining spatial resolution at the expense of not being able to analyze the entire bandwidth of the gravity anomaly. The windowing method of *Simons et al.* [1997] provides a compromise between these two extremes.

3.2 Topography

The use of a global topographic model in which bathymetry is calculated by downward continuation of oceanic gravity anomalies, when comparing the spectral content of gravity and topography, will bias any estimation of the transfer function between gravity and topography to that of the downward continuation operation. This bias is easily avoided by using only ship track bathymetric measurements in the construction of a global topography model. We construct a new spherical harmonic representation of topography based upon the equivalent rock topography model ERT360 [*Pavlis and Rapp, 1990*] over oceanic regions. The ERT360 model, although dated, was created using only ship track bathymetric measurements for oceanic areas and is at sufficient resolution for our purposes. Over continental regions we use the SRTM topography data (Figure 1) for the construction of our model. Within this topographic model (expanded out to l = 110; Figure 4a), the Congo basin is outlined as a subtle depression in the topography which is not as anomalous as the Congo basin's gravity signature at these long wavelengths (*cf.* Figure 2). However, the topographic depression of the basin is almost circular in shape, a characteristic which is unique within Africa.

We again use the spectral localization method to calculate the RMS amplitude spectrum of the topography localized near the Congo basin (Figure 3b). The waveband $15 < l < 45$ (880 km $< \lambda < $ 2580 km) exhibits anomalous RMS topography whose amplitude peaks near l = 20 (λ = 1950 km) and decays to 0 at l = 40 (λ = 990 km). The RMS topography anomaly within the waveband $l < 15$ is much larger in amplitude. These large amplitudes result from the spectral expression of the extreme topographic variations associated with the ocean-continent boundary, especially the sudden transition from the high elevation of southern Africa to the ocean floor at the location of the south-African escarpments (Figure 1). The spectra of step-like features such as the continent-ocean boundary exhibit large amplitudes at all degrees. At $l > 15$ our windowing functions are small enough that

these transitions are masked out of the data and therefore do not affect our spectral estimates. However at the longest wavelengths our spatial windows become large and these features begin to dominate the spectrum of the topography.

3.3 Admittance between gravity and topography

The topography and gravity datasets described above are significant updates to the regional datasets used by *Hartley and Allen* [1994] and *Hartley et al.* [1996] in their analyses of the gravitational admittance of the Congo. These analyses also relied upon admittance spectra calculated using Bouguer gravity anomalies in their estimates of the EET of the Congo lithosphere. *McKenzie and Fairhead* [1997] warn that EET estimates based on Bouguer admittance can only be considered upper bounds to the true EET, due to the effect of erosional damping on short-wavelength components of the topography. It is prudent therefore to re-estimate the admittance spectrum of the Congo using our new datasets to verify the conclusions of *Hartley and Allen* [1994] and *Hartley et al.* [1996]. Since our datasets are global in scope, we again utilize spatio-spectral localization to restrict our admittance analysis to the Congo region.

Admittance analyses attempt to estimate the linear transfer function between topography and gravity. The most general linear transfer function between two functions, *A* and *B* defined on the surface of the sphere, Ω, is given by:

$$B(\hat{u}) = \int_{\Omega} F(\hat{u}, \hat{v}) A(\hat{v}) d\Omega .$$ (5)

The hat (ˆ) symbol is used to denote unit vectors pointing from the center of the sphere to a location (θ, ϕ) on the sphere's surface. Generally the transfer function between topography and gravity is assumed to be spatially invariant and isotropic (see *McNutt* [1979] for an exception). Under these assumptions, and assuming a particular noise model, the spectral coefficients of *F* can be estimated by the admittance, $Z(l)$ (see Appendix A):

$$Z(l) \equiv \frac{S_{gh}(l)}{S_{hh}(l)} = \frac{\sum_{m=-l}^{l} g_{lm} h_{lm}^*}{\sum_{m=-l}^{l} h_{lm} h_{lm}^*} \tag{6}$$

where g_{lm} and h_{lm} are the spherical harmonic coefficients of gravity and topography, respectively. $Z(l)$ is an unbiased estimate of the transfer function's spectrum [*Wieczorek, 2007*].

If our assumption of a spatially-invariant F_l is violated, then $Z(l)$ estimates a globally-averaged transfer function. However, we can examine the spatial variance in F_l using spatio-spectral localization. We denote the spherical harmonic coefficients of gravity and topography windowed near a point (θ_o, ϕ_o) by $\gamma_{lm}(\theta_o, \phi_o)$ and $\psi_{lm}(\theta_o, \phi_o)$ respectivly. Substitution of these windowed coefficients into equation (6) gives a local estimate of F_l:

$$Z(l, \theta_o, \phi_o) = \frac{S_{\gamma\psi}(l, \theta_o, \phi_o)}{S_{\psi\psi}(l, \theta_o, \phi_o)} . \tag{7}$$

Equation (7) assumes that F is spatially invariant within a window. By centering these windowing functions at different locations we can explore the spatial variance of the transfer function.

We use equation (7) to localize our estimate of admittance near the center of the Congo basin, using the same windowing scheme as described above for our estimation of the anomalous RMS amplitude spectra of gravity and topography (Figure 5a). There is relatively good correlation between the localized gravity and topography over the waveband $15 < l < 40$ (990 km $< \lambda <$ 2580 km), a waveband which also contains much of the power of the anomalous free-air gravity. Throughout this waveband the estimated admittance is > 25 mGal/km; the admittance is relatively constant at ~50 mGal/km for $25 < l < 40$. For comparison with the results of *Hartley and Allen* [1994] and *Hartley* [1996], we calculate synthetic gravity spherical harmonic coefficients assuming that the lithosphere responds elastically to the topographic load. In this model, the synthetic

gravity has two sources, the gravity anomaly caused by the topography and that caused by the flexural deflection of the Moho:

$$g_{lm}^F = g_{lm}^H + \left(\frac{R_E - T_c}{R_E}\right)^l g_{lm}^W \tag{8}$$

where the superscripts H and W indicate the spherical harmonic coefficients of gravity associated with the topography and Moho deflection respectively. The factor multiplying the Moho coefficients in equation (8) accounts for the upward continuation of these coefficients from the base of the crust at depth T_c to the surface at radius R_E. For the subtle topography of the Congo region the gravity coefficients on the right hand side of (8) can be approximated by:

$$g_{lm}^H = 4\pi\Delta\rho_H G \frac{l+1}{2l+1} h_{lm} \tag{9}$$

$$g_{lm}^W = 4\pi\Delta\rho_M G \frac{l+1}{2l+1} w_{lm}. \tag{10}$$

$\Delta\rho_M$ and $\Delta\rho_H$ are the density contrasts across the topographic and Moho interfaces, respectively and G is the gravitational constant. Coefficients of Moho deflection w_{lm} are calculated using the formulation for the flexural deflection of a thin spherical elastic shell [*McGovern et al.*, 2002; *Turcotte et al.*, 1981]:

$$w_{lm} = -\left(\frac{\Delta\rho_H}{\Delta\rho_M} \frac{l(l+1)-(1-v)}{\sigma(l^3(l+1)^3 - 4l^2(l+1)^2) + \tau(l(l+1)-2) + l(l+1)-(1-v)}\right) h_{lm} \tag{11}$$

where

$$\sigma \equiv \frac{\tau}{12(1-v^2)}\left(\frac{T_e}{R_E}\right)^2 \tag{12}$$

and

$$\tau \equiv \frac{ET_e}{R_E^2 g \Delta \rho_M} \ . \tag{13}$$

T_e is the thickness of the elastic shell, E is Young's modulus, g is the acceleration of gravity and ν is Poisson's ratio. We use equations (8)-(13) and the parameters listed in Table 1 to calculate synthetic gravity coefficients for values of the elastic thickness T_e = 0, 50, 100, 150 and 200 km. We then use equation (7) to estimate the localized admittance between the topography and these synthetic gravity fields near the Congo at 22.00°E , 1.75°S (Figure 5a).

While the overall fit of the admittance estimated using the GRACE gravity with the synthetic admittances is poor, the magnitude of the former is consistent with flexural models with T_e > 100 km over almost all of the waveband of good correlation between gravity and topography (Figure 5a). The plateau of ~50 mGal/km admittance for the 25 < l < 40 waveband is consistent with T_e ~ 200 km. The average magnitude of the Congo's admittance at long wavelengths (Figure 5a) is consistent with the T_e value of 101 km estimate of *Hartley and Allen* [1994] and *Hartley et al.* [1996]. In general continental regions exhibit T_e values much smaller than this, generally less than 25 km [*McKenzie*, 2003]. The unreasonably large T_e required to fit the modeled admittance to the GRACE admittance indicates that lithospheric flexure is not an important mode of compensation of the Congo topography. We agree with the conclusion of *Hartley and Allen* [1994] that there is likely a downward dynamic force, resulting from mantle convection, acting on the base of the Congo lithosphere. Furthermore we hypothesize that surface subsidence caused by mantle convection resulted in the deposition of the anomalous Mesozoic-Quaternary strata identified by *Daly et al.* [1992].

3.4 Cretaceous-Quaternary basin infill

In order to highlight the pattern of Congo basin dynamic subsidence we remove the anomalous late-Cretaceous to Quaternary sedimentary rocks from the topography. The removal process involved is similar to that of backstripping analyses [e.g., *Watts and*

Ryan, 1976]: remove the sedimentary basin infill from the topography by unloading its mass from the lithosphere assuming a compensation model.

We reinterpret the seismic data of *Daly et al.* [1992] with well control provided by the SAMBA and DEKESE wells [*Cahen et al.*, 1959, 1960] and the 1981 Gilson well to constrain the shape of the Mesozoic-Quaternary isopach (Figure 6). Time-depth conversions were performed using the refraction velocities determined at the SAMBA well by *Èvrard* [1957]. The lateral extent of these rocks was constrained by digitizing outcrop limits of the isopach from the Unesco International Geologic Map of Africa [*CGMW/Unesco*, 1987; Figure 6]. We then fit a smooth surface to these data using the MATLAB® gridfit subroutine [*D'Errico*, 2005]. The isopach map of these sediments shows they are oval in shape and reach ~1200 m in thickness (Figure 6). The region of significant sediment accumulation (> 50 m) measures ~1200 km east-west and 900 km north-south and is coincident with the location of the Congo free-air anomaly. As is typical of the sediment fill of intracratonic basins there is no evidence of significant sediment deformation in the seismic data.

In order to refine our estimate of the dynamic component of topography, we unload the anomalous isopach from the SRTM topography. Given the large area covered by these sediments we assume local compensation in which the corrected topography is given by:

$$H_{Corrected} = H_{SRTM} + \left(\frac{\rho_s}{\rho_m} - 1 \right) I \,. \tag{14}$$

where ρ_s and ρ_m are the bulk density of the sediment infill and mantle respectively and I is the sediment thickness. The density of the sediment infill is constrained by lithology and burial depth. Analysis of the well data indicates that $\rho_s = 2000$ kg/m³, and we assume a mantle density of 3300 kg/m³. Equation (14) gives a maximum topography correction of ~-475 m. We use the sediment-corrected SRTM topography to calculate a second spherical harmonic representation of topography and expand this corrected topographic field to $l = 110$ (Figure 4b). For comparison with the uncorrected topography we calculate the anomalous RMS amplitude spectrum of this corrected

topographic field (Figure 3b). As expected, given the large area covered by the Anomalous sedimentary rocks, sedimentation in the Congo basin has preferentially dampened the topography over the waveband $15 < l < 65$ (610 km $< \lambda <$ 2580 km) with relatively constant damping occurring over $20 < l < 50$ (790 km $< \lambda <$ 1950 km). Topographic modification caused by sedimentation also appears to be partially responsible for the large admittance associated with the Congo basin. Estimating the admittance using the sediment-corrected topography in place of the SRTM topography decreases the admittance within the waveband of anomalous gravity by ~10 mGal/km to ~40 mGal/km. Even after the sediments have been removed, however, the admittance remains too high to be explained by lithospheric flexure. Typical admittance values from cratonic regions are < 20 mGal/km at these wavelengths. Similar to the decomposition of the gravity into band-passed and band rejected components, we decompose the sediment-corrected topography into components using a similar trapezoidal filter (l = 10-15-45-60; Figures 4c and d). While restricted to a slightly smaller waveband, this decomposition demonstrates that the sediment-corrected topography is not only spatially-coincident with the Congo free-air gravity, but spectrally-coincident as well.

3.5 Tomographic structure of Congo lithosphere and asthenosphere

Global tomographic models of shear-wave velocity anomaly [*Ritsema et al.*, 1999; *Mégnin and Romanowicz*, 2000; *Gu et al., 2001*; *Grand*, 2002] generally agree on the velocity structure of the lithosphere and upper mantle beneath central Africa. Of these global models we choose S20RTS [*Ritsema et al.*, 1999; *Ritsema and van Heijst*, 2004] to be representative of the general pattern observed (Figure 7). This velocity structure consists of a region of approximately +5% maximum-amplitude shear-wave velocity anomaly, relative to the Preliminary Reference Earth Model (PREM) [*Dziewonski and Anderson*, 1981], located at a depth of ~150 km beneath the Congo basin (Figures 7a, c and d). The anomalous high velocity region decays to +1% at ~300 km depth (Figures 7b, c and d). Velocities consistent with PREM (0%) are reached at a much greater depth, ~800 km (Figures 7c and d). The horizontal extent of this region covers the entire Congo basin and is connected with a region of similar anomalous velocity beneath southern

Africa (Figure 7a). In S20RTS, the Congo velocity anomaly forms a local maximum distinct from the velocity maximum beneath southern Africa.

Regional models of the shear-wave velocity anomaly beneath Africa, calculated using Rayleigh-wave phase velocities, are not as consistent. *Ritsema and van Heijst's* [2000] model was calculated using a subset of the data used in S20RTS, and exhibits a similar pattern of shear-wave velocity anomaly, although resolution is poor at depths greater than 250 km. *Fishwick* [2007] presents a model based on an updated dataset relative to that of *Ritsema and van Heijst* [1999]. This dataset was constructed with an emphasis on high-quality data and the resulting velocity structure is very similar to S20RTS. Both of these models indicate that shear-wave velocity anomalies beneath central Africa are strongest beneath the Congo basin at a depth of 100-150 km. In contrast, the model of *Pasyanos and Nyblade* [2007] characterizes the upper mantle beneath parts of the Congo craton with anomalously high velocities; however, the region immediately below the Congo basin is not anomalous. *Pasyanos and Nyblade's* [2007] model does indicate that the sediments of the Congo basin make up the upper 20% of a 45 km thick crust, the thickest observed on the African continent. *Pasyanos and Nyblade* [2007] interpret the absence of anomalously fast velocities in the upper mantle beneath the basin as indicative of a missing cratonic keel, proposing that the Congo basin overlies a hole in the cratonic mantle lithosphere. *Pasyanos and Nyblade* [2007] attribute the difference between their model and previous models to poor horizontal resolution in the latter: the Congo basin is surrounded by anomalously fast lithosphere which, in these models, has been "smeared" into the upper mantle beneath the Congo basin.

Shear-wave velocities are sensitive to temperature because of the strong temperature dependence of the shear modulus [*Priestly and McKenzie*, 2006]. As the temperature within the mantle approaches the melting temperature the magnitude of the shear modulus is reduced and seismic velocities decrease. Temperature is also an important, but not exclusive, control on density throughout the mantle, with the coefficient of thermal expansion being $\sim 10^{-5}$ K^{-1}. Cold regions within the mantle are therefore denser and have greater shear wave velocities than their warmer surroundings. If the velocity anomaly beneath the Congo basin as shown in S20RTS is a robust feature, it may indicate

the presence of an anomalously dense region in the upper mantle beneath the Congo, consistent with dynamic support of the Congo basin's anomalous topography.

4. Instantaneous dynamics of the cratonic Congo basin

4.1 Dynamic models of cratonic basin subsidence

Mantle dynamics has long been hypothesized to play a role in intracratonic basin subsidence. *DeRito et al.* [1983] demonstrated using semi-analytical models of viscoelastic beam flexure, that stress changes in the lithosphere could cause anomalous high-density flexurally-compensated bodies within the lithosphere to become unstable, flow, and essentially relax toward an isostatic state. Accompanying this flow is a depression of the surface, causing the formation or re-activation of subsidence in an intracratonic basin. *Middleton* [1989] presented a model in which intracratonic basin subsidence is caused by the combined effects of dynamic topography and thermal contraction over an asthenospheric downwelling or "cold spot". *Middleton* [1989] noted however that permanent subsidence resulting from this mechanism is difficult to achieve, requiring that a fraction of sediment be preserved above base-level as the basin is uplifted in response to removal of the cold spot. Models of intracratonic basin subsidence caused by downward flow of dense eclogite bodies within the cratonic lithosphere roughly predict the subsidence histories of the Michigan, Illinois and Williston basins [*Naimark and Ismail-Zadeh*, 1995]. However, attempts at modeling the role of mantle dynamics in intracratonic sedimentary basin subsidence have had limited usefulness; inadequate observational constraint makes it difficult to uniquely determine model parameters.

The geophysical and geological observations of the Congo basin provide a unique and unprecedented opportunity to study the role dynamic topography plays in cratonic basin subsidence. The correlation of the Congo gravity anomaly, anomalous topographic depression and upper mantle shear-wave velocity anomaly is striking. Nowhere else are these quantities correlated at such large wavelengths. Furthermore these data combine to provide tight constraints on the dynamic processes currently depressing the Congo lithosphere.

4.2 Calculation of model topography and gravity

The observations outlined in section three only constrain the current state of the Congo basin. There is no information about the evolution of the basin contained in the gravity, topography or shear-wave velocity anomaly associated with the basin. Therefore, following the approach of *Billen et al.* [2003], we solve only the conservation of mass and momentum equations and not the energy equation when calculating the dynamic topography.

Under the infinite Prandtl number and Boussinesq approximations, the force balance between mantle density anomalies and surface deflection is governed by conservation of mass, as expressed by the continuity equation:

$$\vec{\nabla} \cdot \vec{u} = 0 \tag{15}$$

and conservation of momentum as expressed by the Stokes equation:

$$\vec{\nabla} \cdot \widetilde{\sigma} + \vec{f} = \vec{0} \tag{16}$$

where $\vec{u}$ is the velocity vector, $\widetilde{\sigma}$ is stress and $\vec{f}$ is the body-force. The over-arrow and over-tilde notations indicate vectors and second order tensors, respectively. We adopt a Newtonian-viscous constitutive relation:

$$\widetilde{\sigma} = -P\widetilde{I} + \eta\widetilde{\dot{\varepsilon}} \tag{17}$$

in which $\widetilde{I}$ is the identity tensor, P is pressure, η is the dynamic viscosity and $\widetilde{\dot{\varepsilon}}$ is the strain-rate tensor defined as:

$$\widetilde{\dot{\varepsilon}} = \vec{\nabla}\vec{u} + (\vec{\nabla}\vec{u})^{\mathrm{T}}. \tag{18}$$

The body-force is given by:

$$\vec{f} = \rho_o \alpha (T - T_o) g\hat{r}. \tag{19}$$

T is absolute temperature, T_o is a reference temperature, ρ_o is a reference density, α is the coefficient of thermal expansion and $\hat{r}$ is the radial unit vector. Non-dimensionalizing using the definitions:

$$\vec{u} = \frac{\kappa}{R_E}\vec{u}', \qquad P = \frac{\eta_o\kappa}{R_E^2}P'$$

$$\eta = \eta_o\eta', \qquad \vec{\nabla} = \frac{1}{R_E}\vec{\nabla}', \qquad T = T_o + \Delta T T' \tag{20}$$

where κ is the thermal diffusivity, η_o is a reference viscosity and ΔT is the temperature difference between Earth's surface and the mantle's interior, yields from (15):

$$\vec{\nabla}'\cdot\vec{u}' = 0 \tag{21}$$

and from the combination of (16)-(19):

$$-\vec{\nabla}'P'\widetilde{I} + \vec{\nabla}'\cdot(\eta'\vec{\nabla}'\vec{u}' + \eta'(\vec{\nabla}'\vec{u}')^T) + RaT'\hat{r} = \vec{0} \tag{22}$$

where the non-dimensional Rayleigh number, Ra, is:

$$Ra = \frac{\rho_o\alpha\Delta T g R^3}{\eta_o\kappa}. \tag{23}$$

Ra is a measure of the relative importance of buoyancy and viscous resistance. Values of the parameters used in the models presented here give a Rayleigh number of 4.35×10^8 (Table 2).

We solve equations (21) and (22) for P' and $\vec{u}'$ in spherical coordinates using the finite-element (FE) mantle convection code CitcomT [*Billen et al., 2003*]. Our model domain consists of an 80° by 80° spherical sector centered on the equator whose depth ranges from the surface to 2890 km, the core-mantle boundary (CMB; Figure 8). The total number of elements in each dimension is 216. The grid spacing varies in latitude and longitude with the innermost 34° by 34° region having a constant grid spacing of 0.2°

which increases linearly outside this inner region to 2.75° at the model boundaries. Depth grid spacing is 7 km over the uppermost 700 km, linearly increasing beneath to 40 km at the CMB. Boundary conditions are reflecting ($u_{\phi\phi} = 0$ or $u_{\theta\theta} = 0$ and $\sigma_{r\theta} = \sigma_{r\phi} = 0$) on the side walls of the model and free-slip ($u_{rr} = 0$, $\sigma_{r\theta} = \sigma_{r\phi} = 0$) on the upper and lower surface. In addition, non-dimensional temperature, T', equals 0 on the upper surface and 1 at the CMB. The equatorial position of the model domain ensures its symmetry about the equator. For comparison with observations the results obtained on this domain are rotated, preserving north so that the center of the model domain coincides with the center of the Congo basin at 22.00°W, 1.75°S.

CitcomT utilizes the consistent boundary flux (CBF) method [*Zhong et al.*, 1993] to calculate the normal stress on the upper surface of the model domain. Rather than attempt to calculate the normal stress on this surface, σ_{rr}, using the constitutive relation (17) the CBF method uses the solution to the model pressure and velocity fields (P' and $\vec{u}'$) to solve the Stokes and continuity equations for the normal stress directly on the upper free surface of the model. *Zhong et al.* [1993] demonstrate that the CBF method is substantially more accurate, in terms of relative errors, than calculating the normal stress by smoothing element stresses on the free surface. *Billen et al.* [2003] benchmarked this procedure for the spherical problem solved by CitcomT.

Dynamic topography is the topography that results in response to the normal stress imposed on the surface by viscous flow in the mantle. Because of the large wavelength of the anomalous topography observed in the Congo we adopt a model in which the surface-normal stress is balanced by isostatic adjustment of the Earth's surface:

$$H_M = \frac{\sigma_{rr}}{\Delta\rho_{fill}g} \tag{24}$$

where H_m is the model topography and $\Delta\rho_{fill}$ is the density contrast between the uppermost mantle and the material infilling the surface deflection. For our models, we compare this modeled topography to the sediment-corrected topography calculated in

Section 3 and therefore the infilling material is air and $\Delta\rho_{fill}$ is equal to the reference density ρ_o.

The model gravity consists of two parts, the gravity due to the variations of density within the mantle and the gravity due to the mass deficit created by the dynamic topography. The spherical harmonic coefficients of the gravity at Earth's surface ($r = R_E$) due to the internal density structure, $\rho(r,\theta,\phi)$, are calculated using:

$$g_{lm}^I = G \int_{R_{CMB}}^{R_E} \left(\frac{r}{R_E}\right)^{l+2} \frac{l+1}{2l+1} \int_{\Omega} \rho(r,\theta,\phi) Y_{lm}^*(\theta,\phi) d\Omega dr \qquad (25)$$

where $Y_{lm}(\theta,\phi)$ is a spherical harmonic (see Appendix A) and $d\Omega = \sin(\theta) d\theta d\phi$. The spherical harmonic coefficients and the integral over r are calculated within CitcomT using the numerical quadrature method used in the FE computation. The topographic component of the gravity is calculated using a modified version of (25) in which the integral over r and the upward continuation factor are dropped because the topographic density anomaly is located at the upper surface of the model. This density anomaly equals the model topography scaled by the surface density contrast $\Delta\rho_s$:

$$g_{lm}^H = G \frac{l+1}{2l+1} \Delta\rho_s h_{lm} = G \frac{l+1}{2l+1} \int_{\Omega} H_M(\theta,\phi) Y_{lm}^*(\theta,\phi) d\Omega \qquad (26)$$

where h_{lm} are the spherical harmonic coefficients of the model topography, H_M. The magnitudes of these two components of gravity are similar and opposite in sign because a positive density within the mantle causes a negative density anomaly at the surface. The total gravity anomaly is therefore relatively small in magnitude compared to either the gravity from internal density variations or the surface deflection and therefore these two gravity components must be calculated as accurately as possible. The consistent boundary flux method therefore also facilitates accurate calculation of the model gravity anomaly.

4.3 Model setup

The shape of the input density structure of our models is described by a cyndrically symmetric bi-variate Gaussian density anomaly at a specified depth (Figure 9a). The axis of symmetry is vertically oriented beneath the center of the Congo basin at 22.00°E, 1.75°S. The horizontal width and vertical thickness of these anomalies is specified by their half-width and half-thickness (the distance at which the magnitude of the Gaussian drops to one-half maximum). The half-width is measured along the surface of the Earth so that deeper models, while having a smaller absolute width, have the same angular width as shallower models. Thus the shape of these density anomalies, when the half-thickness is less than the half-width is an oblate spheroid. In general, we run these models in groups containing 21 members of constant width whose depth location varies from 50 km to 500 km and whose half-thickness at each depth varies from 50 km to a maximum equal to their depth. The magnitude of the maximum density anomaly of each group member is varied so that the total anomalous mass of each member is constant within a group.

The viscosity of our models is described using the relation:

$$\eta = \eta_o \exp\left(\ln(r) \frac{1 - f(\vec{x})}{1 + v_T f(\vec{x})} \right) \tag{27}$$

in which $f \in [0,1]$ is a function of position $\vec{x}$, r is the ratio of maximum to minimum viscosity and v_T describes the decay of viscosity with increasing f (Figure 10). This relation is similar to that used by *Conrad and Molnar* [1999] in which non-dimensional temperature has been replaced by f and to which we have added the parameter v_T. For the background viscosity, f equals the ratio of depth to lithospheric thickness within the lithosphere and equals 1 throughout the sub-lithospheric mantle (Figure 9b). The viscosity of the density anomalies is calculated using the same bi-variate Gaussian geometry to describe the spatial distribution of f. The maximum viscosity of the anomalies is expressed in terms of the depth at which the maximum viscosity equals the background viscosity, symbolized η_{eqv} depth and expressed in km (in Figure 9c, η_{eqv}

depth = 50 km, so the maximum viscosity of the anomaly equals the background viscosity in Figure 9b at 50 km depth). The viscosity at any given location is taken to be the larger of the background and anomalous viscosities (Figure 9d). Within each group of models we use the same viscosity parameters and background viscosity. This is done to ensure that while the mass distribution of each group member may be different, its mass remains mechanically coherent. In addition we explore the effects of a viscosity increase beneath the lithosphere by specifying, for some models, a transition depth beneath which the viscosity increases by a specified ratio over a depth of 100 km beneath which viscosity remains constant. Specifying the total anomalous mass for different sized anomalies, while keeping a similar viscosity structure means that we must specify the input viscosity independently from the input density and therefore cannot use a temperature-dependent viscosity. The input temperature field used when solving equation (22) is obtained by mapping our specified densities into "effective" temperature. We specify the viscosity input to CitcomT directly.

While we have parameterized our input density in terms of temperature, this density can have either a compositional or thermal component. Since we are solving only for the instantaneous flow we do not need to distinguish between density anomalies arising from composition and those arising from temperature. This approach also has some additional benefits. In cratonic regions, lithospheric instability may only occur within the lower extent of the thermal boundary layer and be driven by compositional effects, perhaps due to phase changes [*O'Connell and Wasserburg,* 1972; *Kaus et al.*, 2005]. Compositional buoyancy may also be responsible for the apparent long-term stability of cratonic lithosphere [*Jordan,* 1978; *Kelly et al.*, 2003; *Sleep*, 2005]. Comparing our best-fit input density models with density anomalies associated with different mineral phase changes may allows us to discern the relative roles of compositional and thermal density changes in cratons. Using temperature to determine both the density and viscosity variations within the mantle also assumes a functional relationship between temperature, density and viscosity [see *Hirth and Kohlstedt*, 2003]. Incorporating this relationship into dynamic models of mantle convection often requires the use of parameters that disagree with experimental results to explain observations. Our approach is to find a suite of

viscosity and density structures that match observations and then determine any implications these structures have on the functional relationship between density and viscosity.

4.4 Results

Preliminary modeling quickly showed that a half-width of 600 km provided the best fit to observations, regardless of the viscosity structure, for anomalies contained within the upper mantle (we tested models ranging in half-width from 100 km to 800 km). This is most likely due to the large horizontal extent of the Congo gravity anomaly, along with our placement of the density anomaly within the upper mantle region. It is this region that contains the seismic velocity anomaly observed in S20RTS. As a result, we only discuss model groups with 600 km half-width here. The parameters of model groups we do discuss are given in Table 3 along with the depth, thickness, misfit and maximum density contrast associated with the best-fit model of each group.

The thickness and depth of the density anomalies controls their coupling to the surface as illustrated by the trends in the magnitude of the topographic depression (Figure 11). For group 3 (Figure 11a), as the density anomalies are placed deeper, the resultant deflection of the surface decreases. Note that this occurs even as the anomalies get thicker as the total anomalous mass remains constant. Thicker anomalies, however, have larger deflections for a given depth than do thinner ones, resulting from the greater viscous coupling to the surface. This effect is reduced if the maximum viscosity of the anomalies decreases: the only difference between group 3 and group 6 in Figures 11a and 11c is η_{eqv}, which equals 50 km for group 3 and 100 km for group 6. Note, however, that for a given depth the topographic deflection within group 6 is relatively constant compared with the higher-viscosity anomalies of group 3. For anomalies with a 50 or 100 km half-thickness, increasing the rate at which the background viscosity decays determines the magnitude of the decrease in topographic deflection (Figure 12). Model groups in which the anomalies have a viscosity similar to that of the uppermost lithosphere, or in which the viscosity decays more slowly with depth (groups 1 and 8; Figures 11b and 11d) exhibit increased topographic deflections with depth for a few cases (i.e., 100 km half-

thickness in Figure 11d and 200 km half-thickness in Figure 11b). In addition, the models with the maximum topographic deflection within these groups have larger half-widths. While these deflections are larger in magnitude, they are also narrower in width (Figure 13). Thus the thick high-viscosity region associated with these models focuses the distribution of stress on the surface to a narrower region.

The symbol size in Figure 11 is proportional to the topographic misfit for each model (Appendix B). The topography, taken by itself, does not strongly constrain our models because while for the models in Figure 11, the topography is fit best by shallow models, increasing the total mass anomaly would shift the best fitting models deeper.

The topographic component of the gravity follows the same trends outlined above for the topography, however the addition of the gravity due to the density anomaly changes these trends somewhat when considering the total gravity anomaly (Figure 14). The gravity due to the density anomaly decays much faster, as density anomalies shift deeper, than does the topography. This is seen in Figure 14a where, for shallow depths, the gravity has a magnitude of -40 mGal. As the mass anomaly gets deeper, the positive gravity due to the mass anomaly decreases rapidly and therefore cannot counteract the large negative gravity anomaly caused by the topographic deflection. Thus for deep models in Figure 14a, the gravity is extremely negative (near -100 mGal). This effect is even stronger for models in which the density anomaly remains strongly coupled to the surface at greater depths (Figures 14b and 14d). For group 6 this effect is not as strong because of the reduced topographic deflection for the deeper models due to weak surface coupling. From Figure 11c it can be seen that the topographic depression for the deepest models in group 6 is less than the deepest models of the other groups in Figure 11. When the density anomaly is placed deep in the mantle, its influence on observed gravity is minimal; the observed gravity is that due to the surface deflection, which is smaller for group 6 than for the strongly coupled models.

Another interesting effect seen in Figure 14 for models with 50 km half-width is an increase in the goodness of model fit as the density anomaly gets deeper. This occurs because for the deeper models, the topography and its gravity anomaly are reduced

because of reduced surface coupling. At the same time the magnitude of the gravity due to the density anomaly is also reduced because it is deeper in the mantle. Since the net gravity is the difference of these two magnitudes this difference matches observations better than if either quantity were larger. This is true in general and it is possible to match the observed gravity well even when the topographic deflection is under or over predicted. An example is model I924, the best fitting model in group 12 (Table 3). This model fits the gravity well but the topography poorly. Thus, the gravity taken alone is not a sufficient constraint on the density and viscosity of our models.

The gravity and topography taken together do provide a stronger constraint on the density and viscosity of our models. The topographic deflection is related to the anomalous density via the viscosity structure and determines the topographic component of the gravity. The total gravity is, in addition, also directly sensitive to the input density. The tradeoffs discussed above, associated with fitting either the topography or the gravity alone are therefore eliminated. This can be seen in the plots of model admittance and total model fit (Figures 15 and 16). Both these quantities are sensitive to topography and gravity. The best fit model admittances occur for models at 100 km depth. Models situated deeper in the mantle have a very large gravity anomaly compared to the topographic deflection and therefore admittances are large. Conversely, anomalies at a shallower depth have a subdued gravity due to the increasing gravitational influence of the anomalous mass compared to that of the topography (in the limit of a density anomaly at the surface the total gravity goes to zero). The total misfit shows a similar pattern to the admittance with best fitting models corresponding to a density anomaly at 100 km depth. The overall best fitting model is in group 3, located at 100 km depth and with a 100 km half-thickness (Table 3). The best fitting models for all groups (except group 12 as discussed above) with an isoviscous lower mantle are located at 50 or 100 km depth with most occurring at 100 km. These best-fitting models are also relatively thin with half-thicknesses of either 50 or 100 km. The overall best-fitting model, I546 in group 3, matches the observed gravity, topography and admittance well: The residual gravity and topography anomalies are small and the anomalous gravity, topography and admittance

spectra are well reproduced (Figures 17, 18 and 19). The other models in Table 3 whose total misfit is less than about 0.540 fit similarly well.

Our best-fitting models provide a better constraint on the density structure than on the viscosity structure. The total anomalous mass of the best fitting models in Table 3 ranges only from 8-10×10^{18} kg. Since these anomalies are constrained to be relatively thin and contained within the lithosphere, this corresponds to a maximum anomalous density range of 27-60 kg/m^3. Increasing or decreasing the anomalous mass outside this range results in models which fit the data poorly. It is possible to achieve a better fit for larger anomalous masses by providing some support to the anomalies by introducing a viscosity increase for the lower mantle. Groups 5 and 13 have the same total anomalous mass; however, the best fitting model in group 13 is situated 300 km deep, beneath the lithosphere and in a location where some of the mass is supported by the higher viscosity transition zone and lower mantle. In contrast, the best fitting model of group 5 is located at 50 km depth, but fits much more poorly. An increase in viscosity beneath the lithosphere, however, has little effect on the fit of the anomalies situated within the lithosphere: The 50 km thick 50 km deep density anomaly in group 13 fits the data about as well as that of group 5 with a total misfit of 0.633 vs. 0.638. We cannot uniquely determine the magnitude of the viscosity increase from the upper to lower mantle because there is a tradeoff between the depth of the viscosity increase and the magnitude of that increase (Compare groups 13 and 14 in Table 3). From Table 3 it can be seen, however, that these deeper models supported by a high-viscosity lower mantle fit the gravity much less well than the best-fitting models with density anomalies located at shallower depths for groups with less total mass. This poor fit results from the upward continuation of the gravity due to the density anomaly. For these deep density anomalies, a large mass is required to fit the topography adequately; however, upward continuation of the gravity due to the mass anomaly shifts its spectral content out of the band containing the anomalous Congo basin gravity by preferentially damping shorter wavelengths. This effect can be counteracted by decreasing the width of the anomaly, in effect making the gravity shorter wavelength before upward continuation; however doing so results in a poorer fit to the topography, which is not affected by the spectral dampening related to

upward continuation. Thus the near coincidence of the spectral content of the anomalous topography and the anomalous gravity implies a shallow source of the mass anomaly resulting in topographic deflection.

Unfortunately, we are not able to constrain the viscosity structure of the lithosphere with our models. The three best-fitting individual models in Table 3 have the same mass anomaly with the same maximum viscosity, but have significantly different background viscosity profiles. Furthermore, we can also achieve a very good fit using a model in which the maximum viscosity of the anomaly is significantly less than the maximum viscosity anomaly of our overall best-fit model. This inability to constrain the viscosity structure within the lithosphere probably results from the shallow location of the density anomaly. At these depths there is no significant difference in the strength of coupling between the anomaly and the surface for different viscosity structures. As a result, these various viscosity structures result in a similar topographic depression at the surface for shallow density anomalies (Figure 11).

4.4 Calculation of synthetic tomographic images

In addition to our dynamic solutions we also create synthetic tomographic images for our various input models. We utilize the filtering procedure of *Ritsema et al.* [2007] to obtain the images expected for our input model geometries, assuming resolution characteristics consistent with S20RTS (Figure 20). Previous authors have used either empirical calibration of shear-wave velocity and temperature [e.g., *Priestly and McKenzie*, 2006] or have relied on mineral physics constraints to scale temperature perturbations into velocity perturbations [e.g., *Tan and Gurnis*, 2007]. However, we assume that the shear wave velocity anomaly resulting from our models follows the same bi-variate Gaussian pattern and has unit amplitude. This approach avoids the need to scale geodynamic variables by poorly-determined conversion factors (see *Karato* [2008]). In order to quantify the fit between the synthetic images and those of S20RTS, we derive a misfit parameter based on the correlation coefficient which is localized horizontally using the same spatio-spectral localization used for the gravity and topography, and localized to the upper mantle using a combination of the S20RTS basis splines (see appendix B).

The local correlations observed for the various input models ranges from 0.28 to 0.47 (Figure 21). At the long wavelengths associated with S20RTS (we are restricted to $l <$ 20, which for $f_s = 1.5$ yields $L_{Nyq} = 12$), our windowing functions include a large area surrounding the Congo basin where our models are not defined, resulting in the overall low correlation values in Figure 17. However, these correlation values still provide a relative measure of model fit. The greatest variation in correlation occurs for models with a 50 km half-width, with the overall best and worst fitting models occurring at 100 and 200 km, respectively. That these models occur at adjacent depths is indicative of the rapid change with depth in shear-wave velocity anomaly that occurs in the uppermost regions of S20RTS beneath the Congo (Figure 7). At 100 km half-thickness the depth variation of correlation is decreased, however the best-fit model still occurs at 200 km depth. For half-thicknesses greater than or equal to 200 km, all models fit the observations equally well. This lack of variation results from the relatively constant shear-wave velocity anomaly of S20RTS over these larger depth ranges within the upper 800 km of the mantle beneath the Congo basin.

5. Discussion and conclusions

The observations outlined in Section 3 demonstrate that the Congo basin's surface is currently being depressed in response to the downward flow of an anomalously dense region in the mantle. This geodynamic scenario is similar to that generically proposed by *DeRito et al.* [1983] and *Naimark and Ismail-Zadeh* [1995] in which density anomalies like the one observed described here periodically become unstable and cause subsidence of intracratonic basins. While our observations do not indicate what stage of the subsidence process the Congo basin is currently undergoing, they do provide the best evidence thus far that intracratonic basin subsidence is driven by dynamic topography and that the most recent depression of the Congo basin is dynamically maintained. Models in which anomalous masses within the cratonic lithosphere become unstable in response to global tectonic events are also the most plausible mechanism to explain the long-period near-synchronicity of intracratonic basin subsidence worldwide [*Sloss,* 1990].

The gravity and topographic anomalies associated with the Congo basin also provide constraints on the density structure of the lithosphere. Simultaneously fitting both gravity and topography allow us to determine the magnitude of the total mass anomaly associated with the Congo anomaly. We are also able to constrain this anomaly as being located within the lithosphere at a depth of 100 km. The maximum density contrast across this anomaly ranges from 27-60 kg/m^3, depending on its half-width and thickness. If the density anomaly has a thermal origin this corresponds to a temperature drop of 409-909 K, relative to ambient mantle, assuming a thermal expansivity, α, of 2×10^{-5} K^{-1}. Such a large temperature anomaly implies that the lithosphere beneath the Congo basin has a temperature similar to that of the crust. Correspondingly, the viscosity of such a cold mantle region should be very large [*Priestly and McKenzie*, 2006]. Our modeling results do show, however, that even for a linear viscosity profile through the lithosphere the observations are not fit well. It is much more likely that the origin of these large density anomalies is largely compositional. Density changes associated with the eclogite phase transition can easily explain the observed density contrasts without requiring the presence of a large thermal anomaly and associated high viscosities beneath the Congo basin [*Anderson*, 2007].

We are not able to tightly constrain the viscosity of the lithosphere beneath the Congo basin. This inability arises from the location of the preferred anomaly in the uppermost mantle where it is tightly coupled to the surface for a range of viscosity structures, including exponential and two super-exponential decay rates. It does appear that a linear viscosity profile through the lithosphere is inconsistent with observations. Thus we are unable to determine the exact nature of the decrease in lithospheric viscosity with depth.

Our final constraint on the density and viscosity structure of the lithosphere comes from the analysis of the shear-wave velocity anomaly observed beneath the Congo basin. This analysis shows that the location of a large seismic velocity anomaly within the lithosphere is consistent with the tomographic results. However the exact placement of that anomaly appears deeper in the lithosphere than our preferred models. This difference in location may result from an offset of the location of the center of the density anomaly and the location of maximum seismic velocity anomaly. For example, a region

of constant seismic velocity with depth will have a greater velocity anomaly at greater depths relative to PREM due to the increase in background velocity within PREM. In this analysis we have ignored the amplitude of the seismic velocity anomalies when comparing various models and the resolution of S20RTS limits us to very large scales. Perhaps a more detailed analysis including an analysis of predicted amplitudes of the seismic anomalies and a higher resolution model will provide more constraints on the structure of the Congo lithosphere. Another implication for the tomographic analysis is the influence of composition on seismic velocity. *Anderson* [2007] shows that for eclogitic bodies within the uppermost mantle, density and seismic velocity are not strongly correlated. Indeed it is possible to have a high-density region which is not observed seismically. If this is indeed the case beneath the Congo basin, and the density anomaly is caused by an eclogite phase transition, this may explain the lack of lithospheric root beneath the Congo basin observed in the tomographic model of *Pasyanos and Nyblade* [2007].

In conclusion, the observations of topography, shear-wave velocity anomaly and gravity at the Congo basin indicate a dynamic origin for the depression of the basin's surface. These observations taken together indicate that the density anomaly causing this subsidence is located within the upper mantle at a depth of 100 km. In addition the magnitude of this density anomaly is 27-60 kg/m^3, a range most consistent with a compositional origin. We are not able to constrain the exact nature of the viscosity structure of the lithosphere. It does appear, however, that the decay of viscosity with depth is exponential or super-exponential. While we cannot claim our models fit the data uniquely, due to the nonlinear nature of mantle convection, it does appear that our best-fitting models are the most reasonable assuming realistic lithospheric density and viscosity structures.

Appendix A: Definition of admittance

Starting with the general linear transfer function between two functions A and B, defined on the surface of the sphere (equation (5)):

$$B(\hat{u}) = \int_{\Omega} F(\hat{u}, \hat{v}) A(\hat{v}) d\Omega. \tag{A1}$$

We assume that the transfer function F is isotropic. Physically, this means that there is no azimuthal bias about the point $\hat{u}$ in the transfer function F, or equivalently, that $B(\hat{u})$ is only dependent on the zonal components of $A(\hat{v})$ about the pole $\hat{u}$. It is also generally assumed that the transfer function is spatially-invariant on the surface of the sphere. Mathematically, these two assumptions mean that F has no explicit dependence on the location $\hat{u}$ depending only on the angular separation between the points $\hat{u}$ and $\hat{v}$, i.e., that $F(\hat{u}, \hat{v}) = F(\hat{u} \cdot \hat{v})$. Substituting this relation into equation (A1) gives a convolution integral [*Basri and Jacobs,* 2003]. These convolution integrals are most conveniently expressed in the spherical harmonic domain.

We adopt the *Varshalovich et al.* [1988] normalization for the spherical harmonic functions:

$$Y_{lm}(\theta, \phi) = (-\text{sgn}(m))^m \sqrt{\frac{(2l+1)}{4\pi} \frac{(l-|m|)!}{(l+|m|)!}} P_{l|m|}(\cos\theta) e^{im\phi}, \tag{A2}$$

$l = 0, 1, 2, \ldots$ and m is an integer such that $-l \leq m \leq l$. P_{lm} are the associated Legendre functions, defined for $m \geq 0$ as:

$$P_{lm}(\cos\theta) = (\sin\theta)^m \frac{d^m}{d(\cos\theta)^m} P_l(\cos\theta) = (-1)^l \frac{(\sin\theta)^m}{2^l l!} \frac{d^{l+m}}{(d\cos\theta)^{l+m}} (\sin\theta)^{2l} \tag{A3}$$

where P_l are Legendre polynomials. These spherical harmonic functions are normalized such that:

$$\int Y_{lm}(\theta,\phi)Y_{l'm'}^*(\theta,\phi)d\Omega = \delta_{ll'}\delta_{mm'} \;. \tag{A4}$$

Continuous functions on the sphere can then be represented by:

$$A(\hat{v}) = A(\theta,\phi) = \sum_{l=0}^{\infty}\sum_{m=-l}^{l}a_{lm}Y_{lm}(\theta,\phi) \;. \tag{A5}$$

The spherical harmonic coefficients a_{lm} of the function $A(\theta,\phi)$ are given by:

$$a_{lm} = \int_{\Omega} A(\theta,\phi)Y_{lm}^*(\theta,\phi)d\Omega \;. \tag{A6}$$

The cross power spectrum between two sets of spherical harmonic coefficients is defined:

$$S_{ab}(l) = \sum_{m=-l}^{l}a_{lm}b_{lm}^* \;. \tag{A7}$$

$S_{aa}(l)$ is termed the power spectrum. The correlation spectrum between two sets of coefficients is defined as:

$$r(l) = \frac{S_{ab}(l)}{\sqrt{S_{aa}(l)S_{bb}(l)}} \;. \tag{A8}$$

Returning to the transfer function (A1), If we choose $\hat{u}$ as the $\theta = 0$ axis, then since F only depends on θ we have the following spherical harmonic representation of the transfer function:

$$F(\hat{u},\hat{v}) = F(\hat{u}\cdot\hat{v}) = F(\cos\theta) = \sum_{l=0}^{\infty}\sqrt{\frac{4\pi}{2l+1}}F_l Y_{l0} = \sum_{l=0}^{\infty}F_l P_l(\cos\theta) \;. \tag{A9}$$

We can now transform equation (A1) using the Funk-Hecke theorem [*Basri and Jacobs*, 2003]:

$$B(\theta,\phi) = B(\hat{u}) = \int_{\Omega} F(\hat{u} \cdot \hat{v})A(\hat{v})d\Omega = \sum_{l=0}^{\infty} F_l \sum_{m=-l}^{l} a_{lm}Y_{lm}(\theta,\phi). \tag{A10}$$

Thus using (A5), replacing A with B and a_{lm} with b_{lm},

$$b_{lm} = F_l a_{lm}. \tag{A11}$$

Our goal is to estimate F_l when b_{lm} and a_{lm} are the spherical harmonic coefficients of the gravity and topography respectively. In general, equation (A11) will not hold for observed gravity and topography due to the presence of "noise" in the gravity. We need to modify equation (A11) to take this into account:

$$g_{lm} = F_l h_{lm} + n_{lm} \tag{A12}$$

where g_{lm} and h_{lm} are the spherical harmonic coefficients of gravity and topography and n_{lm} are the coefficients of the "noise". The "noise" in equation (A12) is defined as the component of the gravity which is uncorrelated with the topography, i.e. the cross power spectrum between the topography and the noise given by equation (A7) is zero for all l. Sources of this noise are not just measurement errors but also include any component of the gravity that cannot be linearly related to the topography. Defining the noise in this way allows us to calculate an estimate of F_l, denoted as $Z(l)$, by multiplying equation (A12) by h_{lm}^* and summing over m yielding equation (6):

$$Z(l) \equiv \frac{S_{gh}(l)}{S_{hh}(l)}.$$

Appendix B: Calculation of model misfit

B1. Tomography, gravity and total misfit

The model misfit parameters used to determine which gravity and topography models best fit observations are based upon a localized version of the residual sum of squares (RSS):

$$\text{RSS}(\Omega) = \frac{1}{4\pi} \int_{\Omega_o} (d(\Omega_o,\Omega) - m(\Omega_o,\Omega))^2 \, d\Omega_o \qquad \text{(B1)}$$

where $d(\Omega_o,\Omega)$ and $m(\Omega_o,\Omega)$ are the data and the model respectively, localized near the location Ω using the spatio-spectral localization method outlined in the text, and defined over the surface of the Earth Ω_o. Using Parseval's theorem [*Wieczorek,* 2007] (B1) is transformed to:

$$\text{RSS}(\Omega) = \sum_{l=0}^{\infty} \sum_{m=-l}^{l} (D_{lm}(\Omega) - M_{lm}(\Omega))^2 \,. \qquad \text{(B2)}$$

In terms of the total cross power between two functions,

$$P_{AB} = \sum_{l=0}^{\infty} \sum_{m=l}^{-l} a_{lm} b_{lm} \,, \qquad \text{(B3)}$$

(B2) becomes:

$$\text{RSS}(\Omega) = P_{DD}(\Omega) + P_{MM}(\Omega) - 2P_{DM}(\Omega), \qquad \text{(B4)}$$

Thus the local residual sum of squares equals the power in the localized data plus the power in the localized model minus twice their cross power. In practice, the sum over l in equation (B3) must be restricted to a finite range of l. We choose to sum the power over the waveband containing the anomalous topography and gravity, namely $10 \leq l \leq 40$, when calculating the model misfit parameters. In order to combine the gravity and topography misfit we normalize (B4) by the localized data power, since the model power varies between models, but the data power does not:

$$\text{RSSN}(\Omega) = \frac{\text{RSS}(\Omega)}{P_{DD}(\Omega)} = 1 + \frac{P_{MM}(\Omega)}{P_{DD}(\Omega)} - 2\frac{P_{DM}(\Omega)}{P_{DD}(\Omega)} \,. \qquad \text{(B5)}$$

RSSN(Ω) will equal 1 for the "null" model, $m(\Omega_o,\Omega) = 0$, and will equal 0 when the data and model match perfectly over our waveband of interest. Combining the gravity and topography normalized misfits is accomplished by averaging:

$$\text{RSSN}(\Omega)_{\text{Total}} = \frac{1}{2}(\text{RSSN}(\Omega)_{\text{Topo}} + \text{RSSN}(\Omega)_{\text{Grav}}) . \tag{B6}$$

Throughout this paper we use equations (B5) and (B6) to calculate model misfit when the data and model are localized near the center of the Congo basin at $\Omega = (22.00°\text{E}, 1.75°\text{S})$.

A similar process is used to calculate the misfit of the localized admittance (7). This misfit is based upon the root-mean-square residual of model and observed admittance over a specified waveband:

$$R_A(\Omega) = \sqrt{\frac{\sum\limits_{l=l_{\min}}^{l=l_{\max}}(Z_o(l,\Omega) - Z_m(l,\Omega))^2}{l_{\max} - l_{\min}}} . \tag{B7}$$

We restrict the sum in equation (B7) to the waveband $20 \leq l \leq 40$ over which the observed admittance is anomalously high. We also normalize (B7) by the residual for the "null" model giving:

$$RN_A(\Omega) = \sqrt{\frac{\sum\limits_{l=l_{\min}}^{l=l_{\max}}(Z_o(l,\Omega) - Z_m(l,\Omega))^2}{\sum\limits_{l=l_{\min}}^{l=l_{\max}}(Z_o(l,\Omega))^2}} . \tag{B8}$$

The admittance misfit is only used to identify which models give admittance values similar to those observed and is not included in the total misfit calculation since it is not an independent measure of model misfit.

B2. Tomography misfit

S20RTS is parameterized in terms of spherical harmonic functions and 21 radial basis splines, defined on the domain $R_{CMB} < r < R_E$:

$$\delta V_S(r,\theta,\phi) = \sum_{k=1}^{21} \sum_{l=0}^{20} \sum_{m=-l}^{l} v_{klm} Z_k(r) Y_{lm}(\theta,\phi) \tag{B9}$$

where δV_s is shear-wave velocity anomaly relative to PREM, and Z_r are the splines. Using the procedures of *Ritsema et al.* [2007] we project our input models onto this basis and then apply the S20RTS resolution filter to obtain the coefficients of the synthetic velocity anomaly, s_{klm}. We calculate the local correlation coefficient between the synthetic and S20RTS for each spline using [*Toksöz et al.*, 1969]:

$$c_k(\Omega) = \frac{\displaystyle\sum_{l=0}^{20}\sum_{m=-l}^{l} v_{klm}(\Omega) s_{klm}(\Omega)}{\sqrt{\displaystyle\sum_{l=0}^{20}\sum_{m=-l}^{l} v_{klm}^2(\Omega) \sum_{l=0}^{20}\sum_{m=-l}^{l} s_{klm}^2(\Omega)}} \tag{B10}$$

where $v_{klm}(\Omega)$ and $s_{klm}(\Omega)$ are the coefficients of S20RTS and the synthetic tomography respectively, after being localized near the Congo basin. The coefficients c_k provide a representation of the localized correlation as a function of depth:

$$c(r,\Omega) = \sum_{k=1}^{21} c_k(\Omega) Z_k(r). \tag{B11}$$

We calculate a weighted average of this correlation function using a weighting function, $g(r)$, whose support is the uppermost mantle (depth < 1000 km) and whose amplitude is constant throughout $r < 800$ km (Figure B1):

$$C = \frac{\displaystyle\int_{R_{CMB}}^{R_E} g(r) c(r,\Omega) dr}{\displaystyle\int_{R_{CMB}}^{R_E} g(r) dr} = \frac{\displaystyle\sum_{k=1}^{21} g_k c_k(\Omega)}{\displaystyle\sum_{k=1}^{21} g_k} \tag{B12}$$

where g_k are the coefficients of the filter g in the spline basis. C is a measure of the correlation between the synthetic tomography and S20RTS localized near the Congo and to a depth less than 1000 km.

References

Anderson, D. L. (2007), The eclogite engine: Chemical geodynamics as a Galileo thermometer, *in* Foulger, G. R. and Jurdy, D. M. eds., *Plates, Plumes and Planetary Processes: Geological Society of America Special Paper*, *430*, 47-64, doi:10.1130/2007.2430(03).

Atalay, A. (2002), Active compressional tectonics in central Africa and implications for plate tectonic models: Evidence from fault mechanism studies of the 1998 earthquakes in the Congo basin, *Journal of African Earth Sciences*, *35*, 45-50.

Basri, R. and D. W. Jacobs (2003), Lambertian reflectance and linear subspaces. *IEEE Transactions on Pattern Analysis and Machine Intelligence*, *25*, 218-233.

Billen, M. I., M. Gurnis and M. Simons (2003), Multiscale dynamics of the Tonga-Kermadec subduction zone, *Geophysical Journal International*, *153*, 359-388.

Burke, K. (1976), The Chad basin: An active intra-continental basin, *Tectonophysics*, *36*, 197-206.

Cahen, L. (1954), *Géologie du Congo Belge*, H. Vaillant-Carmanne, Liège.

Cahen, L., J. J. Ferrand, M. J. F. Haarsma, L. Lepersonne and Th. Verbeek, (1959), Description du sondage de Samba, *Annales du Musée royale du Congo belge, in-8°, Sciences géologiques, vol. 29*.

Cahen, L., J. J. Ferrand, M. J. F. Haarsma, L. Lepersonne and Th. Verbeek, (1960), Description du sondage de Dekese, *Annales du Musée royale du Congo belge, in-8°, Sciences géologiques, vol. 34*.

Conrad, C. P. and P. Molnar (1999), Convective instability of a boundary layer with temperature- and strain-rate-dependent viscosity in terms of 'available buoyancy', *Geophysical Journal International*, *139*, 51-68.

CGMW/Unesco (1987), International Geological Map of Africa 1/500000, 6 panels, CGWM/Unesco, Paris, France.

Daly, M. C., S. R. Lawrence, D. Kumin'a and M. Binga (1991), Late Paleozoic deformation in Africa: a result of distant collision? *Nature*, *350*, 605-607.

Daly, M. C., S. R. Lawrence, K. Diemu-Tshiband and B. Matouana (1992), Tectonic evolution of the Cuvette Centrale, Zaire, *Journal of the Geological Society of London*, *149*, 539-546.

DeRito, R. F., F. A. Cozzarelli, and D. S. Hodge (1983), Mechanism of subsidence of ancient cratonic rift basins, *Tectonophysics*, 94, 141-168.

D'Errico, J. (2005), *Surface fitting using gridfit*, available from MATLAB® Central at: http://www.mathworks.com/matlabcentral .

De Waele, B., Johnson, S. P., and S. A. Pisarevsky (2008), Paleoproterozoic to Neoproterozoic growth and evolution of the eastern Congo Craton: Its role in the Rodinia puzzle, *Precambrian Research*, *160*, 127-141, doi:10.1016/j.precamres.2007.04.020.

Dziewonski, A. M. and D. L. Anderson (1981) Preliminary reference Earth model, *Physics of the Earth and Planetary Interiors*, *25*, 297-356.

Évrard, P., (1957), Les recherches géophysiques at géologiques et le travaux de sondage dans la Cuvette congolaise, *Mémoires Académie royale des Sciences colonials, Classe des Sciences Techniques, in-8°, Tome VII, fasc. 1*.

Farr, T. G., et al. (2007), The Shuttle Radar Topography Mission, *Reviews of Geophysics*, *45*, RG2004, doi:10.1029/2005RG000183.

Fishwick, S. (2007), Seismic studies of the African continent and a new surface wave model of the uppermost mantle, *Mémoires Géosciences Rennes, hors série n°7,* 17-21.

Giresse, P., (2005), Mesozoic-Cenozoic history of the Congo basin, *Journal of African Earth Sciences*, *43*, 302-315, doi:10.1016/j.jafrearsci.2005.07.009.

Grand, S. P., (2002), Mantle shear-wave tomography and the fate of subducted slabs, *Philosophical Transactions of the Royal Society of London A*, *360*, 2475-2491.

Gu, Y. J., A. M. Dziewonski, W. Su and G. Ekström (2001), Models of the mantle shear velocity and discontinuities in the pattern of lateral heterogeneities, *Journal of Geophysical Research*, *106*, 11169-11199.

Hartley, R. W., and P. A. Allen, (1994), Interior cratonic basins of Africa: Relation to continental break-up and role of mantle convection, *Basin Research*, *6*, 95-113.

Hartley, R. W., A. B. Watts, and J. D. Fairhead, (1996), Isostasy of Africa, *Earth and Planetary Science Letters*, *137*, 1-18.

Hirth, G. and D. Kohlstedt (2003), Rheology of the upper mantle and the mantle wedge: A view from the experimentalists, in *Inside the Subduction Factory*, *Geophysical Monograph 138*, edited by J. Eiler, pp. 83-105, AGU, Washington, D. C., doi:10.1029/138GM06.

Ingersoll, R. V., and C. J. Busby (1995), Tectonics of sedimentary basins, in *Tectonics of Sedimentary Basins*, edited by C. J. Busby and R. V. Ingersoll, pp. 1-51, Blackwell, Boston.

Jordan, T. H. (1978), Composition and development of the continental tectosphere, *Nature*, *274*, 544-548.

Kaminsky, E. and C. Jaupart (2000), Lithospheric structure beneath the Phanerozoic intracratonic basins of North America, *Earth and Planetary Science Letters*, *178*, 139-149.

Karato, S. (2008), *Deformation of Earth Materials: An Introduction to the Rheology of Solid Earth*, Cambridge University Press, Cambridge, UK.

Kaus, B. J. P., J. A. D. Connolly, Y. Y. Podladchikov and S. M. Schmalholz, (2005), Effect of mineral phase transitions on sedimentary basin subsidence and uplift, *Earth and Planetary Science Letters*, *233*, 213-228, doi:10.1016/j.epsl.2005.01.032.

Kelly, R. K., P. B. Kelemen and M. Jull (2003) Buoyancy of the continental upper mantle, *Geochemistry, Geophysics, Geosystems*, *4(2)*, *1017*, doi:10.1029/2002GC000399.

Leighton, M. W., and D. R. Kolata (1990), Selected interior cratonic basins and their place in the scheme of global tectonics, in *Interior Cratonic Basins: American Association of Petroleum Geologists Memoir*, *51*, edited by M. W. Leighton, et al., pp.729-797, AAPG, Tulsa.

McGovern, P. J., S. C. Solomon, D. E. Smith, M. T. Zuber, M. Simons, M. A. Wieczorek, R. J. Phillips, G. A. Neumann, O. Aharonson and J. W. Head (2004), Localozed gravity/topography admittance and correlation spectra on Mars: Implications for regional and global evolution, *Journal of Geophysical Research*, *107*(E12), 5136, doi:10.1029/2002JE001854.

McKenzie, D. (2003), Estimating T_e in the presence of internal loads, *Journal of Geophysical Research*, *108*, 2438, doi:10.1029/2002JB001766.

McKenzie, D. and D. Fairhead, (1997), Estimates of the effective elastic thickness of the continental lithosphere from Bouguer and free air gravity anomalies, *Journal of Geophysical Research*, *102*, 27523-27552.

McNutt, M. (1979), Compensation of oceanic topography: An application of the response function technique to the *Surveyor* area. *Journal of Geophysical Research*, *84*, 7589-7598.

Mégnin, C. and B. Romanowicz (2000), The three-dimensional shear velocity structure of the mantle from the inversion of body, surface and higher-mode waveforms, *Geophysical Journal International*, *143*, 709-728.

Middleton, M. F. (1989), A model for the formation of intracratonic sag basins, *Geophysical Journal International*, *99*, 665-676.

Naimark, B. M. and A. T. Ismail-Zadeh (1995), Numerical models of a subsidence mechanism in intracratonic basins: application to North American basins, *Geophysical Journal International*, *123*, 149-160.

O'Connell, R. J. and G. J. Wasserburg (1972), Dynamics of submergence and uplift of a sedimentary basin underlain by a phase-change boundary, *Reviews of Geophysics and Space Physics*, *10*, 335-368.

Pasyanos, M. E. and A. A. Nyblade (2007), A top to bottom lithospheric study of Africa and Arabia, *Tectonophysics*, *444*, 27-44, doi:10.1016/j.tecto.2007.07.008.

Priestly, K. and D. McKenzie (2006), The thermal structure of the lithosphere from shear wave velocities, *Earth and Planetary Science Letters*, *244*, 285-301, doi:10.1016/j.epsl.2006.01.008.

Ritsema, J. and H. J. van Heijst (2000), New seismic model of the upper mantle beneath Africa, *Geology*, *28*, 63-66.

Ritsema, J. and H. J. van Heijst (2004), Global transition zone tomography, *Journal of Geophysical Research*, *109*, B02302, doi:10.1029/2003JB002610

Ritsema, J., H. J. van Heijst, and J. H. Woodhouse (1999), Complex shear wave velocity anomaly structure imaged beneath Africa and Iceland, *Science*, *286*, 1925-1928.

Ritsema, J., A. K. McNamara, and A. L. Bull (2007), Tomographic filtering of geodynamic models: Implications for model interpretation and large-scale mantle structure, *Journal of Geiphysical Research*, *112*, B01303, doi:10.1029/2006JB004566.

Simons, M. (1996), Localization of Gravity and Topography: Constraints on the Tectonics and Mantle Dynamics of Earth and Venus, Ph. D. thesis, Massachusetts Institute of Technology, Cambridge, MA.

Simons, M., S. Solomon and B. H. Hager (1997), Localization of gravity and topography: Constraints on the tectonics and mantle dynamics of Venus, *Geophysical Journal International*, *131,* 24-44.

Sleep, N. H. (2005), Evolution of the continental lithosphere, *Annual Review of Earth and Planetary Science*, *33*, 369-393, doi:10.1146/annurev.earth.33.092203.122643.

Sloss, L. L. (1988), Tectonic evolution of the craton in Phanerozoic time, in *Sedimentary Cover—North American Craton: U.S., The Geology of North America, vol. D-2*, edited by L. L. Sloss, pp. 25-51, The Geological Society of America, Boulder.

Sloss, L. L. (1990), Epilog, in *Interior Cratonic Basins: American Association of Petroleum Geologists Memoir*, *51*, edited by M. W. Leighton, et al., pp.729-797, AAPG, Tulsa.

Tan, E. and M. Gurnis (2007), Compressible thermochemical convection and application to lower mantle structures, *Journal of Geophysical Research*, *112*, B06034, doi:10.1029/2006JB004505.

Tapley, B., J. Ries, S. Bettadpur, D. Chambers, M. Cheng, F. Condi, B. Gunter, Z. Kang, P.Nagel, R. Pastor, T. Pekker, S.Poole, and F. Wang, (2005), GGM02—An improved Earth gravity field model from GRACE, *Journal of Geodesy*, *79*, 467-478, doi:10.1007/s00190-005-0480-z.

Turcotte, D. L., R. J. Willemann, W. F. Haxby and J. Norberry (1981), Role of membrane stresses in support of planetary topography, *Journal of Geophysical Research*, *68*, 3951-1724.

Varshalovich, D. A., A. N. Moskalev, and V. R. Kjersonskii (1998) *Quantum Theory of Angular Momentum*, World Scientific, Singapore.

Watts, A. B. and W. B. F. Ryan (1976), Flexure of the lithosphere and continental margin basins, *Tectonophysics*, *36*, 25-44.

Wieczorek, M. A. (2007) The gravity and topography of the terrestrial planets, *Treatise on Geophysics*, *vol. 10*, edited by T. Spohn, series editor G. Schubert, 165-206, doi:10.1016/B978-044452748-6.00156-5.

Tables:

Table 1: Parameters used in flexure calculations

Variable Name	Symbol	Value
Crustal Thickness	T_C	35 km
Earth Radius	R_E	6371 km
Topographic Density Contrast	$\Delta\rho_H$	2670 kg/m^3
Moho Density Contrast	$\Delta\rho_M$	630 kg/m^3
Gravitational Acceleration	g	9.81 m/s^2
Young's Modulus	E	100 GPa
Poisson's Ratio	ν	0.25

Table 2: Parameters used in viscous models

Variable Name	Symbol	Value
Reference Density	ρ_o	3300 kg/m^3
Temperature Change Across Model	ΔT	1300 K
Themal Diffusivity	κ	1×10^{-6} m^2/s
Coefficient of Thermal Expansion	α	2×10^{-5} K^{-1}
Reference Viscosity	η_o	5×10^{20} Pas
Rayleigh Number	Ra	4.35×10^8

Table 3: Summary of model groups

| | | Group Parameters | | | | | Best Fit Model From Each Group | | | | | |
Group	v_T	η_{eqv} Depth (km)	Mass Anomaly (10^{18} kg)	Z_{lm} (km)	r_{lm}	Model	Anomaly Depth (km)	Half-Thickness (km)	Gravity Misfit	Topography Misfit	Total Misfit	$\Delta\rho_{max}$ (kg/m^3)
1	4.35	0	9	-	1	I806	100	50	0.398	0.686	0.542	54
2	4.35	50	8	-	1	I790	100	100	0.395	0.681	**0.538**	27
3	4.35	50	9	-	1	I546	100	100	0.381	0.682	**0.532**	30
4	4.35	50	10	-	1	I506	100	50	0.378	0.695	**0.537**	60
5	4.35	50	14.7	-	1	I763	50	50	0.376	0.900	0.638	100
6	4.35	100	9	-	1	I832	100	100	0.385	0.682	**0.534**	30
7	0.1	50	8	-	1	I895	100	100	0.387	0.680	**0.534**	27
8	0.1	50	9	-	1	I848	100	50	0.381	0.684	**0.533**	54
9	0.1	50	10	-	1	I530	100	50	0.387	0.699	0.543	60
10	-0.9	50	10	-	1	I489	50	50	0.401	0.702	0.552	68
11	10	50	9	-	1	I874	100	100	0.383	0.682	**0.533**	30
12	4.35	50	6	-	1	I924	200	50	0.386	0.714	0.550	36
13	4.35	50	14.7	500	50	I718	300	50	0.409	0.689	0.549	93
14	4.35	50	14.7	400	20	I742	300	50	0.419	0.704	0.561	93
15	-0.9	50	9	-	1	I944	100	50	0.389	0.686	**0.538**	54

Figure 1: Basemap showing the SRTM topography of Africa. The major features discussed in the text are labeled. Note the nearly circular depression of the Congo basin. The white box outlines the location of Figures 6 and 8. The south African escarpments are labeled: DE = Drakensberg Escarpment, GE = Great Escarpment and BE = Gamsberg Escarpment.
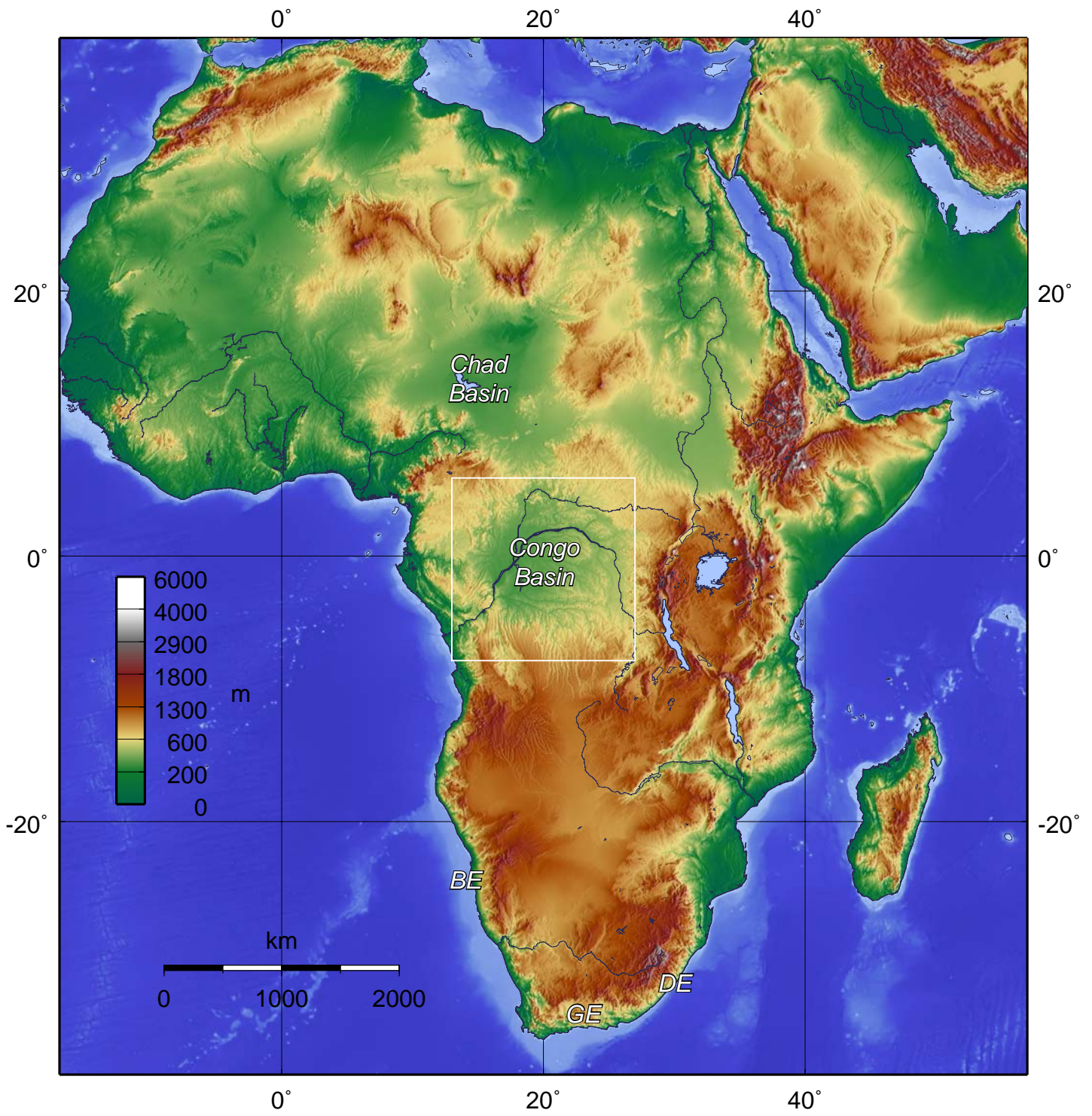
Figure 2: **a)** Free-air gravity anomaly (GGM02S from GRACE) expanded to $L_{max} = 110$. Note the prominent low coincident with the Congo basin. **b)** Geoid heights from GGM02S. The Congo basin is coincident with an embayment in the high-amplitude, long-wavelength Indian geoid low. Contour interval is 5 m, with the zero contour as a thick line. **c)** Filtered free-air anomaly (GGM02S) using a trapezoidal band pass filter (l = 5-10-45-60). **d)** Same as c) except the field was filtered using the conjugate band reject filter: c) and d) represent a decomposition of the field in a). Note that the gravity low associated with the Congo is contained within the waveband of anomalously high RMS amplitude highlighted in Figure 3a.

a) GRACE Gravity
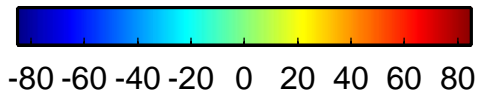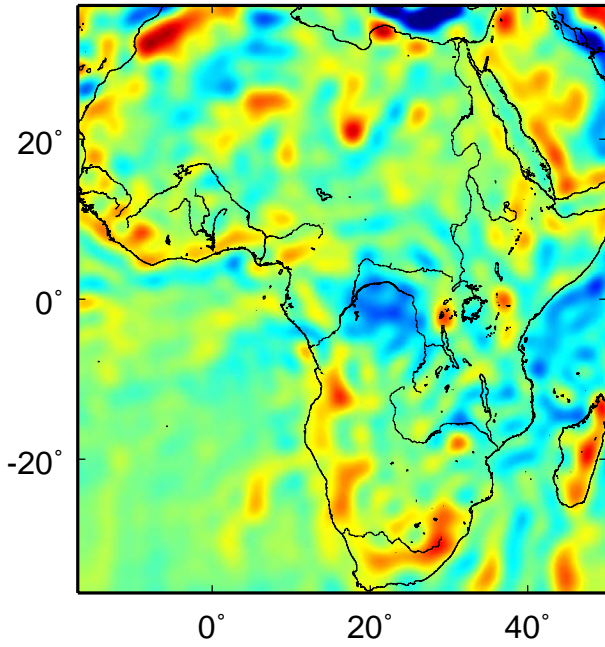
b) GRACE Geoid

Free Air Gravity (mGal)
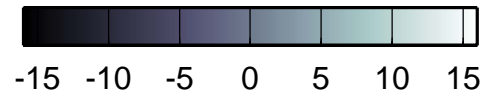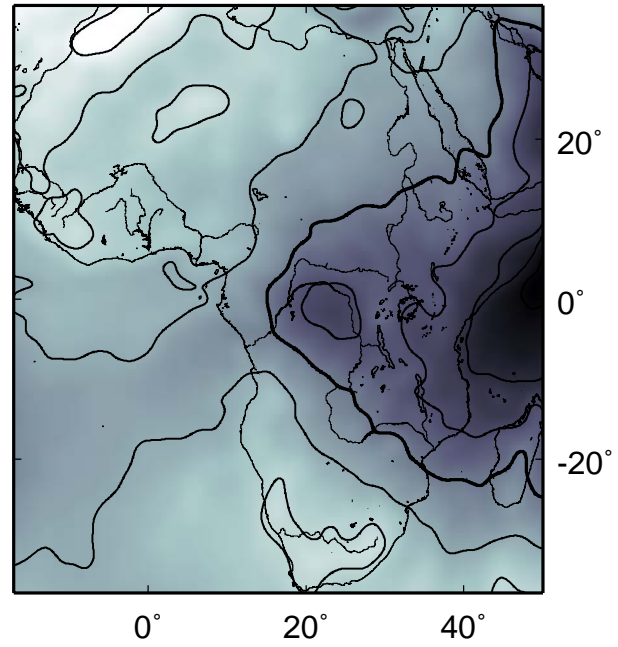
Geoid Height (m)

c) Band-Passed Gravity
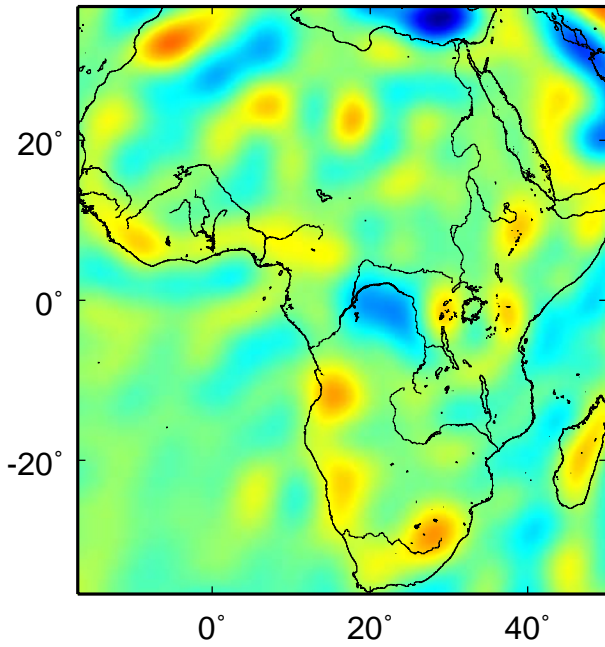
d) Band-Rejected Gravity
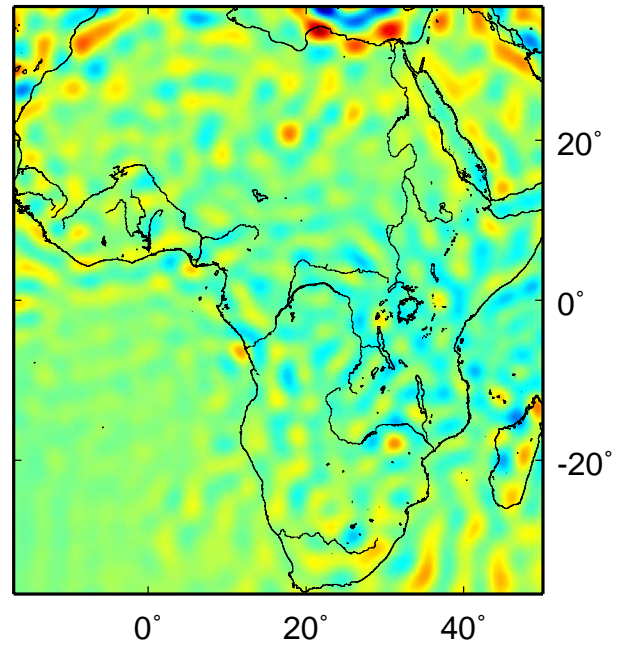
Figure 3: **a)** Anomalous RMS amplitude spectrum of the GGM02S free-air gravity anomaly localized near the center of the Congo basin at 22.0°E, 1.75°S. The amplitude of the gravity anomaly near the Congo is particularly large within the waveband $10 < l < 45$. **b)** Same as a) except that the RMS amplitude anomaly of the topography has been localized near the Congo: topography before the removal of the anomalous Mesozoic-Quaternary isopach (solid line); anomalous RMS amplitude of the topography after correction for sediment removal (dashed line). Note that there are two wavebands over which the topography of the Congo is anomalous. For the waveband $5 < l < 15$, the large amplitudes result from the spectral expression of the continent-ocean boundary, while the anomalous amplitudes within the waveband $15 < l < 45$ result from the topographic expression of the Congo basin. Sedimentation within the basin has preferentially dampened the topography within the waveband $15 < l < 65$, with uniform damping over $20 < l < 50$.

a) RMS Gravity Anomaly

b) RMS Topography Anomaly

Original Topography

Sediment Corrected
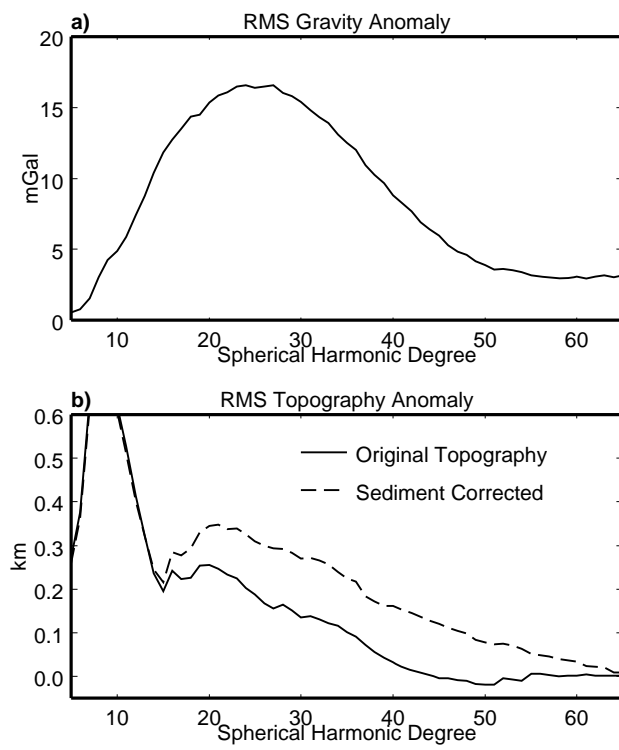
Figure 4: a) Topography of Africa expanded out to $L_{max} = 110$. The Congo basin has only a slight topographic expression. **b)** Topography of Africa after the removal and unloading of the anomalous Mesozoic-Quaternary sedimentary infill of the Congo basin. Removal of these sediments highlights the structure of the Congo's anomalous topography which is nearly circular in shape. **c) & d)** Similar to the free-air anomaly of the Congo, this unloaded topography is also band limited as shown by decomposing the topography using an $l = 10$-15-45-60 trapezoidal band pass and conjugate band reject filter.

a) Topography

b) Sediment-Unloaded Topo

c) Band-Passed Unloaded Topo

d) Band-Rejected Unloaded Topo

Elevation (km)
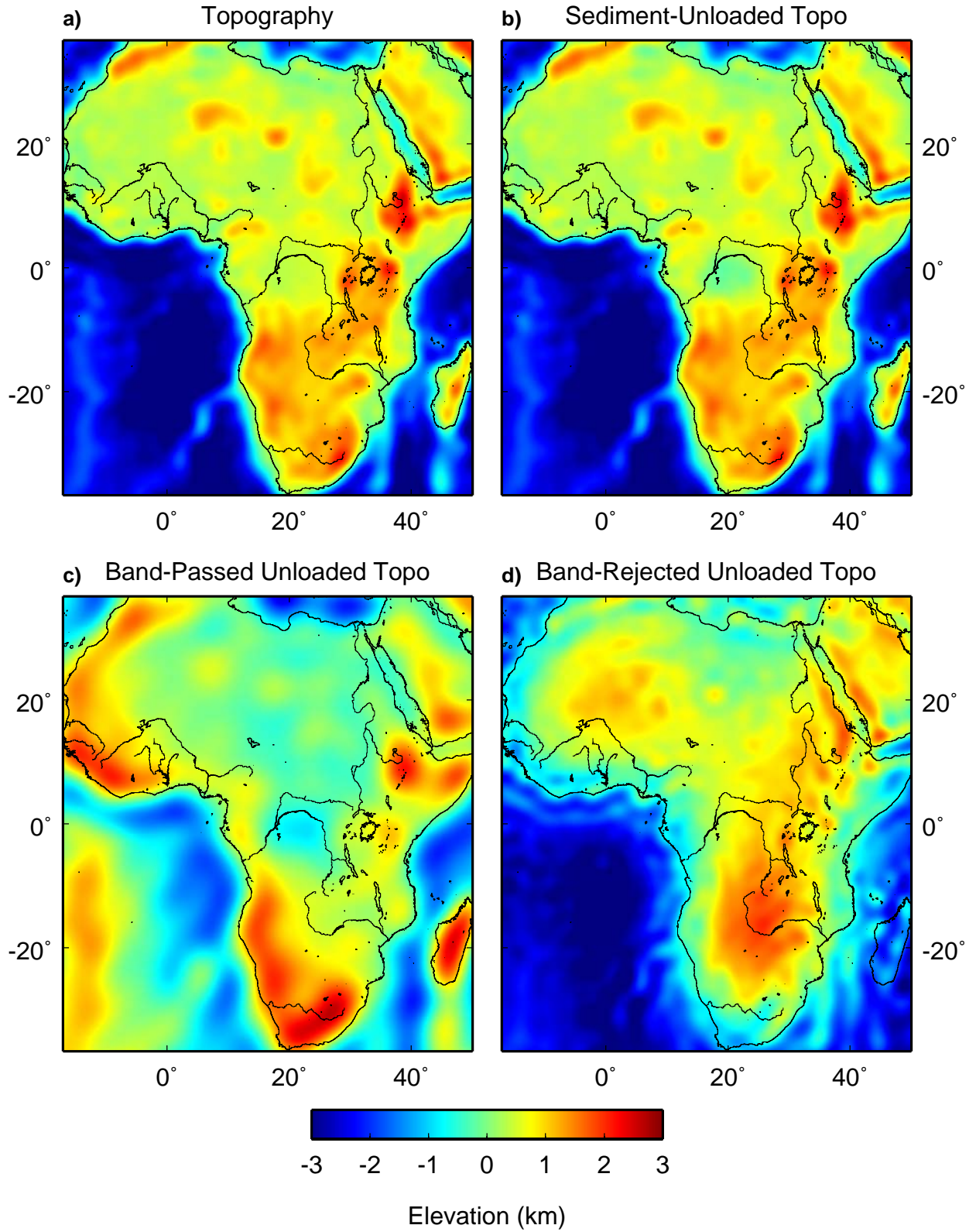
Figure 5: a) Estimated admittance of the Congo basin localized near 22.00°E, 1.75°S (solid line with error bars), along with the localized correlation coefficient (thick line). The dashed lines are model admittances calculated assuming flexural support of a topographic load using the values listed in Table 1 and are labeled with the magnitude, in km, of the elastic thickness. The admittance of the Congo region is consistent with unreasonably large values of elastic thickness, indicating that the topography near the Congo is not maintained by lithospheric flexure. **b)** Same as a) except that the sediment unloaded topography has been used in the admittance estimate.
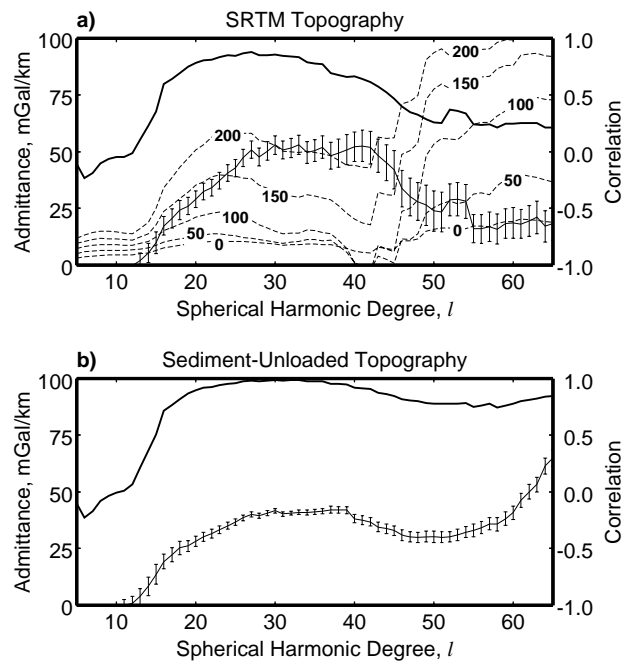
Figure 6: Contours of the Mesozoic-Quaternary sedimentary rocks (thin black lines; thickness labeled in m). See Figure 1 for location; the Congo and Ubangui rivers are shown as gray lines for reference. These sedimentary units are identified by *Daly et al.* [1992] as having no explainable subsidence mechanism. The location of thickest sediment infill is coincident with the location of the Congo gravity anomaly (Figure 2). The thick black lines and well symbols denote the locations of the seismic sections and wells used in the construction of this map. The wells are designated DEKESE (D), SAMBA (S) and Gilson (G). Velocities determined by refraction surveys near the location of the SAMBA well were used for time-depth conversion of the seismic data [*Évrard*, 1957].

Mesozoic-Cenozoic Isopach in metres
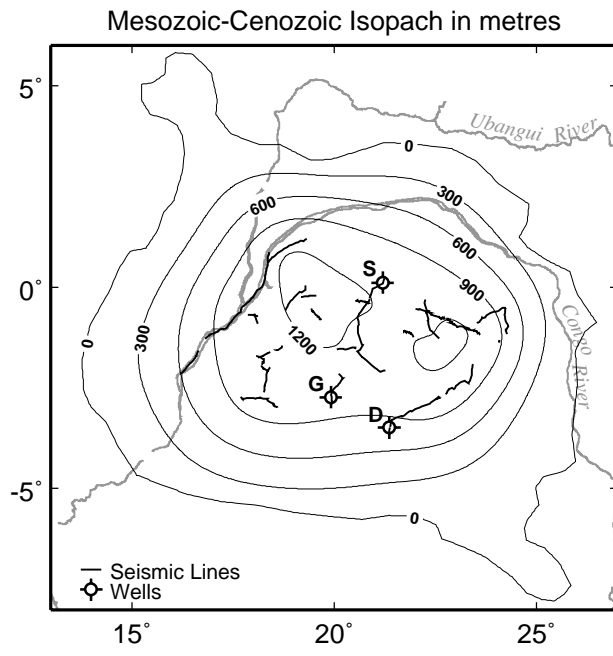
Figure 7: a) Depth slice through the tomography model S20RTS [*Ritsema et al.*, 1999; *Ritsema and van Heijst*, 2004] at a depth of 150 km. Note the +5% shear-wave velocity anomaly (relative to PREM) beneath the Congo basin which forms a maxima distinct from the fast regions beneath southern Africa. **b)** Same as a) but at a depth of 300 km. At this depth the Congo velocity anomaly has magnitude +1%. **c)** NE-SW cross section through S20RTS along the profile A-A'. **d)** Same as c), however the cross section trends NW-SE along profile B-B'. These two cross-sections highlight the depth extent of the Congo basin velocity anomaly. The maximum anomaly of +5% occurs near a depth of 100-150 km. This anomaly decays with depth to +2% over the depth range 150-300 km. From 300 km to 800 km depth the velocity anomaly is relatively constant at 1%, reaching 0% near 800 km deep.

a) Depth = 150 km

b) Depth = 300 km

Shear-Wave Velocity Anomaly Relative to PREM (%)

c)

d)
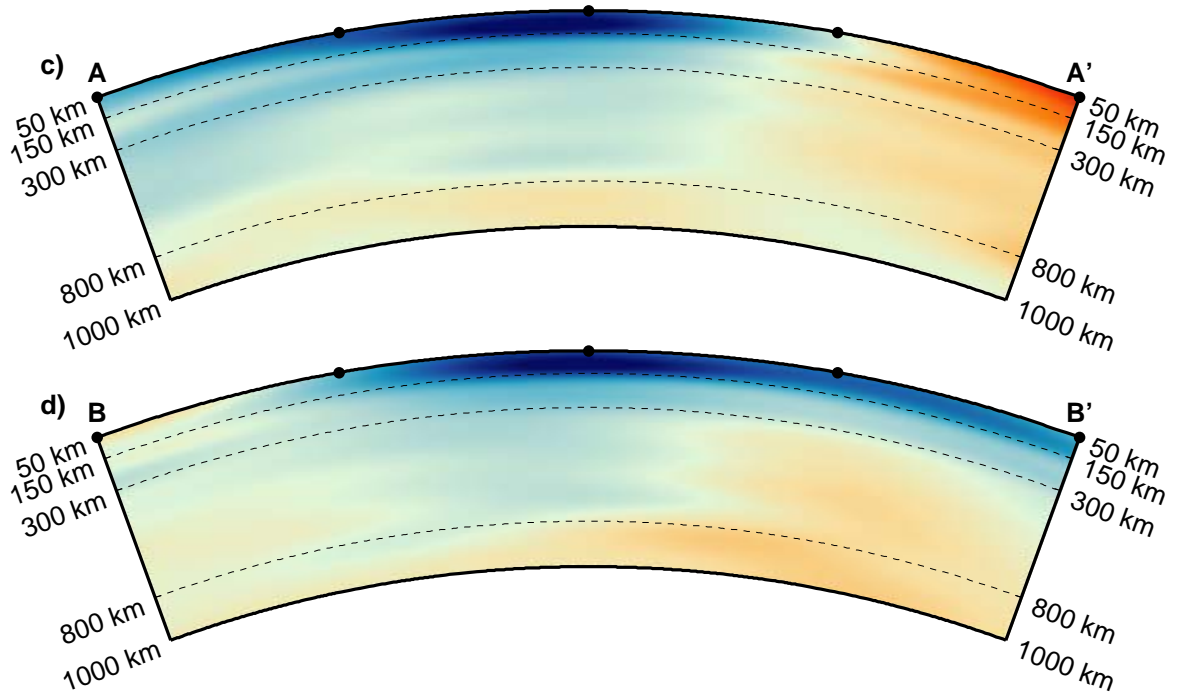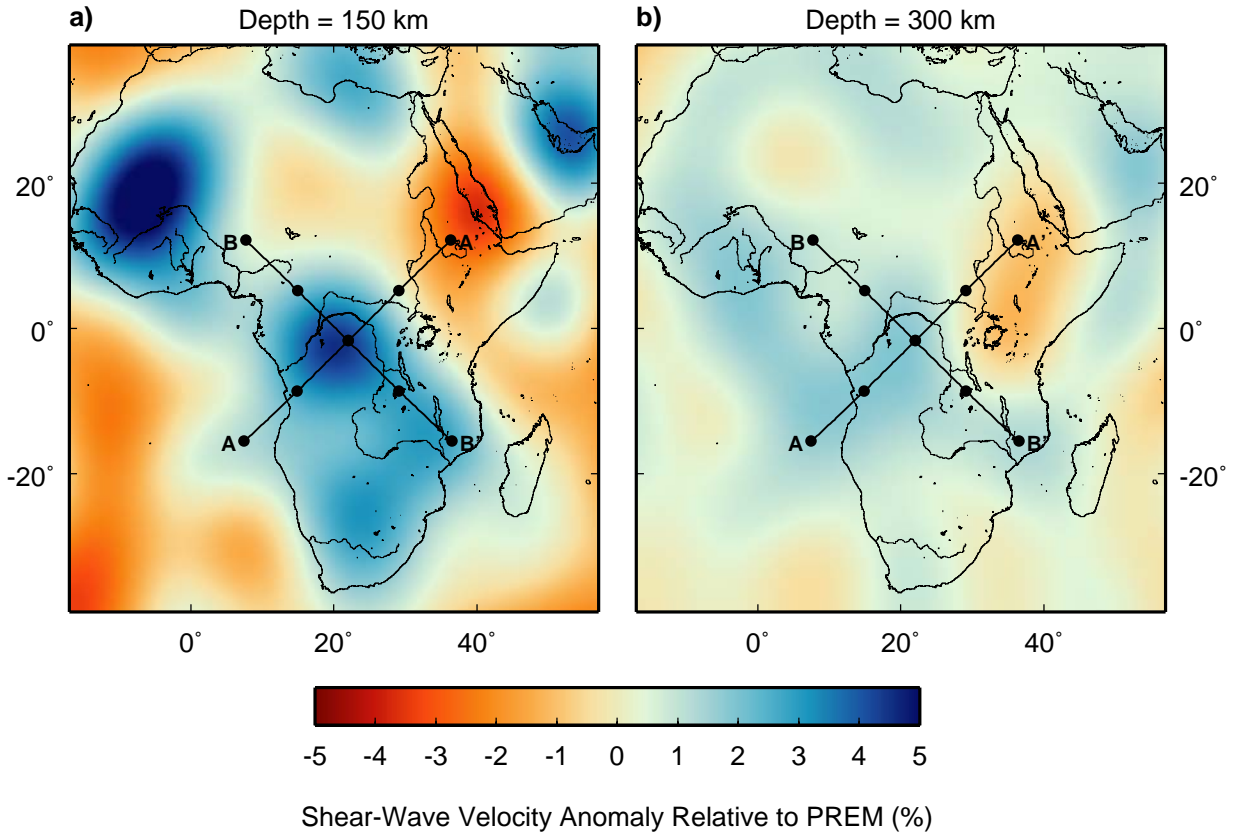
Figure 8: 3-D view of our finite-element mesh viewed from the southeast. The gridlines have been decimated by a factor of six for clarity. The domain extends from the CMB to the surface, spans 80° longitude by 80° latitude and straddles the equator. The total number of nodes in each dimension is 217. The central 34° by 34° region has a grid spacing of 0.2° increasing linearly outside this region to 2.75° at the edge of the domain. In depth the grid spacing is 7 km over the uppermost 700 km of the mantle and increases linearly below to 40 km spacing at the CMB.
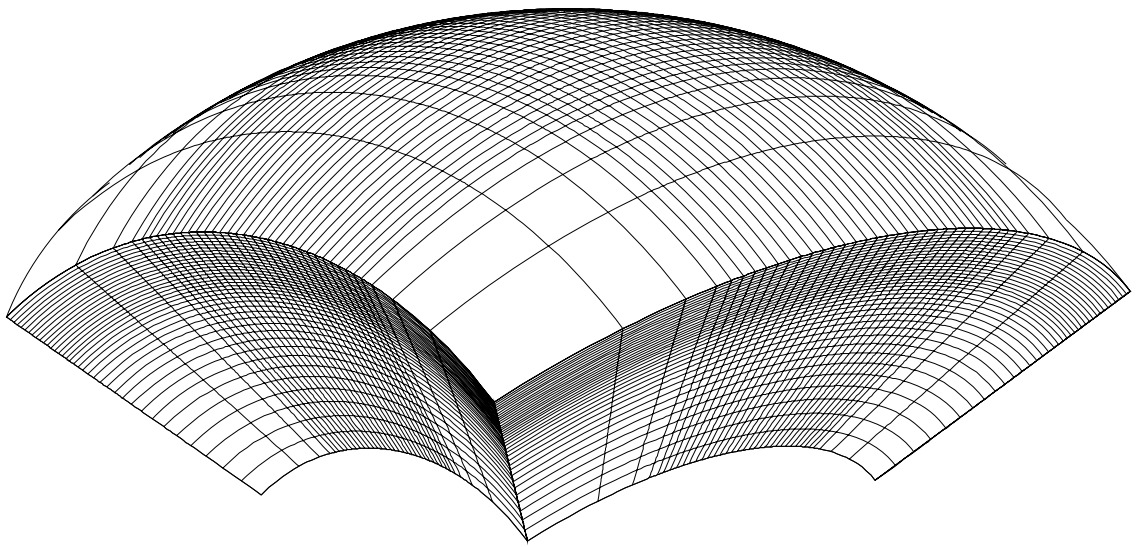
Figure 9: Cross-sections through the center of a sample input model with half-width = 600 km, half-depth = 100 km, depth = 100 km, $r = 1000$, $v_T = 4.35$ and total anomalous mass = $9{\times}10^{18}$ kg. **a)** Input density structure. The maximum density anomaly is +27 kg/m^3. **b)** Background viscosity structure. **c)** Viscosity anomaly associated with the density anomaly in a). The value of the background viscosity structure at a depth of 50 km defines the maximum viscosity of the anomaly. **d)** The total viscosity structure is defined as max($\eta_{background}$, $\eta_{anomaly}$). Defining the viscosity in this manner allows the anomalous mass to be viscously coupled to the lithosphere smoothly and without increasing the viscosity within the lithosphere.

a)

Density Anomaly(kg/m³)

b)

log(Background Viscosity (Pas))

c)

log(Anomaly Viscosity (PaS))

d)

log(Viscosity (Pas))
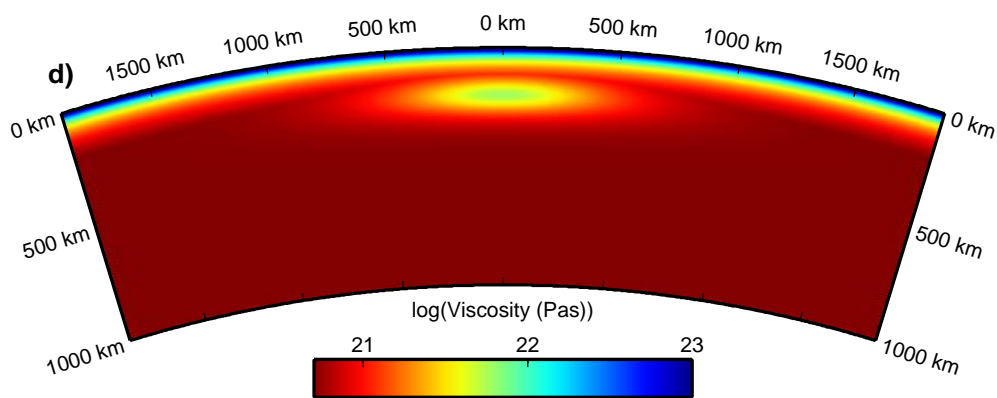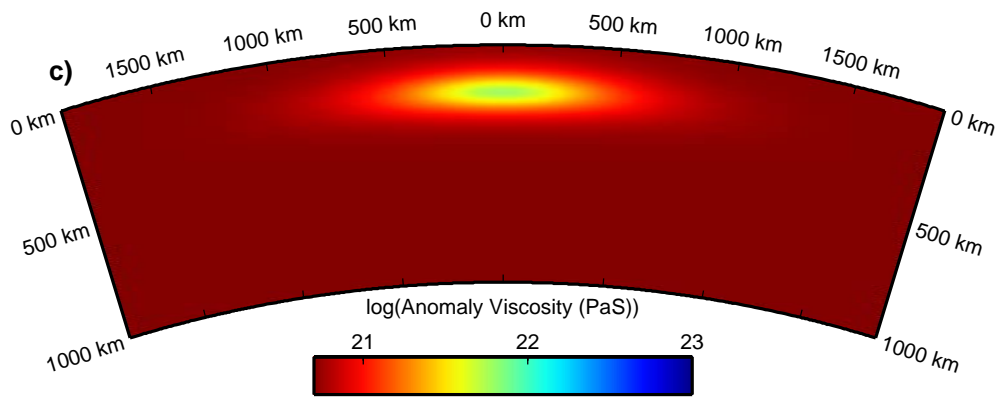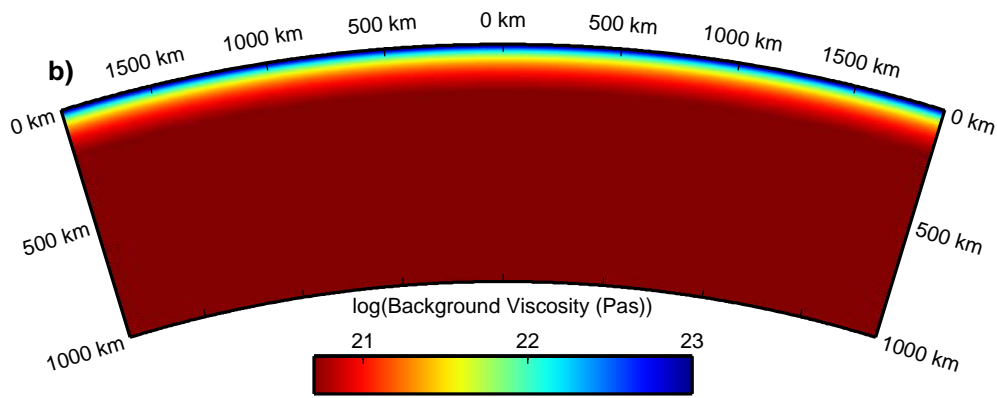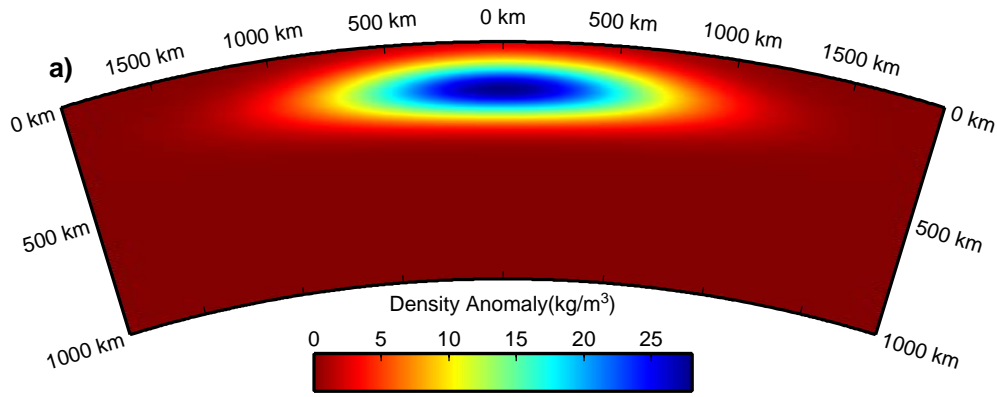
Figure 10: Viscosity as a function of f for various values of v_T and $r = 1000$. For the background viscosity, f equals the ratio of depth to lithospheric thickness. This viscosity profile is nearly linear with f for $v_T = -0.9$, nearly exponential for $v_T = 0.1$ and super-exponential for $v_T = 4.35$ and 10.
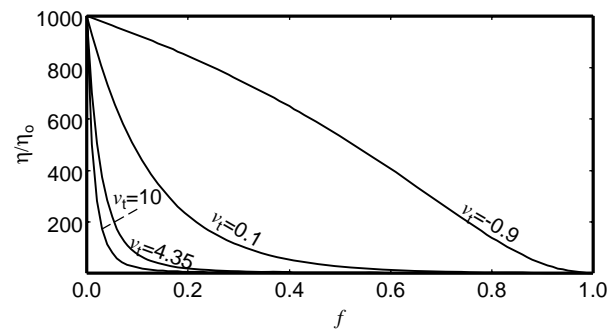
Figure 11: Model topography for several groups presented in Table 3. In all cases the total mass anomaly is 9×10^{18} kg and the lower mantle is isoviscous. The symbol size indicates goodness of fit with observations with a larger symbol meaning a better fit (See Appensix B). The color of each symbol displays the maximum topographic depression observed at the center of the Congo basin. These models all have an isoviscous lower mantle. Other viscosity parameters are: **a)** Group 3, η_{eqv} depth = 50 km, v_T = 4.35. **b)** Group 8, η_{eqv} depth = 50 km, v_T = 0.1. **c)** Group 6, η_{eqv} depth = 100 km, v_T = 4.35. **d)** Group 1, η_{eqv} depth = 0 km, v_T = 4.35. See text for a detailed discussion of these models.
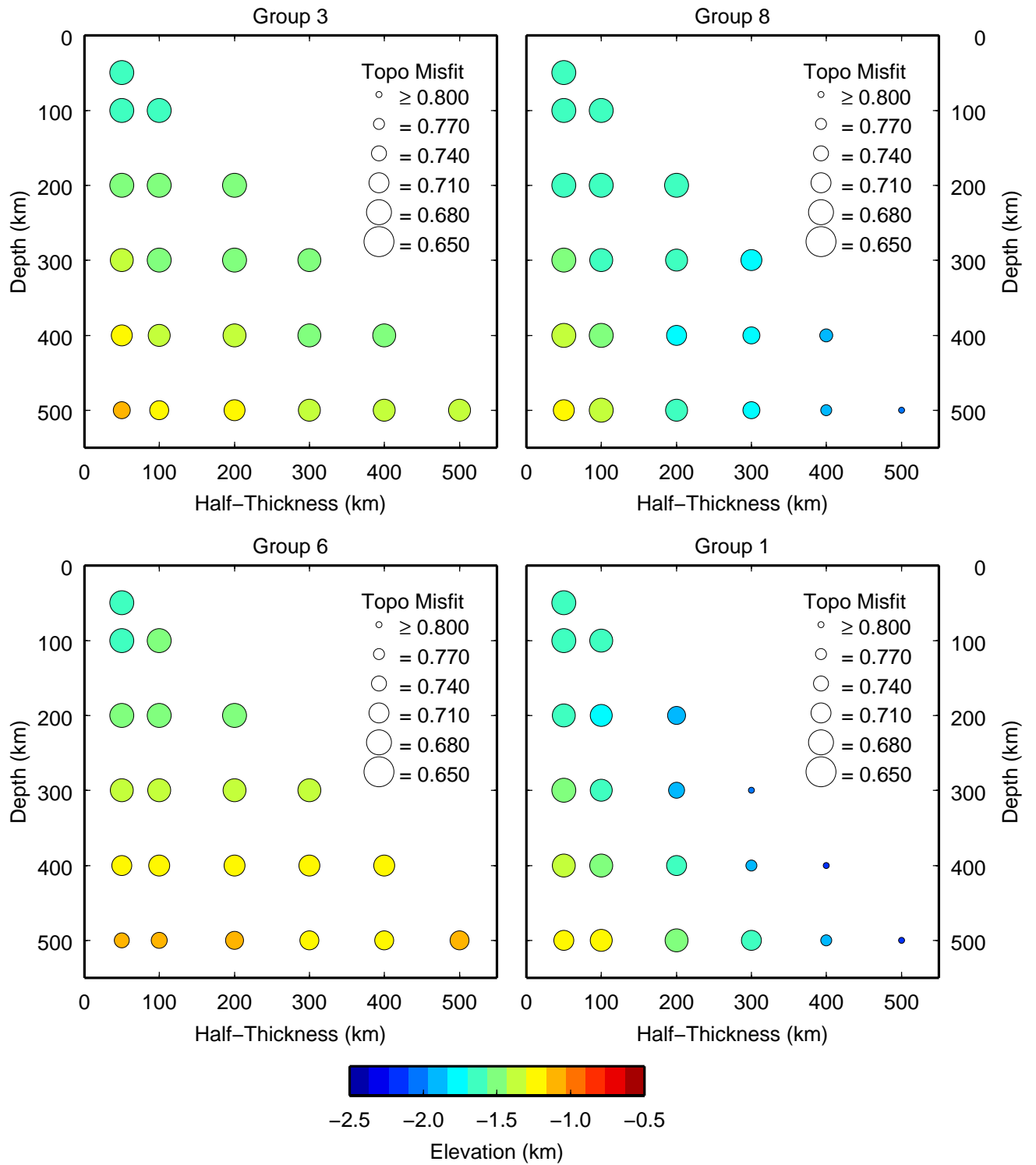
Figure 12: Magnitude of topographic deflection for models with different background viscosity profiles. All cases have the same mass anomaly of 9×10^{18} kg and half-thickness of 50 km. The topographic depression is nearly the same for all viscosity profiles at a depth of 50 km; however the depression for models whose profile is super-exponential ($v_T = 4.35$ and 10) decays more quickly with depth than the models with a near exponential viscosity profile ($v_T = 0.1$).
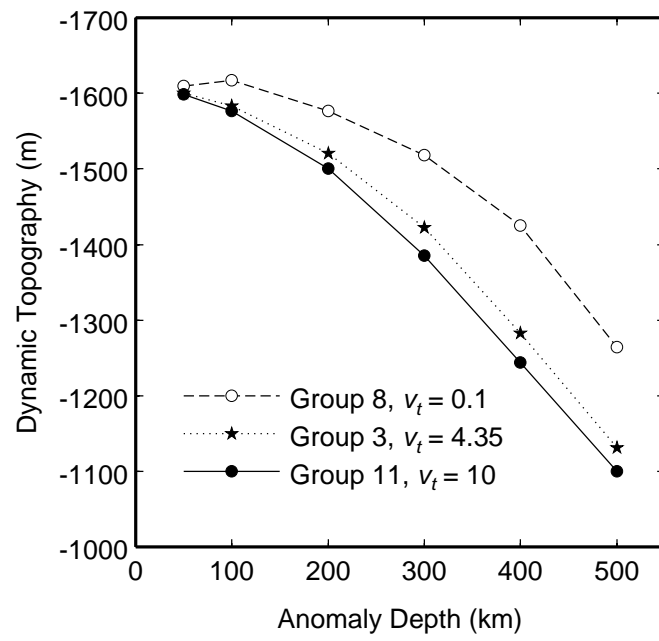
Figure 13: Profiles of model topography along a north-south transect through the Congo basin at 22°E. The profiles here are for models in group 1. These models all have a relatively high viscosity associated with the density anomaly. **a)** Group 1 models whose half-thickness is 50 km for various depths (the model at 50 km depth has been left out for clarity: it is very similar to the profile for the model at 100 km depth). The magnitude of the depression for these models decreases as the anomaly gets deeper, while the width remains relatively constant. **b)** Group 1 models whose depth is 400 km. Thicker anomalies are more strongly coupled to the surface so the magnitude of the depression for these models increases with anomaly thickness. Note however that there is also a significant narrowing of the depression for the models whose anomaly is thickest. The red curve in a) and b) are for the same model and provides a reference shape.

a) Group 1, Constant Half-thickness = 50 km

b) Group 1, Constant Depth = 400 km
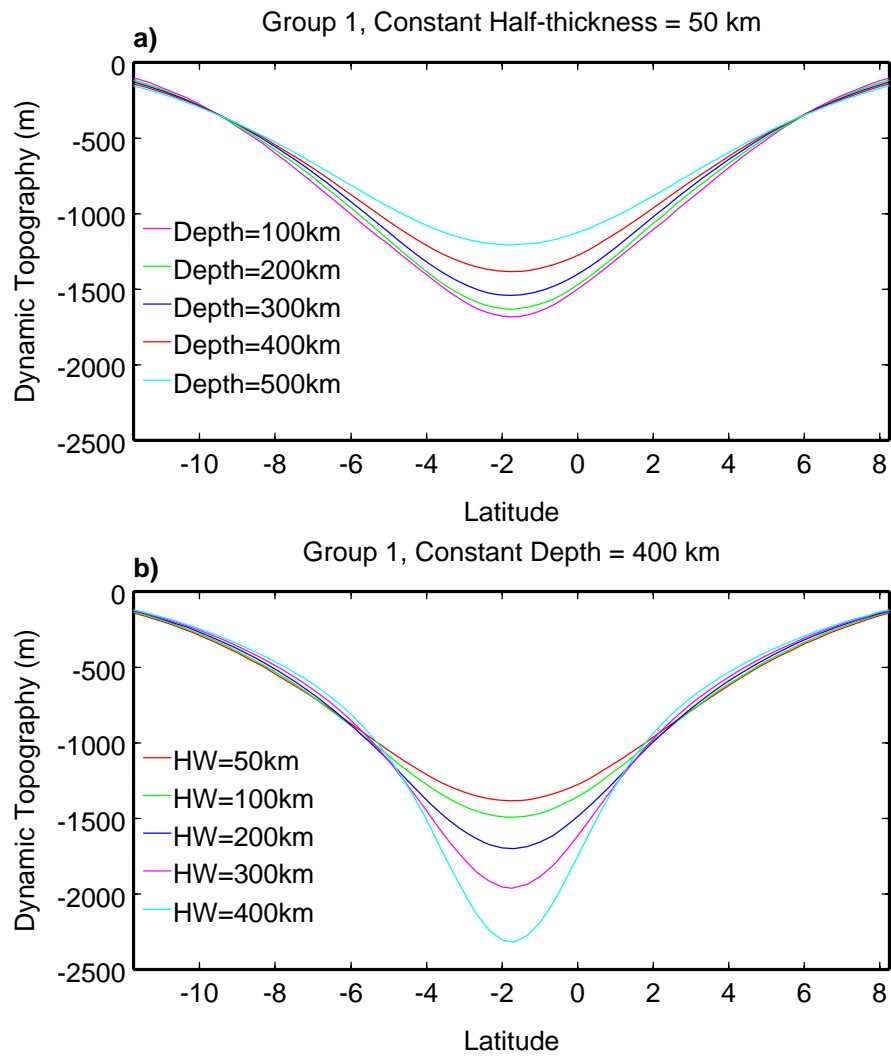
Figure 14: Same as Figure 11, except symbol size represents gravity misfit and symbol color represents total gravity anomaly at the center of the Congo basin.
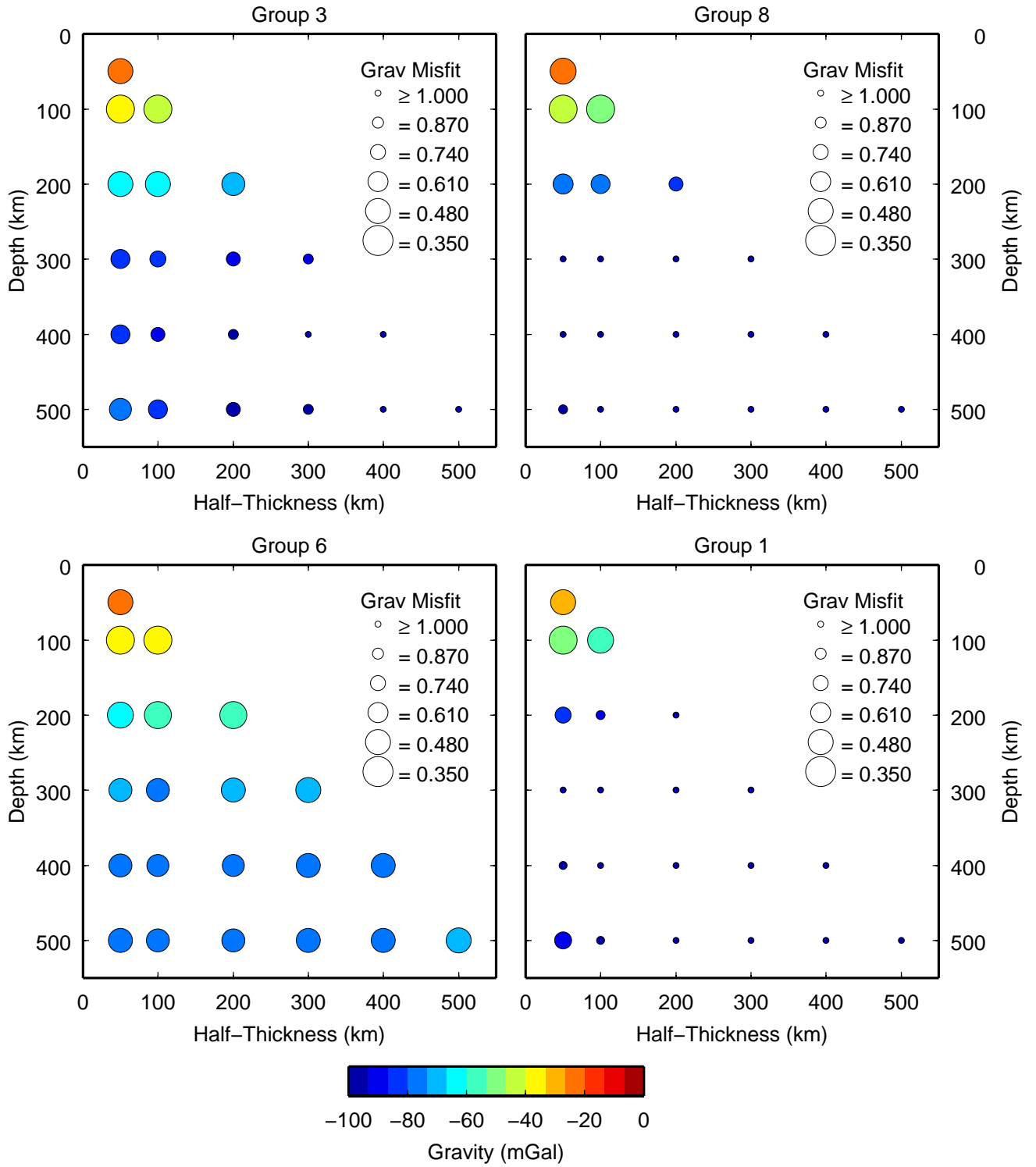
Figure 15: Same as Figure 11, except symbol size represents admittance misfit and symbol color represents average admittance observed over the band $20 < l < 40$ when gravity and topography are localized near the center of the Congo basin.
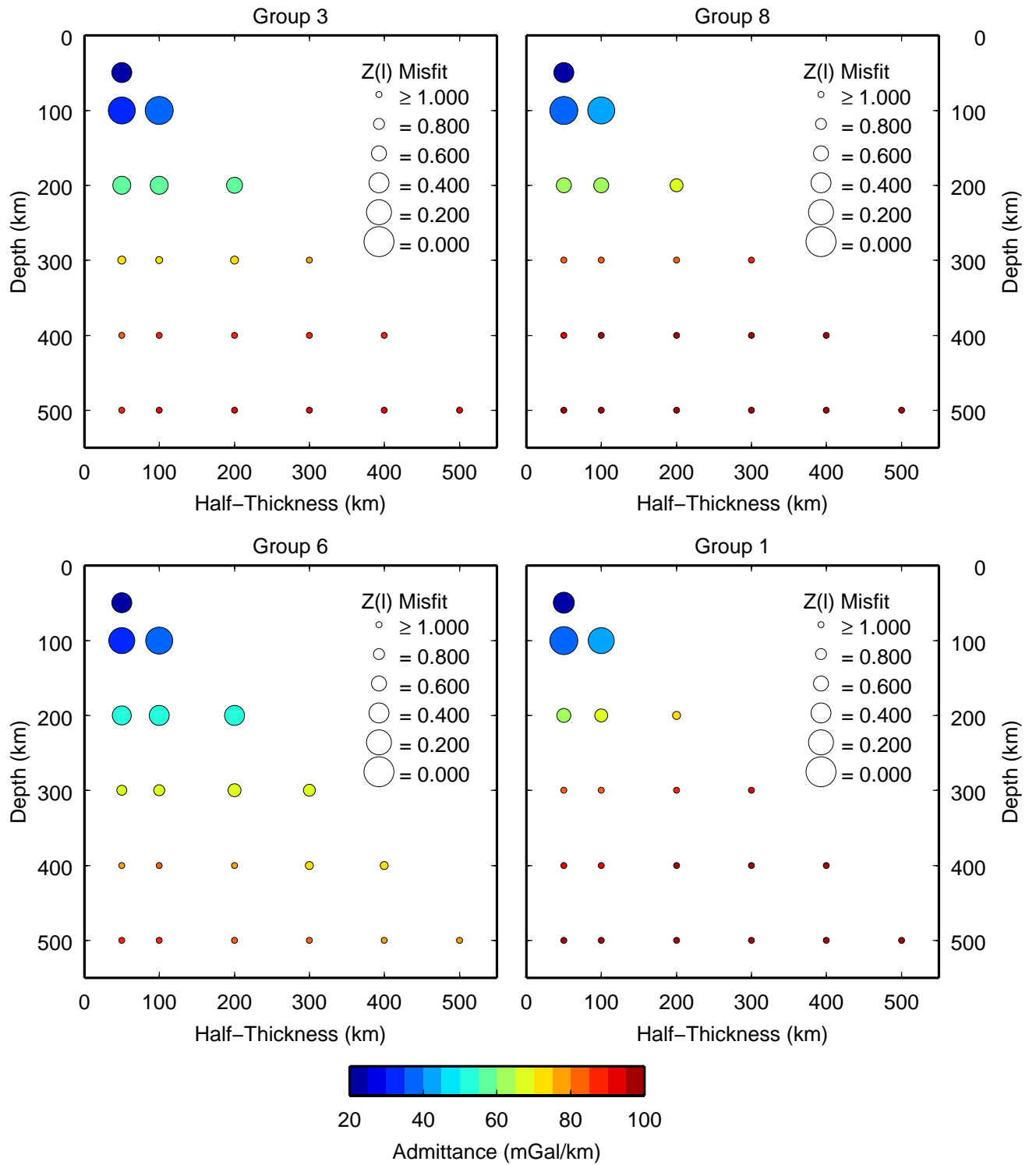
Figure 16: Same as Figure 11, except symbol size represents total misfit.
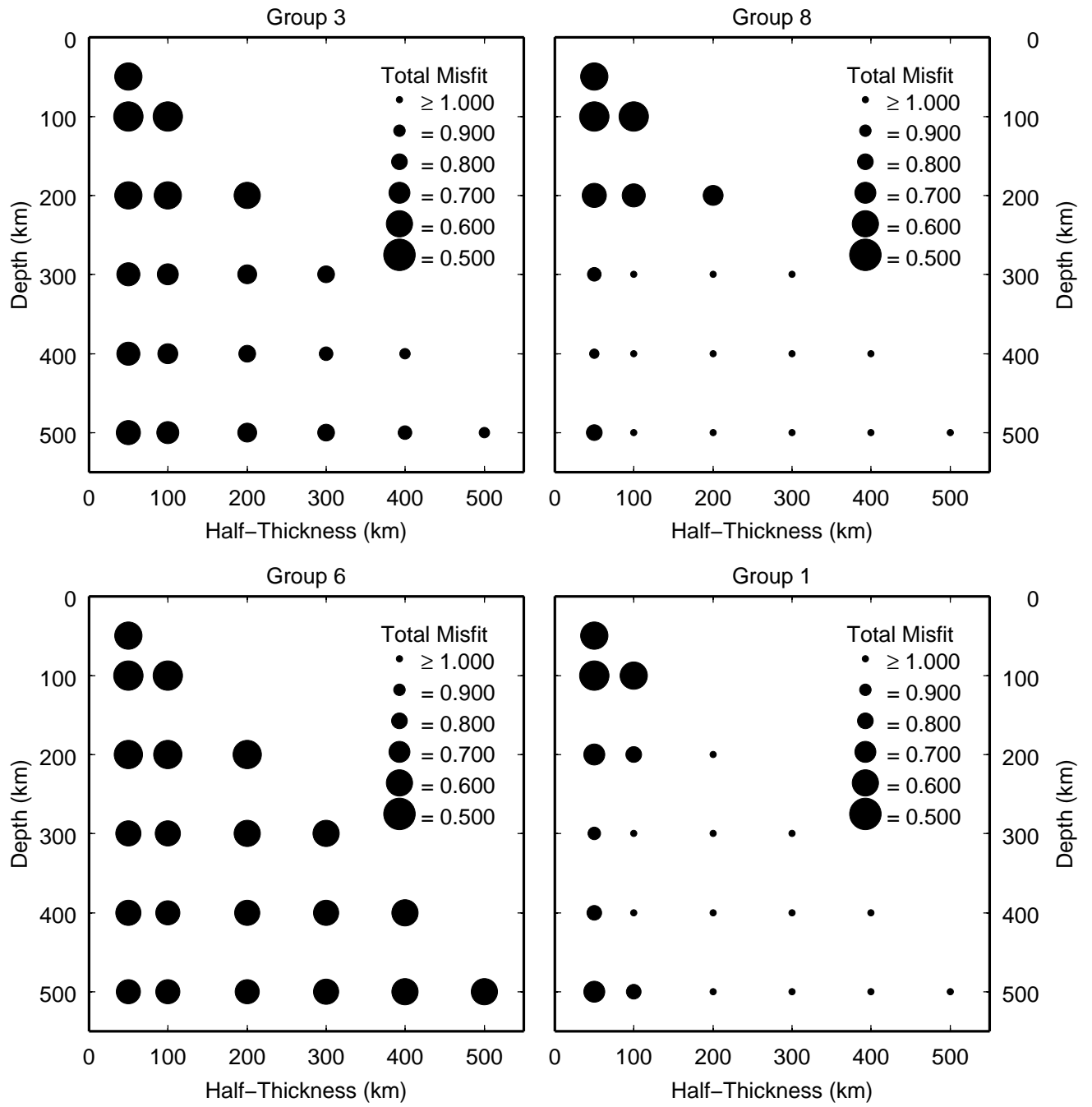
Figure 17: Sample model output for our overall best-fitting model (model I546; Table 3). **a)** Model topography reaches maximum amplitude of about 1.4 km near the center of the Congo basin. **b)** Residual topography calculated by subtracting the model in a) from the sediment-corrected topography displayed in Figure 4b. The absence of any significant depression at the location of the Congo basin demonstrates the very good fit to observations we are able to achieve with our dynamic models. **c)** Model gravity for our best-fit model. This model gravity reaches -70 mGal minimum magnitude at the center of the Congo basin. **d)** Residual gravity given by subtracting the model gravity from the GRACE gravity shown in Figure 2a. Again, there is no systematic misfit observed in the Congo region indicating a good fit. Overall we are able to fit the gravity and topography of the Congo basin using several models whose output is similar to those described here (see Table 3).
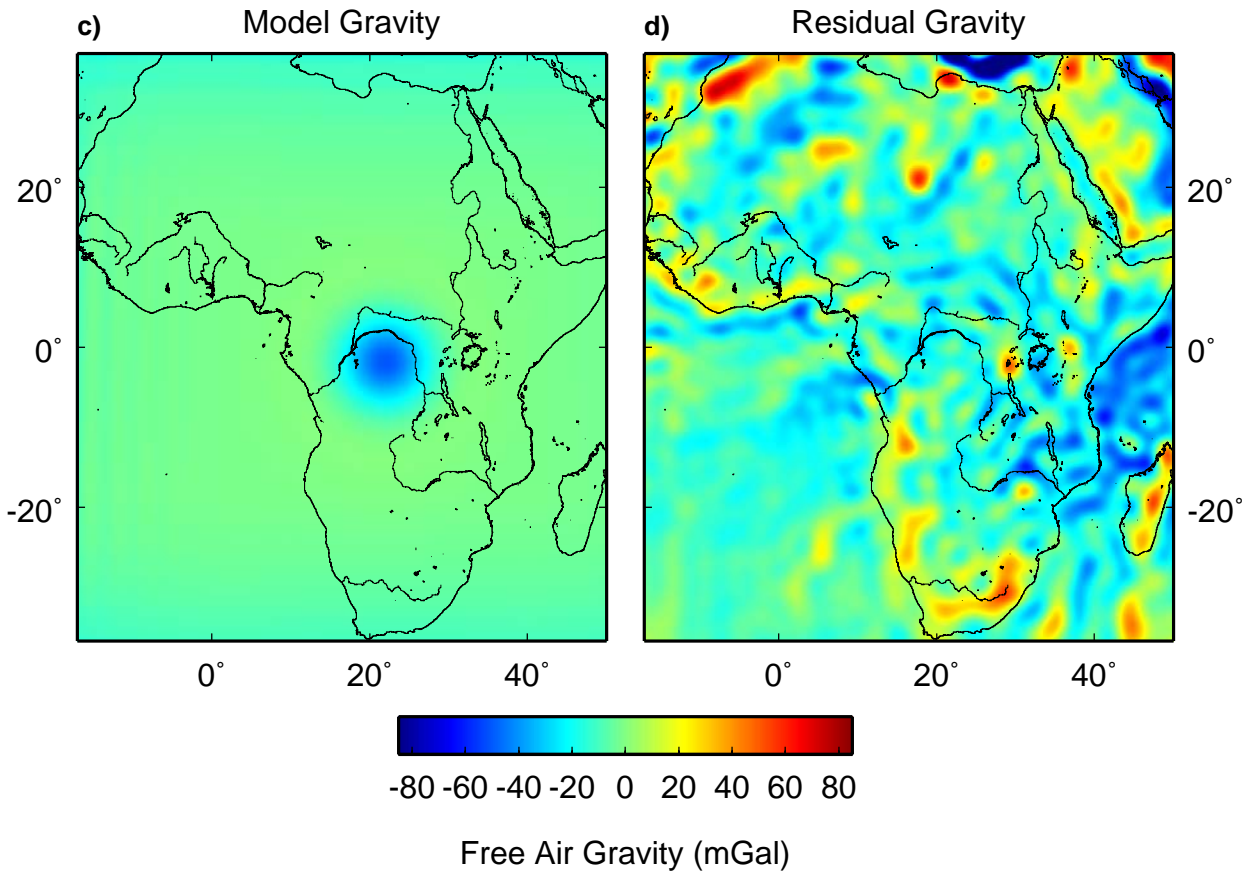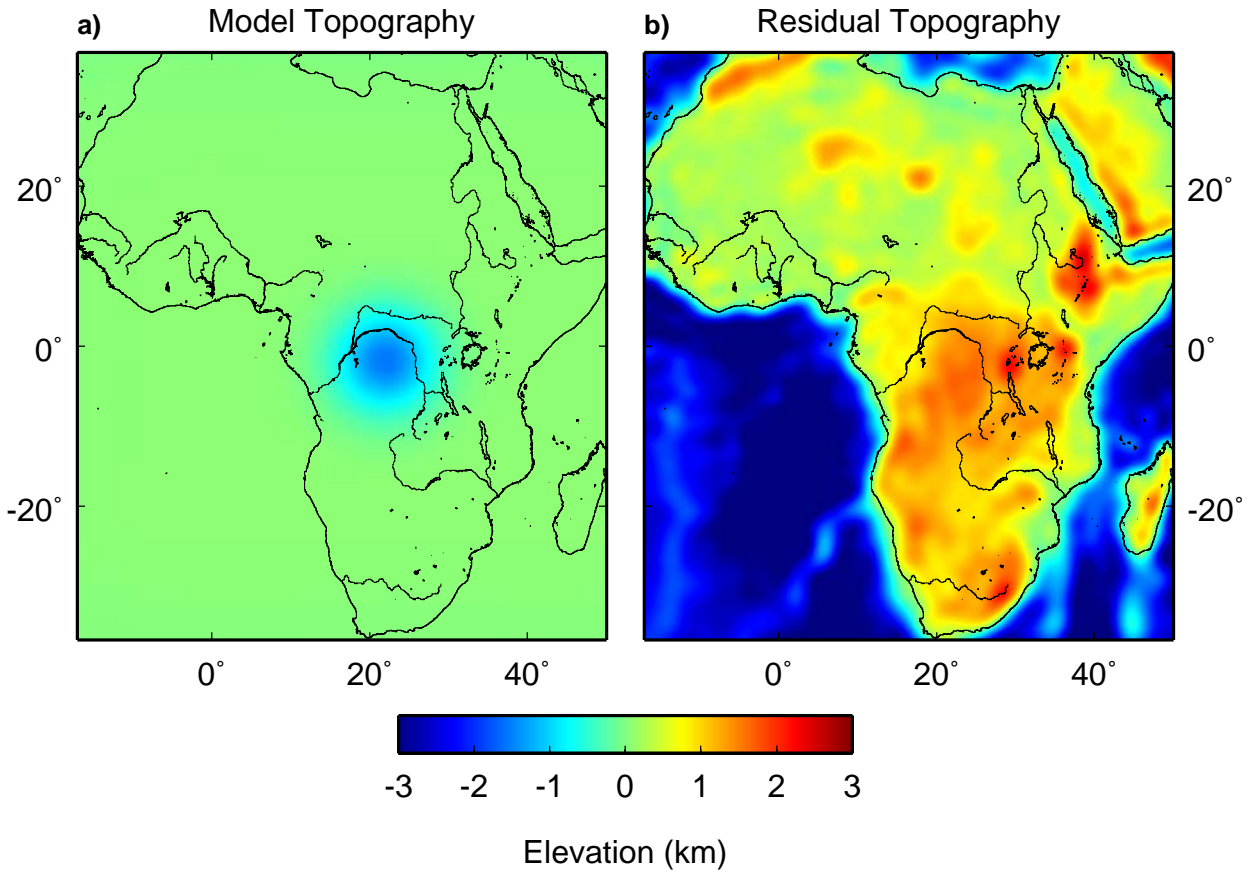
a) Model Topography

b) Residual Topography

Elevation (km)

c) Model Gravity

d) Residual Gravity

Free Air Gravity (mGal)

Figure 18: a) Bandpassed topographic profile of our best-fit model, I546, along with the sediment unloaded topography ("Observation") and the original SRTM topography ("Surface") at longitude 22°E. The model fits the data the best near the center of the Congo basin. The large southward increase in the observed topography south of the basin is the high elevations of southern Africa. **b)** Model power "spectrogram" along the profile in a). Each vertical slice of this image represents the power spectrum of the model in a) localized near the latitudes along the profile. Note that the model power is localized near the Congo basin. **c)** Spectrogram of the "observed" profile in a). Note the anomalous RMS topography near the Congo, superimposed upon a triangular-shaped region of high topography power in southern Africa. **d)** Localized residual sum of squares (RSS) for model I546 (see Appendix B). The localized RSS is equivalent to the data power minus the model power, so it is equal to the image in c) minus the image in b). Note that much of the anomalous power associated with the Congo basin has been removed.
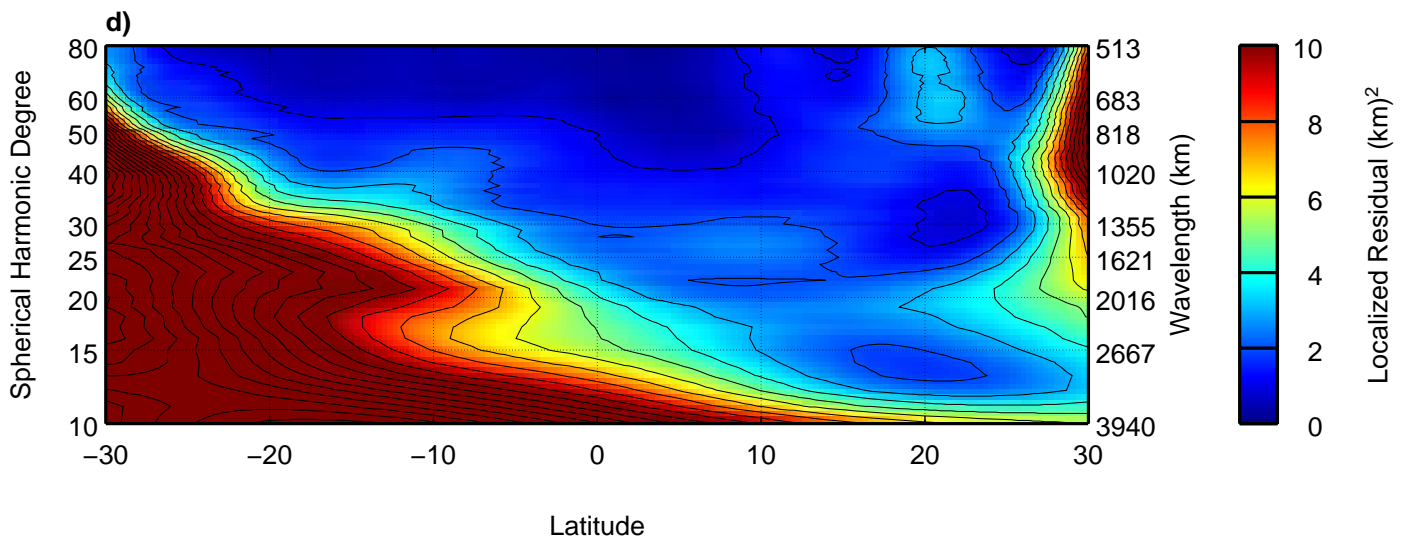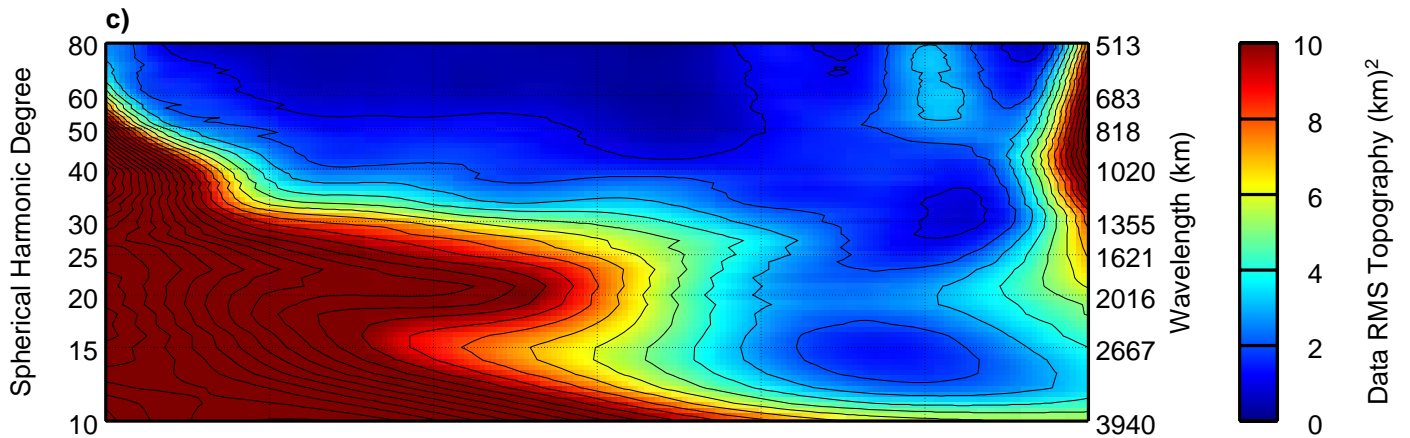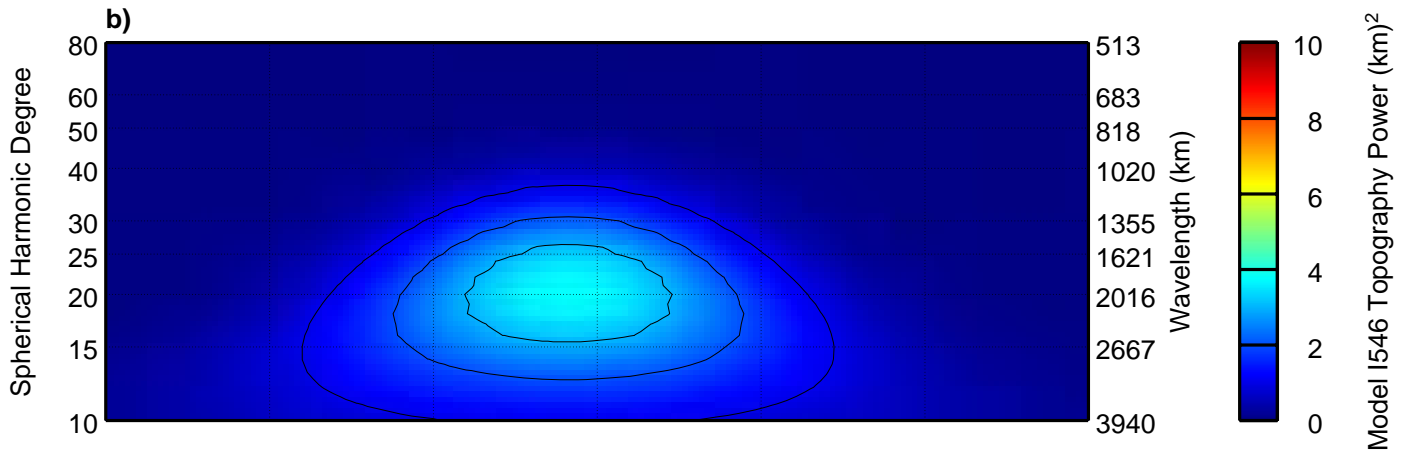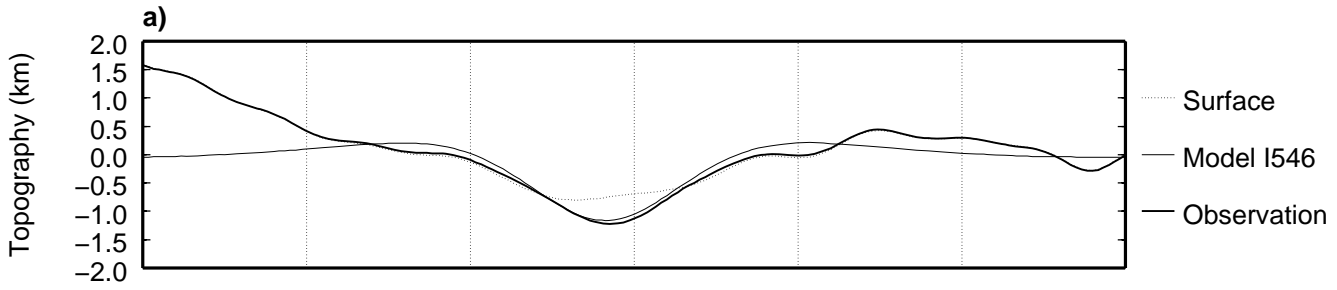
Figure 19: Same as Figure 18, but for gravity. Note that in c) the Congo gravity anomaly is isolated from other anomalies. In d) much of the anomalous power of gravity has been removed indicating a good model fit at the Congo basin and over the waveband containing the Congo gravity anomaly.
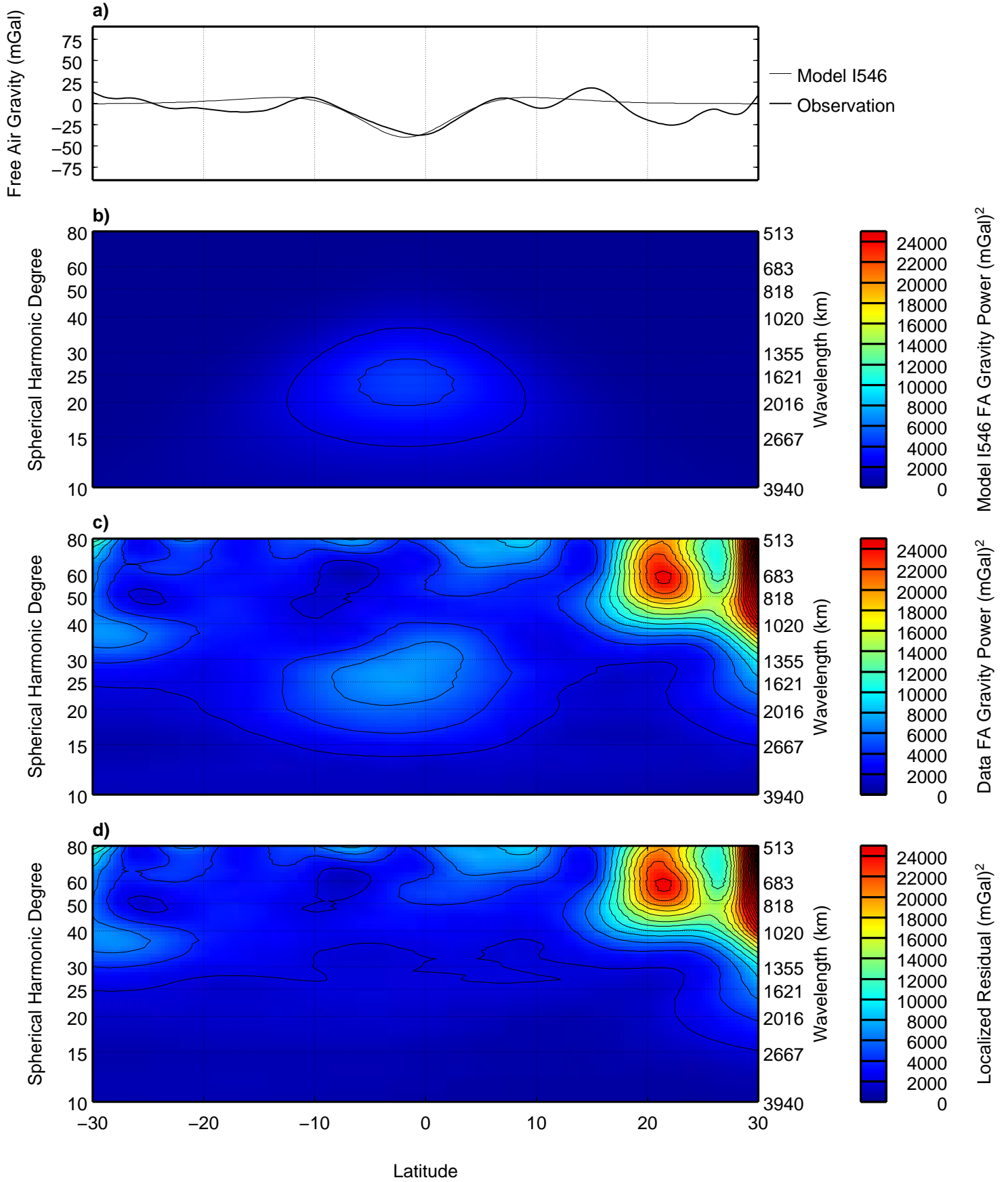
Figure 20: **a)** Same as Figure 7 for the input seismic velocity anomaly for a 100 km deep, 100 km wide anomaly of unit amplitude. This model has been projected onto the S20RTS tomography model's basis. **b)** Output of the filtering process of *Ritsema et al.* [2007] for the input model in a). The presence of this anomaly in the upper mantle is consistent with the observations in Figure 7.

a) Depth = 150 km   Depth = 300 km

Input Amplitude

b)

Depth = 150 km

Depth = 300 km
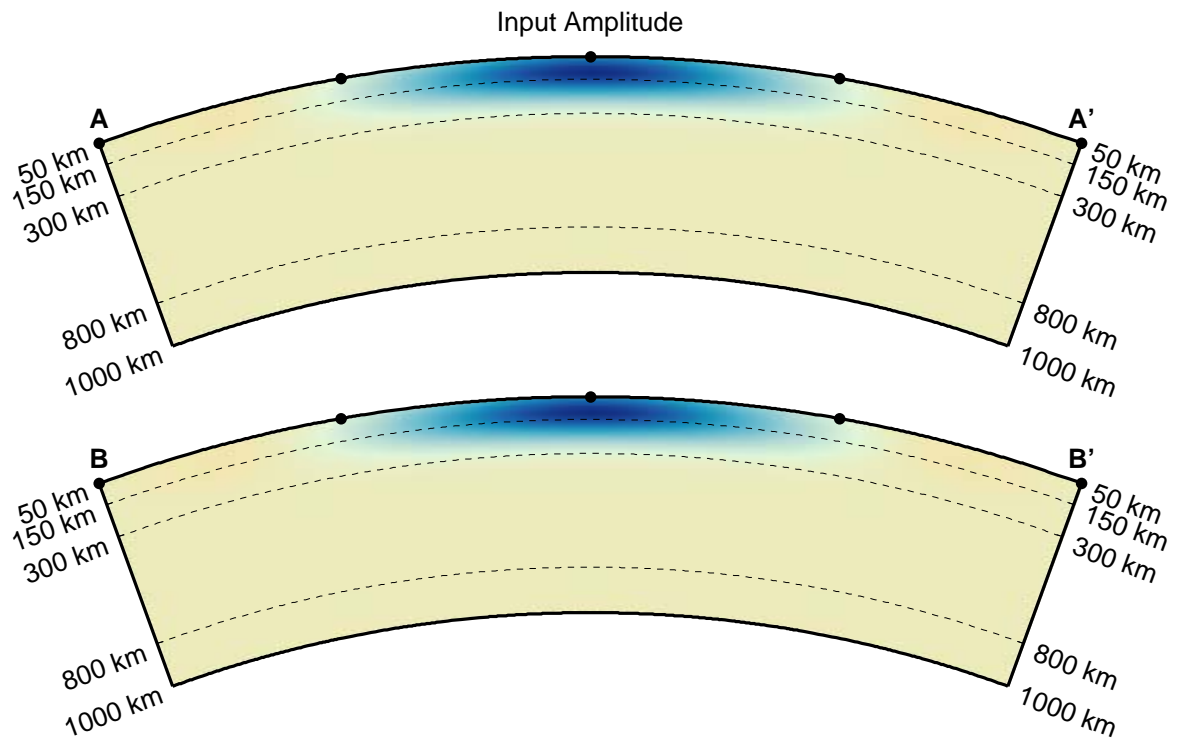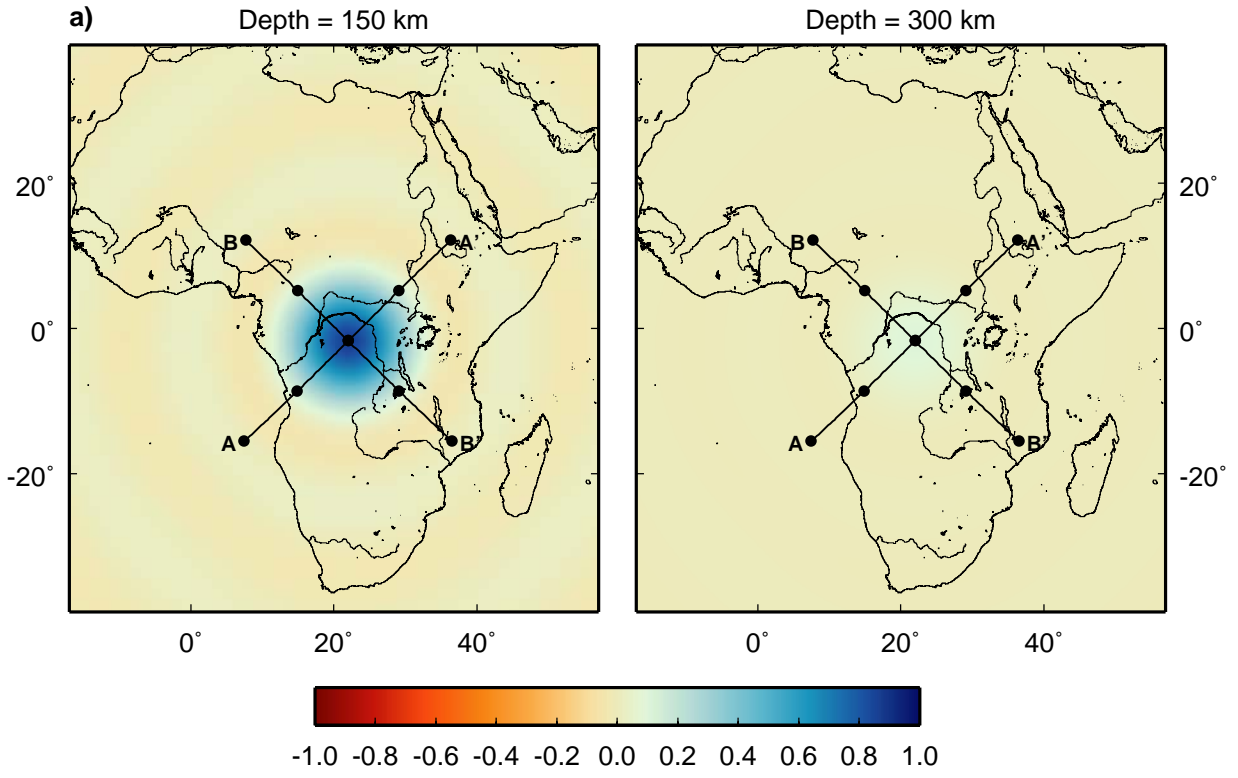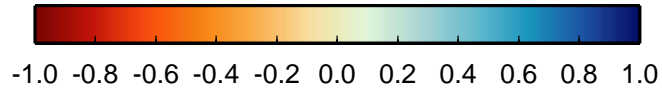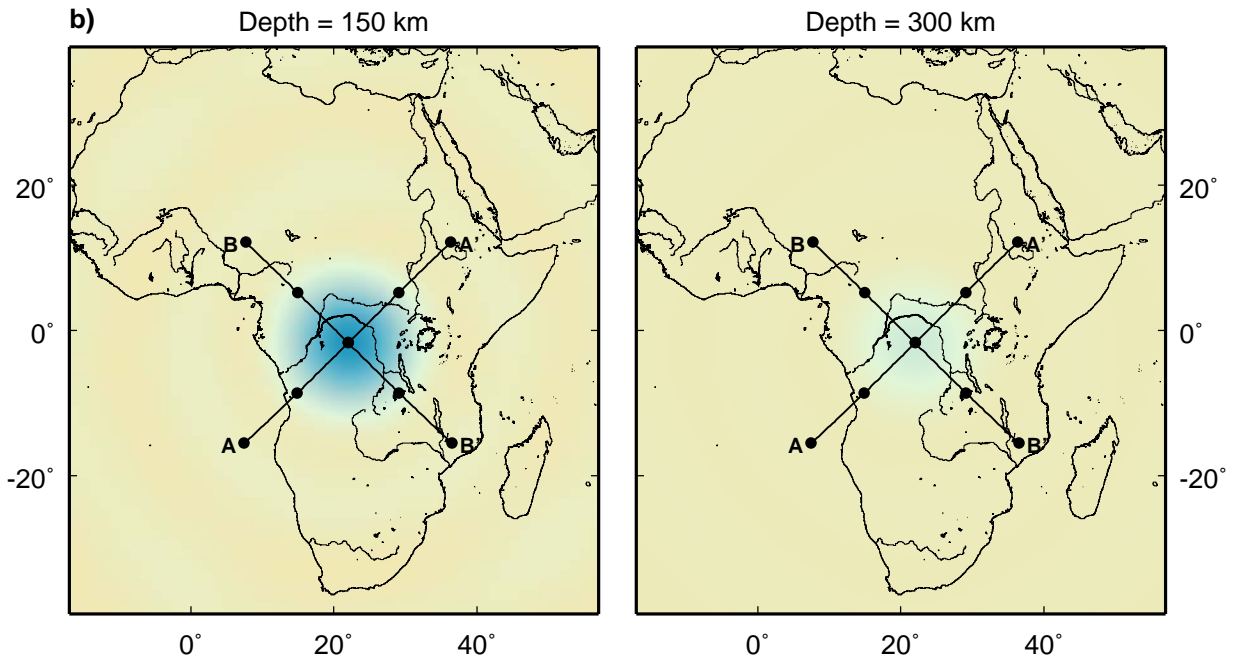
Input Amplitude Filtered to match S20RTS
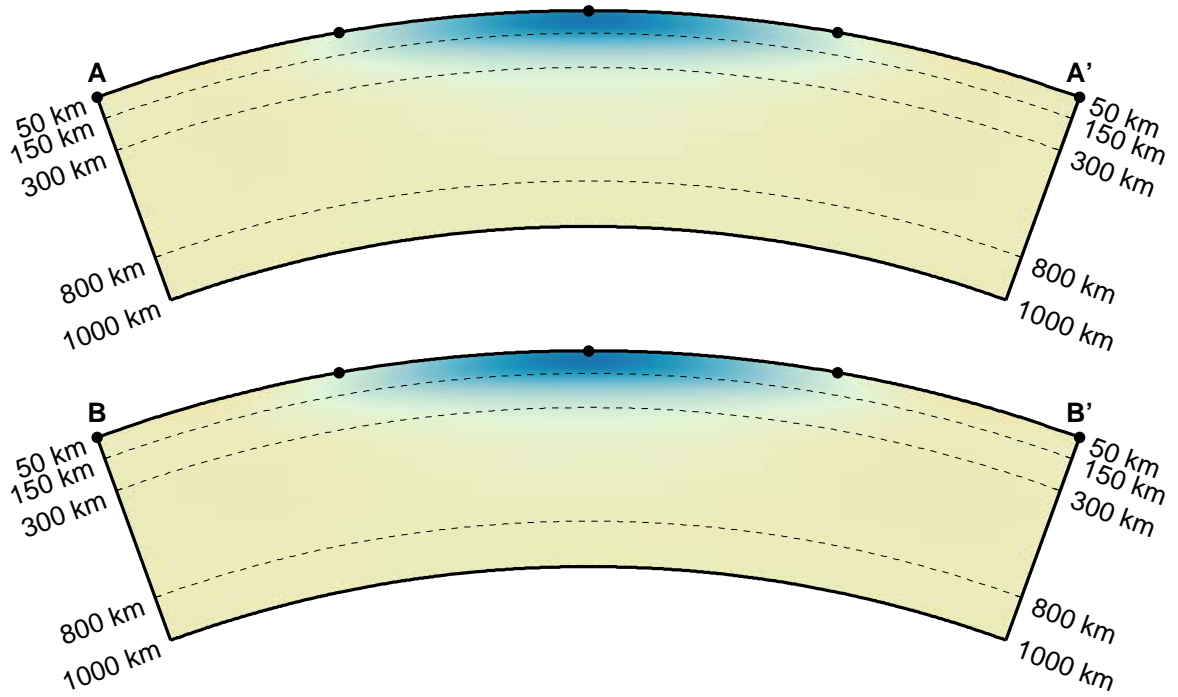
Figure 21: This diagram displays localized correlation coefficients between modeled and observed shear-wave velocity anomalies for the model geometries used here. Larger symbols indicate better fit. These coefficients have been calculated by localizing the correlation between the model and S20RTS basis splines to the uppermost mantle and horizontally to the Congo region using spatio-spectral localization.

Figure B1: Profile of the function used to weight the correlation of model and observed tomography to the uppermost mantle. This weighting function emphasizes the correlation in the uppermost 800 km of the mantle, the region which contains the anomalous shear-wave velocities observed beneath the Congo basin.

C h a p t e r   5

SUBSIDENCE HISTORY OF THE CRATONIC CONGO BASIN

Nathan J. Downey

Abstract

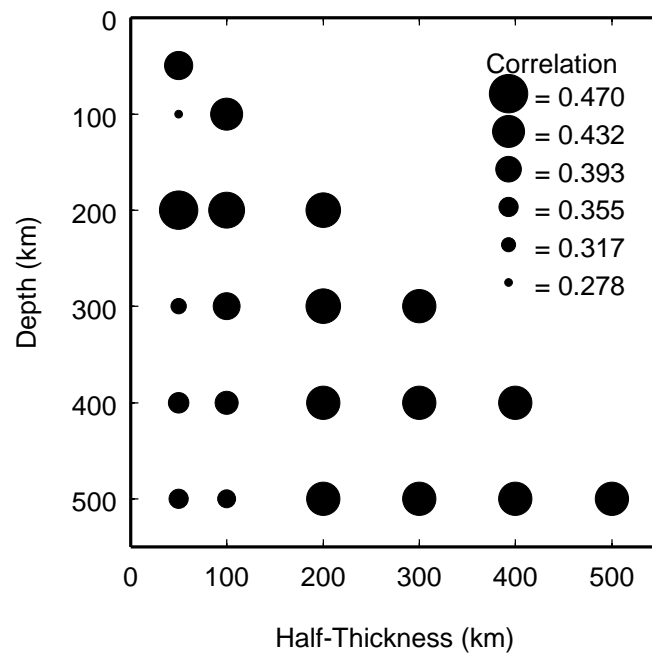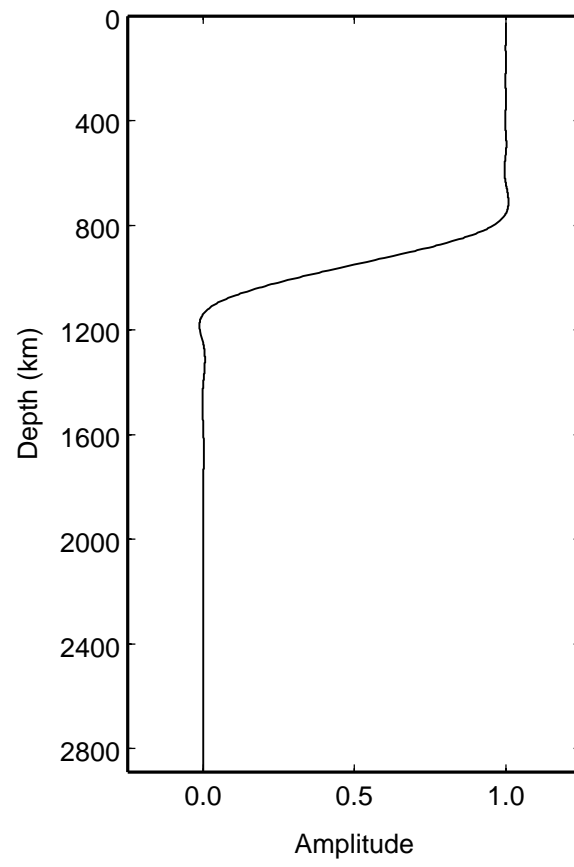The time-dependent properties of cratonic basins can yield insight into their formation mechanisms. The unusual properties of these basins including their intermittent subsidence, ellipsoidal isopach pattern and roughly simultaneous global subsidence have been difficult to explain. We present data that constrain the development of the Congo basin since the early Cretaceous. These data demonstrate that the Congo basin is currently not a location of major sediment deposition. We present two possible models for the history of the Congo basin since early Cretaceous time. In the first, subsidence in the basin and associated sediment deposition has slowly diminished over time to the current state in which sediment largely bypasses the basin to be deposited offshore. In the second model, the basin has rebounded. This second model explains the rapid increase in sedimentation that occurred at 34 Ma and also explains the origin of the uplifted central parts of the Congo basin.

1. Introduction

Understanding the mechanisms of intracratonic basin formation is critical for determining the mechanical properties of cratons and how they respond to changes in global tectonics. Unfortunately, the mechanisms forming these basins are still not fully understood. Their time-dependent properties, however, provide clues as to the nature of their formation mechanisms. Relating these properties to the dynamics of basin formation may provide insights into the rheology, thermal properties, and composition of cratons. A full understanding of the formation of intracratonic basins may not be necessary to constrain the physical properties of cratonic lithosphere; some constraint on the rheology and composition of continental interiors can be provided by examining individual properties of intracratonic basins.

Instantaneous models of the Cratonic Congo basin show that the late Jurassic-Quaternary subsidence within the basin is dynamically maintained. These models show that the gravity and topography observed at the Congo basin can be explained by viscous support of a high-density body located within the lithosphere at 100 km depth. While the current dynamics of the Congo basin can be modeled using a variety of lithospheric viscosity models, a tighter constraint on these structures can perhaps be gleaned from examining the current subsidence rate of the basin. Observations of the subsidence history of the Congo basin determined by 1-D backstripping of several wells contained within the basin (see Figure 1) indicate that the majority of the sediments within the dynamic surface depression were deposited during Cretaceous time and that there has been little net subsidence since. Additionally, the small-scale topographic structure of the central Congo basin indicates that much of the current surface of the basin is not depositional, an observation supported by the increase of sediment deposition at the offshore Congo fan sometime near the Eocene-Oligocene boundary (34 Ma). Thus the late Jurassic to Quaternary sedimentary infill of the Congo basin forms an unconformity-bounded sedimentary sequence typical of intracratonic basins.

We present dynamic models of the current subsidence of the Congo basin. These models show that an exponential or linear decrease in viscosity through the lithosphere results in a negligible subsidence rate. We also present two possible models for the development of Congo stratigraphy, one characterized by an exponential decrease and one in which the basin rebounds.

2. Time-dependent properties of intracratonic basins.

Intracratonic basins are the longest-lived of all basin types [*Woodcock*, 2004]. In terms of the mechanical properties of their substratum, intracratonic basins overlie ancient cratonic lithosphere which is thought to be stable over long periods (>1 Ga). In addition, intracratonic basins often, although not always, overlie ancient lithospheric rifts. Despite this superposition, the subsidence within intracratonic basins is generally not associated with rift activity because rift formation generally predates basin subsidence. The isopachs of intracratonic basins bear no resemblance to the linear structures of their underlying rifts. Instead, the isopachs of intracratonic basins follow a bi-variate Gaussian pattern [*Sloss*, 1991]. Intracratonic basins typically undergo several cycles of renewed subsidence resulting in the formation of superposed unconformity-bounded sediment packages. In addition, these cycles are observed, based on chronostratigraphic correlation, to occur somewhat simultaneously in intracratonic basins on a global scale [*Leighton and Kolata*, 1990]. The nature of chronostratigraphic control makes it difficult to determine the time-scales over which this synchronicity occurs [*Miall,* 1994, 1997]. If eustasy is the dominant factor determining deposition within a basin, it is expected that deposition should be globally synchronous over short time-scales. However, identifying this synchronicity at the time-scales of the briefest depositional events observed is not possible using chronostratigraphic data. Similarly, it is not known if the onset and termination of sedimentation within intracratonic basins occurs simultaneously, or if these basins subside at rates determined by local tectonics in response to global tectonic events. Mechanisms proposed to explain intracratonic basin formation have difficulty explaining the long-period global synchroneity of intracratonic basin activity, their typically circular isopachs and their periodic activity.

3. Cretaceous-Quaternary history of the Congo basin

3.1 Paleogeography and interaction with the passive margin

Throughout Cretaceous time, the Congo region of Africa was the location of a large shallow lake at the center of an internally-draining basin, reflected in the lacustrine or lagoonal character of the majority of sediments deposited in the basin at this time [*Guillocheau et al.*, 2007]. A few possible marine deposits of Cretaceous age are observed at the basin margins [*Giresse*, 2005]. This lake lay within a relative topographic low between the northern and southern regions of Africa. In the latest Cretaceous this lake was uplifted along with the rest of southern Africa, while remaining depressed relative to southern Africa, morphology similar to that observed today [*Guillocheau et al.*, 2007]. Also in the latest Cretaceous a shift to a drier climate occurred. The sediments deposited within the basin at this time exhibit a lacustrine or fluvial affinity; the dry climate indicates that the Congo basin at this time was probably analogous to the modern Chad basin [*Burke*, 1974]. A second climatic shift to wetter conditions occurred near the Eocene-Oligocene boundary at 34 Ma [*Séranne*, 1998; *Burke and Gunnell*, 2008]. This date corresponds to the global shift from greenhouse to icehouse climatic conditions [*Séranne*, 1998]. The Eocene-Oligocene boundary also marks the initiation of high rates of sediment deposition at the Congo deep-sea fan [*Lavier et al.*, 2001; *Leturmy et al.*, 2003; *Anka and Séranne*, 2004; Figure 2]. *Séranne and Anka* [2005] and *Séranne* [1998] attribute this increase to the shift to a warmer climate that occurred at this time. Since 2.8 Ma the Congo region of Africa has been extremely wet, with the central portion of the Congo basin currently receiving some of the highest rainfall observed on the African continent [*Burke and Gunnell*, 2008].

3.2 Backstripping

The late-Jurassic to Quaternary stratigraphy of the Congo basin is characterized by thick Mesozoic sections overlain by a thin Cenozoic cover. The ages of the individual units

within this section are poorly determined [*Giresse*, 2005]. We identify five distinct stratigraphic units observed within three different wells (Figures 1 and 3). The basal Stanleyville formation, which is observed in the Samba and Gilson wells, but not in the Dekese well (Figure 3) is a fining-upward conglomeratic unit which lies unconformably over Paleozoic and Triassic units [*Giresse*, 2005; *Daly et al.*, 1992]. The age of this unit is late Jurassic to early Cretaceous. The Stanleyville is overlain by the lower-Cretaceous Loia formation and the upper Cretaceous Bokungu formations. The Kwango formation is identified here as being late Cretaceous in age, although it may also date from the earliest Tertiary. Above the Kwango exists a thin veneer of sediments of unknown, but probably Cenozoic, age.

Sahagian (1993) attempted to discern the tectonic subsidence of the Congo basin by backstripping the sediments of the Samba well. In his analysis *Sahagian* [1993] corrected for sea-level using the curves from *Sahagian* [1988], resulting in a linear tectonic subsidence curve for the basin. *Sahagian* [1993] interpreted this curve to indicate that the Congo basin is a passive receptacle of sediment eroded from surrounding uplifted regions. Re-examination of the paleogeographic data outlined above indicates that correcting for sea-level change in the subsidence analysis of the Congo basin is not warranted given the continental nature of the sediment infill.

We present a 1-D backstripping analysis of the Gilson, Dekese and Samba wells in which we have not applied a correction for sea-level change (Figure 3). The age of the units within the wells also differs slightly from that of *Sahagian* [1993]. We based our ages upon the review by *Giresse* [2005] (Table 1); however, the age differences are not significant given the large uncertainties associated with dating the strata. The resulting subsidence history is consistent between wells and indicates that the Congo basin subsided, relative to a local base-level unique to each well, at a rate of approximately 15-20 m/Myr throughout the early Cretaceous (note that this rate is the observed total subsidence rate, the estimated tectonic subsidence rate for the same period ranges 6-8 m/Myr). These rates are consistent with rates generally observed for individual subsidence events within cratonic basins [*Leighton and Kolata*, 1990]; total subsidence

rates averaged over longer time periods tend to be smaller, less than 10 m/Myr and often less than 5 m/Myr [*Sloss*, 1996]. Since the mid Cretaceous there has been a period of apparent quiescence represented by the thin late Cretaceous and Cenozoic sections observed within the wells. It is important to note that, for conformable stratigraphic sections and in the absence of additional constraints, subsidence curves determined by backstripping will always show a monotonic increase in basin subsidence.

3.3 Small-scale topographic structure of the Congo basin

Local relief is defined as the difference in elevation (Δh) between regions separated by a horizontal length scale d and can be estimated using:

$$\Delta h(\vec{\delta}) = \left\langle \left| h(\vec{x} + \vec{\delta}) - h(\vec{x}) \right| \right\rangle \tag{1}$$

where $h(\vec{x})$ is the elevation at a location $\vec{x}$ in the plane and $\vec{\delta}$ is a vector of magnitude d [*Weissel et al.*, 1994]. The brackets $\langle \ \rangle$ denote a spatial averaging operation. If the scaling properties of topography are isotropic then Δh only depends on d and can often be described using a power–law relation,

$$\Delta h(d) = Cd^H \ , \tag{2}$$

in which C is an amplitude factor and H is the Hurst exponent [*Weissel et al.*, 1994]. *Aharonson and Schorghofer* [2006] use local estimates of H to characterize Martian topography, finding that smooth regions are characterized by low values of H, while rougher regions are characterized by $H \sim 0.8$. *Hurtrez et al.* [1999] find that terrestrial estimates of H are dependent upon d, with scales between ~100 and ~1000 m being dominated by fluvial erosion characterized by $H \sim 0.5$. *Weissel et al.* [1994] calculate H for three regions within Saudia Arabia and northeast Africa, finding that the topography in these regions is characterized by $0.5 < H < 0.7$.

We estimate the local relief in the Congo basin using Shuttle Radar Topography Mission (SRTM) Version 3 [*Jarvis et al.*, 2008] topography at a variety of length scales within the range 450 m $< d <$ 1170 m using equation (1). This range of scales restricts us to the scales which are sensitive to fluvial processes, with the lower bound being chosen so that we are estimating relief at a minimum distance of approximately 5 times the resolution of the SRTM data. We estimate the local relief on a regular grid by finding the relief between every unique pair of data points, separated by a distance equal to d, within a 5 km radius of each grid point. We then average these relief estimates, weighted by their distance from the grid point.

Although the Congo basin is a topographic depression on a large scale, examination of the small-scale topography of the "Eastern Region" (Figure 4a) reveals a valley and ridge morphology typical of fluvially-modified topography. The "Western Region" in Figure 4a exhibits a smooth morphology. The estimated local relief for $d = 900$ m confirms these general topographic styles of the central regions of the Congo basin (Figure 4b). The local relief in the Eastern Region generally ranges between 10 m and 30 m and increases to the southeast, while the Western Region is typified by a local relief less than 10 m. The Hurst exponent estimated over the 450 m $< d <$ 1170m length scale range is ~ 0.4 for much of the Eastern Region, consistent with a fluvially-modified landscape and ~ 0.1 for the Western Region, indicating a flat topography. The Hurst exponent in the Western Region tends to be larger, ~ 0.4, near stream channels. The incision of the rivers into the topography of the eastern region is also evidenced in the Unesco geologic map of the region (Figure 4d) [*CGMW/Unesco*, 1987]. The Western Region roughly corresponds to the location of the most recent sedimentation, indicated by the late-Quaternary age of the exposed sediments. This region is also dominated by wetlands. In the Congo-bounded region, several rivers have eroded through the Cenozoic section and Mesozoic rocks are exposed in the base of the river valleys.

The small-scale morphology and surface geology of the Congo basin indicate that much of the modern surface of the Congo basin is not the site of sediment deposition interface. Our poor understanding of the interaction between erosion, surface uplift, lithology and

climate patterns does not allow us to attach any significance to the southeastward increase in local relief. The ongoing erosion of the Congo topography has an important implication for the dynamics of Congo subsidence because it indicates that the magnitude of the dynamic topography is not rapidly changing.

4. Dynamic models of current Congo Basin subsidence

We use a finite element formulation of thermal convection of viscous material (CitcomT, [*Billen et al., 2003*]) to model the current subsidence rate of the Congo basin. Thermal convection in the mantle is modeled by the Stokes and continuity equations under Boussinesq and infinite Prandtl number conditions:

$$\vec{\nabla} \cdot \tilde{\sigma} + \vec{f} = \vec{0} \tag{3}$$

$$\vec{\nabla} \cdot \vec{u} = 0. \tag{4}$$

The time-dependence is given by the heat equation:

$$\frac{\partial T}{\partial t} + \vec{u} \cdot \vec{\nabla} T = \kappa \nabla^2 T \tag{5}$$

and we assume a Newtonian-viscous constitutive relation:

$$\tilde{\sigma} = -P\tilde{I} + \eta \tilde{\dot{\varepsilon}} . \tag{6}$$

$\tilde{\sigma}$ is the stress tensor, $\vec{f}$ is the gravitational body-force, $\vec{u}$ is velocity, t is time, T is temperature, κ is thermal diffusivity, $\tilde{I}$ is the identity tensor, P is pressure, η is the dynamic viscosity and $\tilde{\dot{\varepsilon}}$ is the strain-rate tensor. η given by the viscosity law:

$$\eta = \eta_o \exp\left(\ln(r)\frac{1-f(\vec{x})}{1+v_T f(\vec{x})}\right),\tag{7}$$

in which $f \in [0,1]$, termed the "effective temperature", is a function of position $\vec{x}$, r is the ratio of maximum to minimum viscosity and v_T describes the decay of viscosity with increasing f. η_o determines the maximum viscosity associated with the density anomaly and is expressed in terms of the depth at which this maximum viscosity equals the background viscosity (symbolized η_{eqv} and expressed in km). To calculate the change in surface topography with time, we solve the Stokes and continuity equations at two times [*Gurnis, et al.*, 2000] between which the evolution of the temperature field within our model is governed by equation (5). The difference in the magnitude of the surface dynamic topography at these two times divided by the duration of the time step estimates the current subsidence rate of the basin (typically 10^5 yr).

We calculate subsidence rates for the models of Table 2. In all these models the density anomaly is centered at 100 km depth. The variable we are trying to constrain using the subsidence rate calculation is v_T, the parameter which controls the rate at which viscosity decays with depth in the lithosphere. The results of our uplift calculations show that subsidence rate does vary with v_T: models whose decay is super-exponential with depth have maximum subsidence rates ranging from 15-43 m/Myr with diffusion and 27-56 m/Myr without diffusion. Models whose viscosity decay rate with depth is near exponential or linear have much smaller maximum rates of 2.3-5.7 m/Myr without diffusion (Figure 5). For these models diffusion reduces subsidence rate even to the point of uplift. It seems that thermal diffusion could act as a stabilizing process for the Congo anomaly; other stabilizing forces could be at work and more detailed modeling needs to be carried out. If the Congo basin is currently not a major depositional location, models with an exponential, or linear, decay in viscosity with depth are preferred because of their low subsidence rates.

5. Discussion and Conclusions

Throughout the Cretaceous the Congo basin was the location of an internally draining watershed. Subsidence within the basin provided accommodation space for sediment deposition which reached up to 1 km in thickness as evidenced by the Cretaceous sedimentary rocks preserved in the basin. Contrast this observation with the current state of the Congo basin in which sediments largely bypass the continental basin to be deposited at the Congo deep-sea fan. The current state of the Congo basin is typical of intracratonic basins. Sediment supply within cratonic basins almost always meets or exceeds the accommodation space made available by the slow subsidence typical of these basins; sediment-starved intracratonic basins are rarely observed in the geologic record [*Sloss*, 1996]. From analysis of the basin stratigraphy observed in the basin's wells, it appears the shift to an externally-draining state occurred in the late Cretaceous, given the thin Cenozoic sediment cover observed within the basin.

We present two possible subsidence histories for the Congo basin which are consistent with observations (Figure 6). In the first, the subsidence of the basin is characterized by exponential decay (Figure 6a). Subsidence was rapid throughout the early Cretaceous, decreasing to extremely low rates in the Cenozoic. The transfer of deposition location from within the basin to without would have been a gradual process. Finally at the present day, when subsidence has essentially stopped, sediment would be routed to final deposition locations exterior to the basin. A second possibility is one in which the Congo basin rebounded during the Cenozoic (Figure 5c). In this model, the basin reaches maximum subsidence sometime within the Cenozoic after which it rebounds resulting in erosion at the basin's surface. This model is stratigraphically indistinguishable from the exponential-decay model. We have no constraint on how much sediment has been eroded: the exponential model predicts a small amount, the rebound model predicts a large amount.

Important for distinguishing between these models is the age of the Cenozoic strata within the basin. The exponential decay model predicts that these strata should be largely

late Cretaceous to Paleogene in age with a decreasing thickness into the Neogene. The rebound model predicts that these strata should date exclusively from the late-Cretaceous to Paleogene. Unfortunately our poor constraint on the ages of these strata does not allow us to distinguish these models in this manner. A second observation which distinguishes these models is the rate of sedimentation increase on the passive margin. In the exponential decay model, sediment deposition is gradually transferred out of the Congo basin, while in the rebound model the transfer should be sudden, with a sustained increase in sedimentation at the new deposition location as the transfer of sediment from the basin to the new location is enhanced by basin uplift. The rapid increase of sedimentation at the Congo passive margin lends support to the basin rebound hypothesis. Sedimentation at the passive margin also constrains the timing of this rebound event to prior to 34 Ma. *Anka and Séranne* [2003] attribute the massive increase in sedimentation at the coast as a response to a change in climate at this time. The magnitude of sedimentation increase at the coast, however, probably is in response to a large-scale reorganization in the sediment routing system of the Congo region. While the efficiency of this transfer would have been greatly enhanced due to a climatic change, the underlying cause is probably dynamic in origin.

The two possible subsidence histories outlined in Figure 6 also imply differing subsidence mechanisms. Exponential decay is usually associated with contraction following a thermal disturbance within the lithosphere. Hot-spot volcanism is usually cited as a source in the case of intracratonic basins. The current high-density region beneath the Congo basin would therefore represent a mass of material which was emplaced within the lithosphere and then cooled to its present state. However there are several problems with this hypothesis. There is no evidence for recent surface volcanism within the Congo basin and there is a question of space. The rifts underlying the Congo basin have been inactive since the Paleozoic so it is not easy to see how space for a large magmatic body within the lithosphere could have been created. Subsidence followed by rebound is indicative of the generation of a lithospheric instability. In this model, the lithosphere beneath the Congo region became unstable during the Cretaceous, perhaps aided by a phase change, flowed downward into the mantle and detached. The rebound

represents the declining topographic influence of this sinking lithospheric chunk as it sank deeper in the mantle. The current high-density anomaly observed within the lithosphere represents the remnants of this instability, perhaps preserved because of its location within the highly viscous upper mantle.

The mantle instability model of intracratonic basin formation is also attractive because it helps to explain some of the unusual properties of intracratonic basins. An axially-symmetric or near-symmetric lithospheric instability depresses the surface in a basin-like shape, resulting in a roughly circular or oval shaped depression. The resulting isopach closely resembles the bi-variant Gaussian pattern described by *Sloss* [1991]. *DeRito et al.* [1983] show that the formation of lithospheric instabilities such as the one hypothesized here can be enhanced by changes in continental stress patterns. Large tectonic re-organizations could explain why these instabilities form beneath different intracratonic basins at roughly similar times. Smaller period variations in subsidence rates between basins could result from local effects, such as lithospheric thickness and thermal state. Finally, the Late-Jurassic to Quaternary strata within the Congo basin form an unconformity-bound sequence typical of intracratonic basins. The largely continental nature of the sediments within this package indicates that the bounding unconformities are unrelated to sea-level change. A lithospheric instability mechanism can therefore explain the subsidence patterns typically observed in intracratonic basins.

References

Aharonson, O. and N. Schorgehofer (2006), Subsurface ice on Mars with rough topography, *Journal of Geophysical Research, 111,* E11007, doi:10.1029/2005JE002636.

Anka, Z. and M. Séranne (2004), Reconnaissance study of the ancient Zaire (Congo) deep-sea fan (ZaiAngo Project), *Marine Geology*, *209*, 223-244, doi:10.1016/j.margeo.2004.06.007.

Billen, M. I., M. Gurnis and M. Simons (2003), Multiscale dynamics of the Tonga-Kermadec subduction zone, *Geophysical Journal International*, *153*, 359-388.

Burke, K. (1976), The Chad basin: An active intra-continental basin, *Tectonophysics*, *36*, 197-206.

Burke, K. and Y. Gunnell, (2008), The African erosion surface: A continental-scale synthesis of geomorphology, tectonics and environmental change over the past 180 million years, *Geological Society of America Memoir*, *201*, 1-66, doi:10.1130/2008.1201.

Cahen, L. (1954), *Géologie du Congo Belge*, H. Vaillant-Carmanne, Liège.

CGMW/Unesco (1987), International Geological Map of Africa 1/500000, 6 panels, CGWM/Unesco, Paris, France.

Daly, M. C., S. R. Lawrence, K. Diemu-Tshiband and B. Matouana (1992), Tectonic evolution of the Cuvette Centrale, Zaire, *Journal of the Geological Society of London*, *149*, 539-546.

DeRito, R. F., F. A. Cozzarelli, and D. S. Hodge (1983), Mechanism of subsidence of ancient cratonic rift basins, *Tectonophysics*, 94, 141-168.

Giresse, P., (2005), Mesozoic-Cenozoic history of the Congo basin, *Journal of African Earth Sciences*, *43*, 302-315, doi:10.1016/j.jafrearsci.2005.07.009.

Guillocheau, F., N. Rolland, J. P. Colin, C. Robin, D. Rouby, J. J. Tiercelin, and O. Dauteuil, (2007), Paleogeography of Africa through Meso-Cenozoic Times: A focus on the continental domain evolution, *Mémoires Géosciences Rennes*, *hors série n°7,* 35-37.

Gurnis, M., J. X. Mitrovica, J. Ritsema, and H.-J. van Heijst, (2000) Constraining mantle density structure using geological evidence of surface uplift rates: The case of the African Superplume, *Geochemistry, Geophysics, Geosystems 1* (11), Paper number 1999GC000035.

Hurtrez, J.-E., F. Lucazeau, J. Lave and J.-P. Avouac (1999), Investigation of the relationships between basin morphology, tectonic uplift, and denudation from the study of an active fold belt in the Siwalik Hills, central Nepal, *Journal of Geophysical Research*, *104*, 12779-12796.

Jarvis, H. I., A. Nelsom and E. Guevara (2008), Hole-filled seamless SRTM data V3, International Center for Tropical Agriculture (CIAT), available from http://srtm.csi.cgiar.org.

Lavier, L. L., Steckler, M. S. and F. Brigaud (2001), Climatic and tectonic control on the Cenozoic evolution of the West African margin, *Marine Geology*, *178*, 63-80.

Leighton, M. W., and D. R. Kolata (1990), Selected interior cratonic basins and their place in the scheme of global tectonics, in *Interior Cratonic Basins: American*

Association of Petroleum Geologists Memoir, *51*, edited by M. W. Leighton, et al., pp.729-797, AAPG, Tulsa.

Leturmy, P., Lucazeau, F. and F. Brigaud, (2003), Dynamic interactions between the gulf of Guinea passive margin and the Congo River drainage basin: 1. Morphology and mass balance, *Journal of Geophysical Research*, *108*, 2383, doi:10.1029/2002JB001927.

Miall, A. D. (1994), Sequence stratigraphy and chronostratigraphy: Problems of definition and precision in correlation and their implications for global eustasy, *Geoscience Canada*, *21*, 1-26.

Miall, A. D. (1997), *The Geology of Stratigraphic Sequences*, Springer-Verlag, Berlin.

Sahagian, D. (1988), Epeirogenic motions of Africa as inferred from Cretaceous shoreline deposits, *Tectonics*, *7*, 125-138.

Sahagian, D. (1993), Structural evolution of African Basins: Stratigraphic synthesis, *Basin Research*, *5*, 41-54.

Séranne, M. (1999), Early Oligocene stratigraphic turnover on the west Africa continental margin: A signature of the Tertiary greenhouse-to-icehouse transition?, *Terra Nova*, *11*, 135-140.

Séranne, M. and Z. Anka, (2005), South Atlantic continental margins of Africa: A comparison of the tectonic vs climate interplay on the evolution of equatorial west Africa and SW Africa margins, *Journal of African Earth Sciences*, *43*, 283-300, doi:10.1016/j.jafrearsci.2005.07.010.

Sloss, L. L. (1991), The tectonic factor in sea level change: A countervailing view, *Journal of Geophysical Research*, *96*, 6609-6617.

Sloss, L. L. (1996), Sequence stratigraphy on the craton: caveat emptor, *in Paleozoic Sequence Stratigraphy; Views from the North American Craton, GSA Special Paper 306*, edited by B. J. Witzke, et al., pp. 425, GSA, Boulder, doi: 10.1130/0-8137-2306-X.425.

Weissel, J. K., L. F. Pratson and A. Malinverno (1994), The length-scaling properties of topography, *Journal of Geophysical Research*, *99*, 13997-14012.

Woodcock, N. H. (2004), Life span and fate of basins, *Geology*, *32*, 685-688, doi:10.1130/G20598.

Tables

Table 1: Stratigraphic ages used in Backstripping analysis

Formation	Age Range (Ma)
Late Cretaceous-Cenozoic (C_z)	90-0
Kwango	99-90
Bokungu	121-99
Loia	140-121
Stanleyville	150-140

Table 2: Summary of uplift models

Models (w/out,w/ diffusion)	v_T	η_{eqv} Depth (km)	Mass Anomaly (10^{18} kg)	Half- Thickness (km)	$\Delta\rho_{max}$ (kg/m^3)	Subsidence Rate, No Diffusion (m/Ma)	Subsidence Rate with Diffusion (m/Ma)
U018,U003	4.35	50	8	100	27	26.5	14.7
U017,U001	4.35	50	9	100	30	31.2	18.1
U019,U004	4.35	50	10	50	60	29.4	24.9
U020,U006	4.35	100	9	100	30	32.9	19.8
U016,U007	0.1	50	8	100	27	5.4	-6.3
U021,U008	0.1	50	9	50	54	5.7	1.1
U022,U011	10	50	9	100	30	56.4	43.0
U023,U015	-0.9	50	9	50	54	1.4	-2.3

Figure 1: Isopach map of the Late-Jurassic to Quaternary sedimentary infill of the Congo basin. These sedimentary rocks fill the bottom of a long-wavelength dynamic depression in the Earth's surface. The locations of three wells used to constrain the subsidence history of the basin are shown.
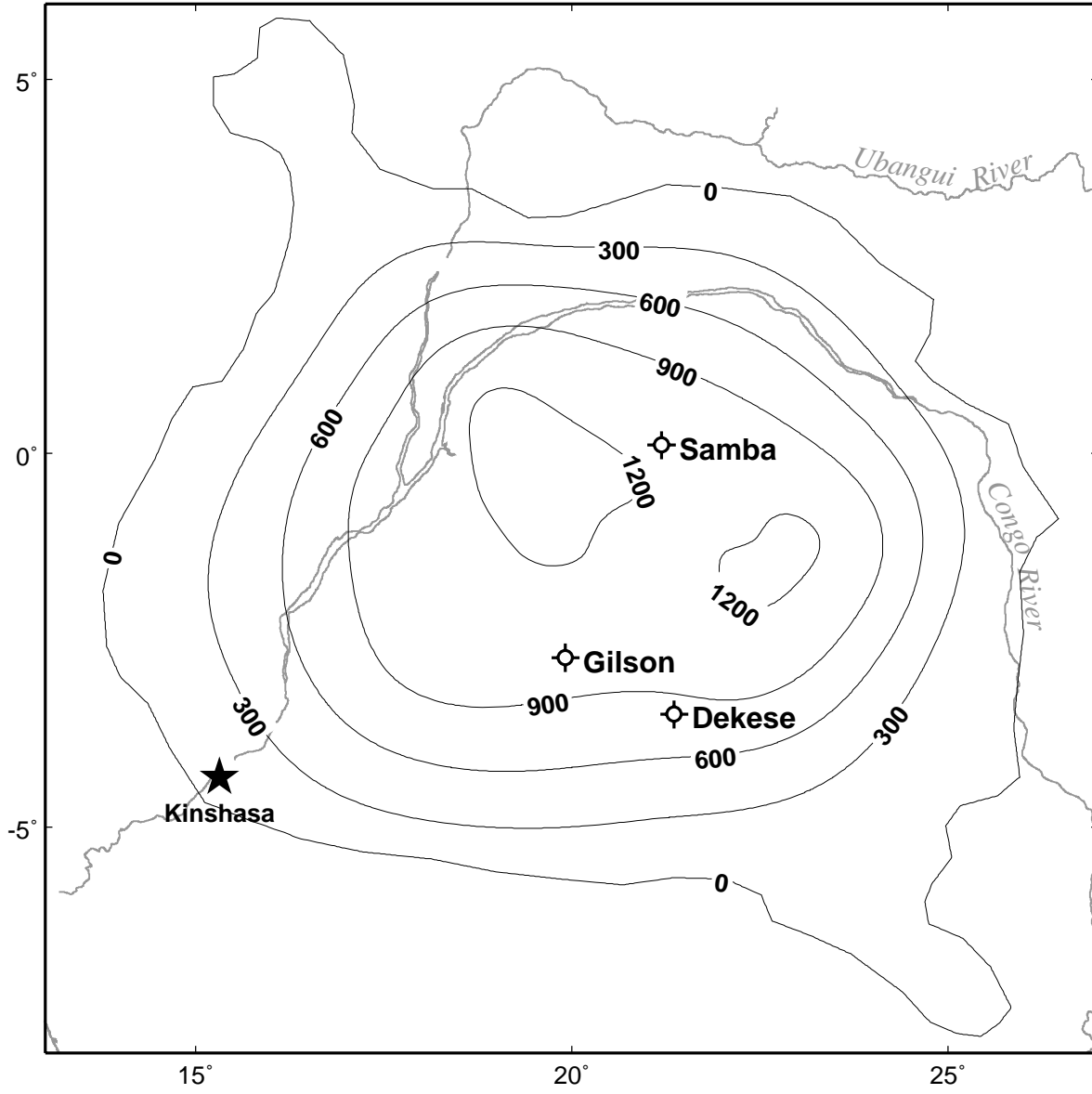
Late-Jurassic to Quaternary Isopach in metres

Figure 2: History of sedimentation on the Congo/Angolan margin of central Africa, taken from *Leturmy et al.* [2003]. The sedimentation rates are those observed on three profiles across the margin, denoted Congo (C), Gabon (G) and Angola (A). Sediments deposited prior to 90 Ma are associated with the development of the passive margin as Africa rifted away from South America. From 90 Ma to 34 Ma sedimentation at the coast was limited to sediment discharge from small coastal streams. 34 Ma marks a major increase in the rate of sedimentation at the passive margin, probably reflecting a significant change in the depositional system of the Congo basin, after which sedimentation rates averaged 40 m/Myr along the profiles shown.
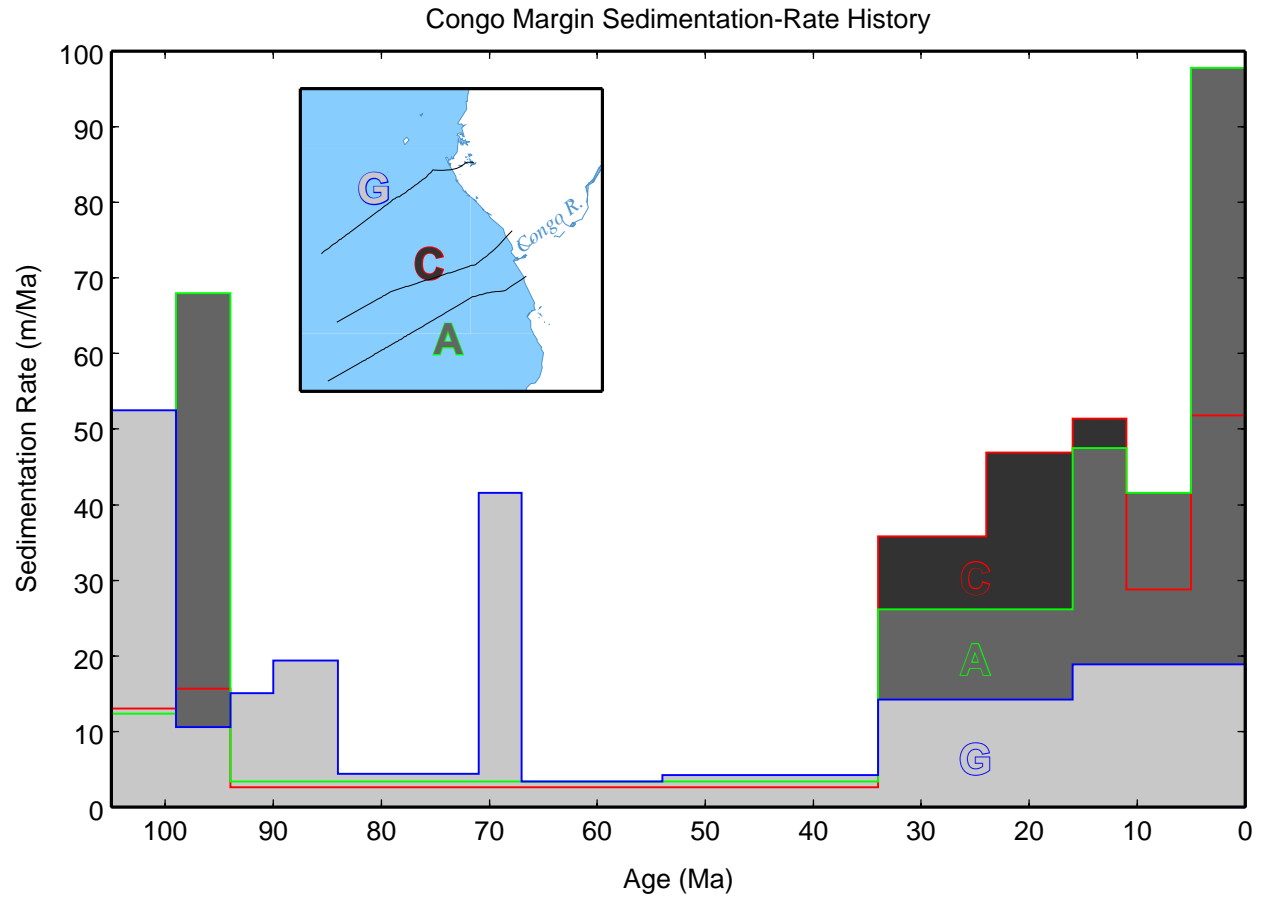
Congo Margin Sedimentation-Rate History

Figure 3: **a)** Total subsidence (dotted line and open circles) and backstripped tectonic subsidence (solid circles and solid line) calculated using the stratigraphy observed in the Gilson well. **b)** Geohistory diagram for the Gilson well. The thickness of the stratigraphic units are shown over time. Note that the Cenozoic section is much thinner than the Mesozoic section. The basal conglomerates of the Stanleyville formation lie unconformably on the deeper Paleozoic and Triassic strata of the basin. **c)-d)** Same as for a)-b) but for the stratigraphy of the Samba well. Note the thicker Stanleyville section here. This reflects the south and eastward thinning of the Stanleyville formation within the basin. **e)-f)** Subsidence and geohistory for the Dekese well. The Stanleyville and Kwango formations are not observed here; however, the thickness of the Bokungu formation is greater than observed in the other wells, which may result from an inability to distinguish Kwango from Bokungo strata within the Dekese section. All the tectonic subsidence curves demonstrate the same general pattern of relatively rapid Mesozoic subsidence of 15-20 m/Ma followed by a Cenozoic period of quiescence. See text for details on the assumptions used to create these plots and limitations in their interpretation.
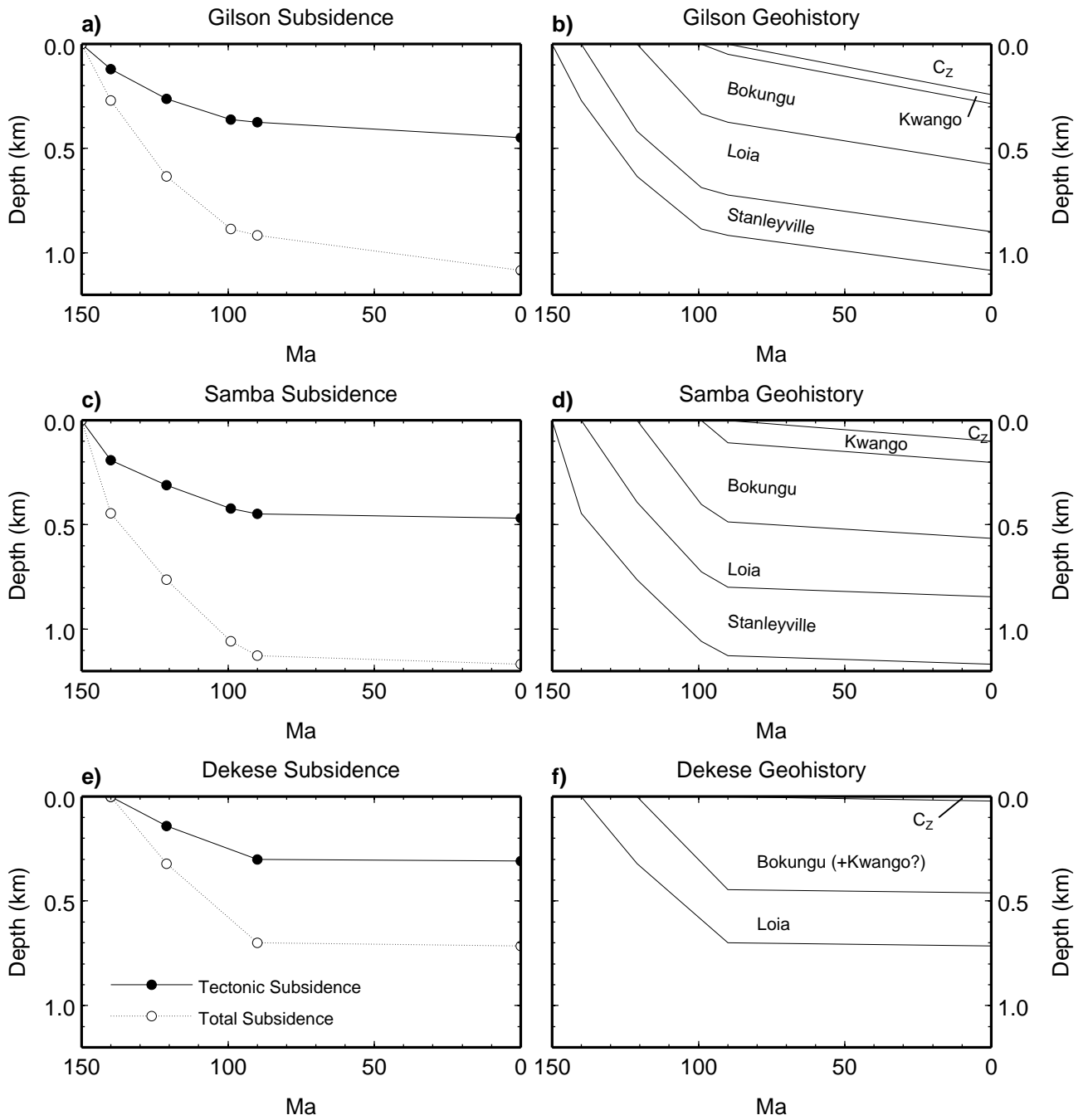
a) Gilson Subsidence

b) Gilson Geohistory — C$_z$, Bokungu, Kwango, Loia, Stanleyville

c) Samba Subsidence

d) Samba Geohistory — Kwango, C$_z$, Bokungu, Loia, Stanleyville

e) Dekese Subsidence — Tectonic Subsidence, Total Subsidence

f) Dekese Geohistory — C$_z$, Bokungu (+Kwango?), Loia

Figure 4: **a)** SRTM topography of Congo Basin. Location corresponds to that of Figure 1. The Congo and Ubangui rivers are labeled for reference. The 300 m isopach of the Mesozoic-Quaternary sedimentary strata and the Congo River are used to outline boundaries of two regions, denoted the eastern and western regions. The white box shows the location of Figure 4d. **b)** Local relief, calculated as detailed in the text, over a length scale of 990 m. The local relief within the eastern region generally ranges between 10 m and 30 m and increases to the southeast, while much of the area of the western region is much smoother with local relief typically less than 10 m. **c)** The Hurst exponent calculated over a range of scales varying from 450 m to 1170 m. While the distinction between the eastern and western regions is not as clear as in the local relief, the eastern region exhibits a Hurst exponent in the range $0.3 < H < 0.8$. A notable exception occurs near 23°W, 2°S where $H \sim 0.1$. In the western region, the smoothest regions have $H \sim 0.1$ with higher values coinciding with river channels. **d)** Detail of the surface geology of the Congo basin [*CGMW/Unesco,* 1987]. Q_2 denotes late Quaternary sediments. N_2-Q_1 denotes Neogene to early Quaternary sediments (although the true age of these sediments is unknown. They could date from the Late Cretaceous to Quaternary. See text for details). K_1 are upper Cretaceous and K_2 are middle Cretaceous aged sediments. Much of the western region contains recent deposits, while in the eastern region rivers have incised into older deposits as evidenced by the Cretaceous exposures in their headwaters.
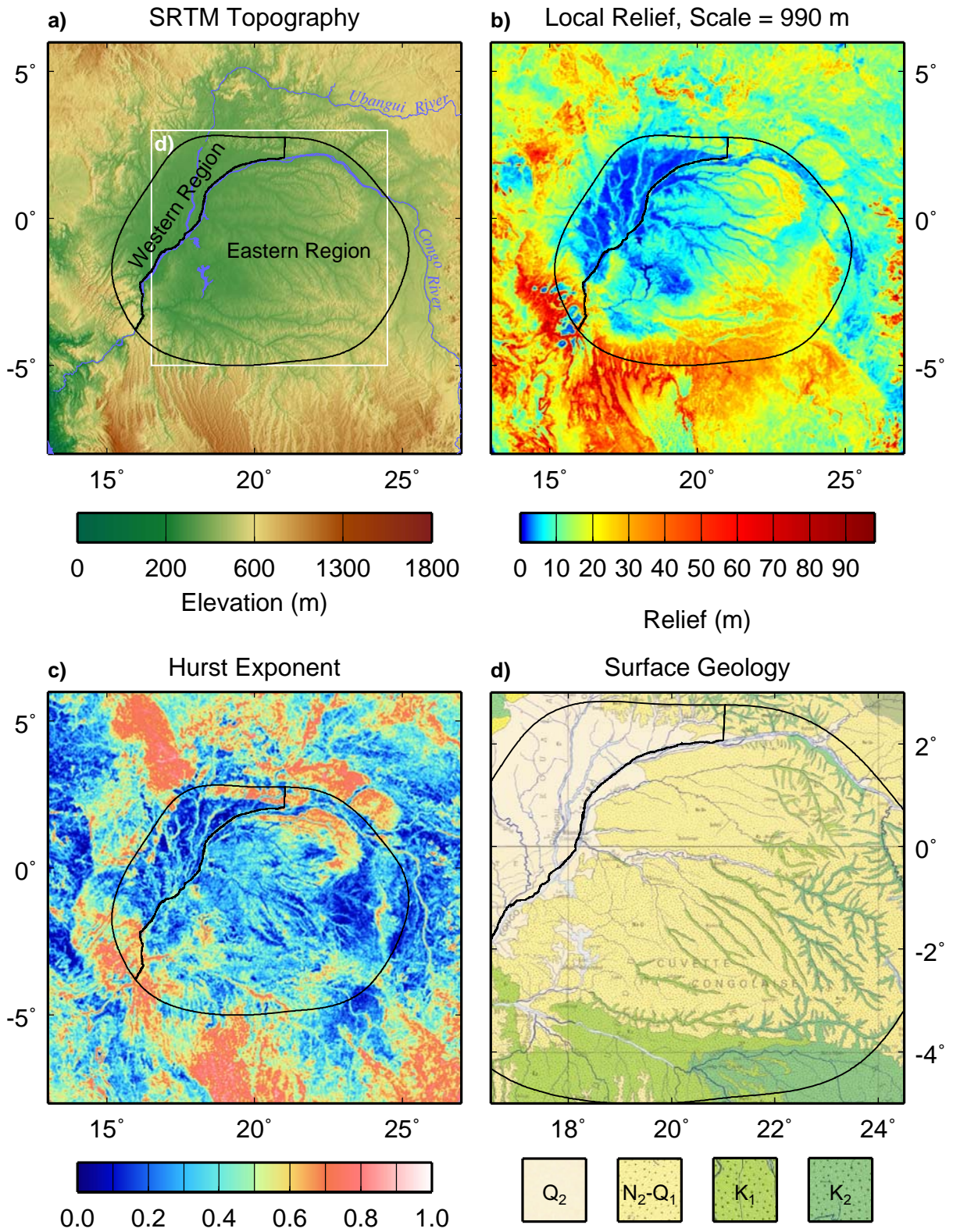
a) SRTM Topography

b) Local Relief, Scale = 990 m

c) Hurst Exponent

d) Surface Geology

Figure 5: **a)** Profiles of the topographic deflections for the models with subsidence rates less than 10 m/Ma along longitude 22°E. **b)** Uplift/subsidence of the models in a) along the same profile. Dashed line indicates heat diffusion was allowed in the model while solid line means that diffusion was not allowed. Uplift is only observed if there is diffusion of heat within the anomaly, however very low subsidence rates can be achieved for no diffusion if the viscosity profile within the lithosphere is nearly linear.
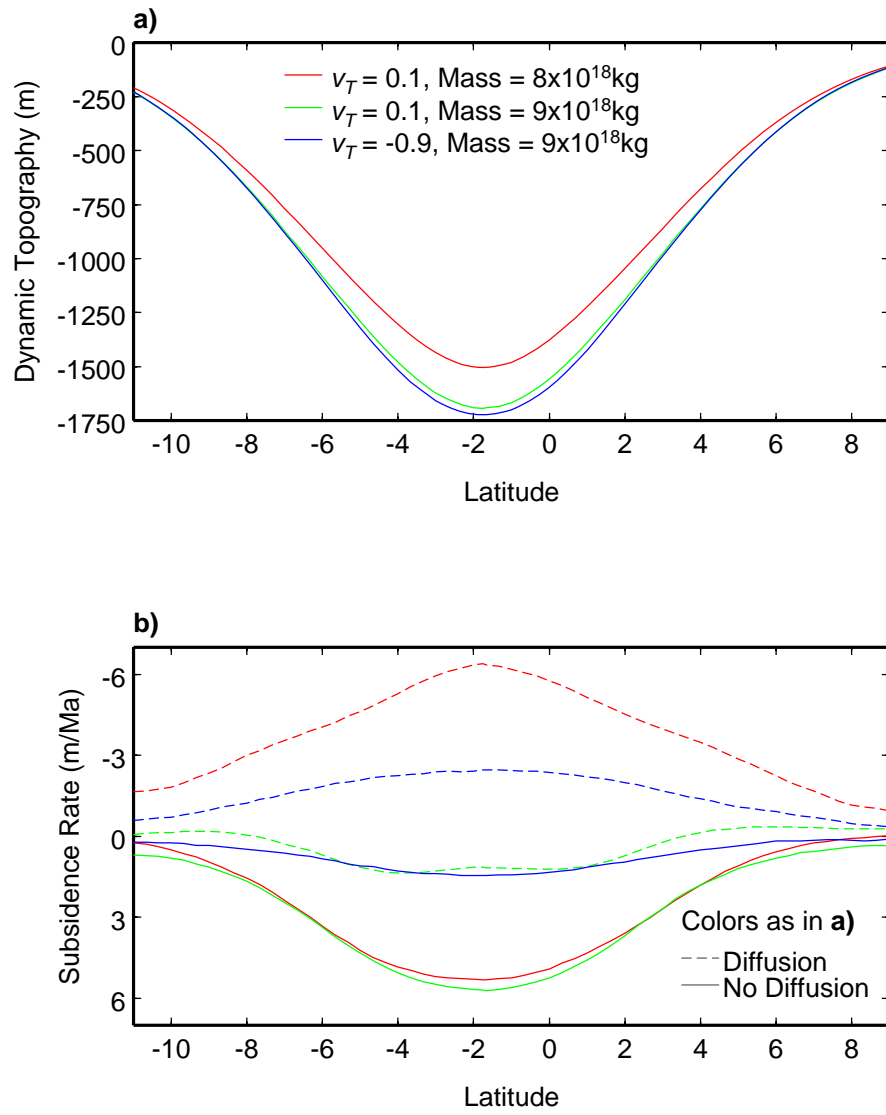
Figure 6: **a)** Synthetic subsidence curve for the exponential decay model, typical of a thermal contraction mechanism for basin subsidence. The data points from the subsidence curve of the Samba well are shown for comparison. **b)** Synthetic geohistory associated with the model in a). In this model sediment deposition within the basin gradually decreases to the current state in which sediments bypass the basin and are deposited on the passive margin. **c)-d)** Same as a)-b) but for the basin rebound model. The shaded sediments in d) represent sediments deposited within the basin which were later eroded and deposited on the coast. This mechanism is consistent with the rapid increase of sediment delivery to the passive margin near 34 Ma and also explains the uplifted topography in the central regions of the Congo basin (Figure 4a).

a) Exponential Subsidence

b) Synthetic Geohistory

c) Basin Rebound

d) Synthetic Geohistory